

Fundamental limits on the rate of bacterial growth

**3 Nathan M. Belliveau^{†, 1}, Griffin Chure^{†, 2}, Christina L. Hueschen³, Hernan G. Garcia⁴, Jane
4 Kondev⁵, Daniel S. Fisher⁶, Julie A. Theriot^{1, 7, *}, Rob Phillips^{8, 9, *}**

5 ¹Department of Biology, University of Washington, Seattle, WA, USA; ²Department of Applied Physics,
6 California Institute of Technology, Pasadena, CA, USA; ³Department of Chemical Engineering,
7 Stanford University, Stanford, CA, USA; ⁴Department of Molecular Cell Biology and Department of
8 Physics, University of California Berkeley, Berkeley, CA, USA; ⁵Department of Physics, Brandeis
9 University, Waltham, MA, USA; ⁶Department of Applied Physics, Stanford University, Stanford, CA,
10 USA; ⁷Allen Institute for Cell Science, Seattle, WA, USA; ⁸Division of Biology and Biological Engineering,
11 California Institute of Technology, Pasadena, CA, USA; ⁹Department of Physics, California Institute of
12 Technology, Pasadena, CA, USA; *Co-corresponding authors. Address correspondence to
13 phillips@pboc.caltech.edu and jtheriot@uw.edu; [†]These authors contributed equally to this work

14

15 **Abstract** Recent years have seen an experimental deluge interrogating the relationship between bacterial
16 growth rate, cell size, and protein content, quantifying the abundance of proteins across growth conditions with
17 unprecedented resolution. However, we still lack a rigorous understanding of what sets the scale of these
18 quantities and when protein abundances should (or should not) depend on growth rate. Here, we seek to
19 quantitatively understand this relationship across a collection of *Escherichia coli* proteomic data covering ≈ 4000
20 proteins and 36 growth rates. We estimate the basic requirements for steady-state growth by considering key
21 processes in nutrient transport, energy generation, cell envelope biogenesis, and the central dogma. From these
22 estimates, ribosome biogenesis emerges as a primary determinant of growth rate. We expand on this
23 assessment by exploring a model of proteomic regulation as a function of the nutrient supply, revealing a
24 mechanism that ties cell size and growth rate to ribosomal content.

25

26 **Introduction**

27 The observed range of bacterial growth rates is enormously diverse. In natural environments, some microbial
28 organisms may double only once per year (?) while in comfortable laboratory conditions, growth can be rapid
29 with several divisions per hour (?). This six order-of-magnitude difference in time scales of growth encompasses
30 different microbial species and lifestyles, yet even for a single species such as *Escherichia coli*, the growth rate can
31 be modulated over a comparably large scale by tuning the type and amount of nutrients in the growth medium (?).
32 This remarkable flexibility in growth rate illustrates the intimate relationship between environmental conditions
33 and the rates at which cells convert nutrients into new cellular material – a relationship that has remained a major
34 topic of inquiry in bacterial physiology for over a century (?).

35 Several of the evergreen questions about bacterial growth and physiology that were originally raised by mi-
36 crobiologists in the middle of the 20th century can now be reframed in light of newly available proteomic data.
37 For example, what biological processes are the primary determinants for how quickly bacterial cells can grow and
38 reproduce? How do cells modulate the absolute numbers and relative ratios of their molecular constituents as a
39 function of changes in growth rate or nutrient availability? In this paper, we begin by considering these two ques-
40 tions from two distinct angles. First, as a result of an array of high-quality proteome-wide measurements of *E. coli*
41 under diverse growth conditions, we have a census that allows us to explore how the number of key molecular

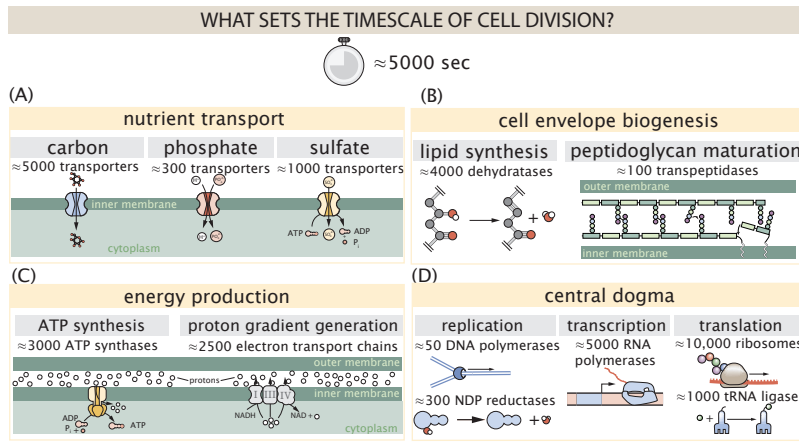


Figure 1. Transport and synthesis processes necessary for cell division. We consider an array of processes necessary for a cell to double its molecular components, broadly grouped into four classes. These categories are (A) nutrient transport across the cell membrane, (B) cell envelope biogenesis, (C) energy production (namely, ATP synthesis), and (D) processes associated with the central dogma. Numbers shown are the approximate number of complexes of each type observed at a growth rate of 0.5 hr^{-1} , or a cell doubling time of $\approx 5000 \text{ s}$.

42 players change as a function of growth rate. Here, we have assembled a singular data set using measurements
 43 collected over the past decade via mass spectrometry (???) or ribosomal profiling (?) of the composition of the *E.*
 44 *coli* proteome across 36 unique growth rates (see the Appendix Section "Experimental Details Behind Proteomic
 45 Data" for a further discussion of the data). Second, by compiling molecular turnover rate measurements for many
 46 of the fundamental processes associated with bacterial growth, we make quantitative estimates of a handful of
 47 key cellular processes (schematized in **Figure 1**) to determine whether our current understanding of the dynamics
 48 of these processes are sufficient to explain the magnitude of the observed protein copy numbers across condi-
 49 tions (see **Box 1** describing the philosophy behind this approach). The census, combined with these estimates,
 50 provide a window into the question of whether the rates of central processes such as energy generation or DNA
 51 synthesis are regulated systematically as a function of cell growth rate by altering protein copy number.

52 Throughout our estimates, we consider an archetypal growth rate of $\approx 0.5 \text{ hr}^{-1}$ corresponding to a doubling
 53 time of ≈ 5000 seconds, as the data sets examined here heavily sample this growth regime. While we formulate
 54 point estimates for the protein abundances at this division time, we also consider how these values will vary at
 55 other growth rates due to changes in cell size, surface area, and chromosome copy number (??). For the majority
 56 of the processes considered, we find that the protein copy numbers appear tuned for the task of cell doubling
 57 across a continuum of growth rates. Thus, our understanding of the kinetics of myriad biological processes is
 58 sufficient to quantitatively explain the observed abundances of these proteins.

59 From these estimates, it emerges that translation, particularly the synthesis of ribosomal proteins, is a plausible
 60 candidate that limits the rate of cell division in *E. coli*. We reach this conclusion by considering that ribosome
 61 synthesis is 1) a rate limiting step for the *fastest* bacterial division, and 2) a major determinant of bacterial growth
 62 across the nutrient conditions we have considered under steady state, exponential growth. This enables us to
 63 suggest that the long-observed correlation between growth rate and cell size (??) can be simply attributed to
 64 the increased absolute number of ribosomes per cell under conditions supporting extremely rapid growth. To
 65 better understand how the observed alterations in absolute protein abundances, and in particular, changes in
 66 ribosome copy number, influence growth rate across different nutrient conditions we consider a minimal model
 67 of cellular growth. Our conclusions from these analyses provide important insight into how *E. coli* regulates growth
 68 across conditions of differing nutrient availability and identifies fundamental constraints in bacterial growth more
 69 broadly.

109 Nutrient Transport

110 We begin by considering the critical transport processes diagrammed in **Figure 1(A)**. In order to build new cellular
 111 mass, the molecular and elemental building blocks must be scavenged from the environment in different forms.

70 Box 1. The Rules of Engagement for Order-Of-Magnitude Estimates

72 This work relies heavily on "back-of-the-envelope" estimates to understand the growth-rate dependent abundances of molecular complexes. This moniker arises from the limitation that any estimate should be able to fit on the back of a postage envelope. As such, we must draw a set of rules governing our precision and sources of key values.

74 **The rule of "one, few, and ten".** The philosophy behind order-of-magnitude estimates is to provide an estimate of the appropriate scale, not a prediction with many significant digits (?). We therefore define three different scales of precision in making estimates. The scale of "one" is reserved for values that range between 1 and 2. For example, If a particular process has been experimentally measured to transport 1.87 protons for a process to occur, we approximate this process to require 2 protons per event. The scale of "few" is reserved for values ranging between 3 and 7. For example, we will often use Avogadro's number to compute the number of molecules in a cell given a concentration and a volume. Rather than using Avogadro's number as 6.02214×10^{23} , we will approximate it as 5×10^{23} . Finally, the scale of "ten" is reserved for values which we know within an order of magnitude. If a particular protein complex is present at 883 copies per cell, we say that it is present in approximately 10^3 copies per cell. These different scales will be used to arrive at simple estimates that report the expected scale of the observed data. Therefore, the estimates presented here should not be viewed as hard-and-fast predictions of precise copy numbers, but as approximate lower (or upper) bounds for the number of complexes that may be needed to satisfy some cellular requirement.

86 Furthermore, we use equality symbols (=) sparingly and frequently defer to approximation (\approx) or scaling (\sim) symbols when reporting an estimate. When \approx is used, we are implicitly stating that we are confident in this estimate within a factor of a few. When a scaling symbol \sim is used, we are stating that we are confident in our estimate to within an order of magnitude.

93 **The BioNumbers Database as a source for values.** In making our estimates, we often require approximate values for key cellular properties, such as the elemental composition of the cell, the average dry mass, or approximate rates of synthesis. We rely heavily on the BioNumbers Database (bionumbers.hms.harvard.edu, ?) as a repository for such information. Every value we draw from this database has an associated BioNumbers ID number, abbreviated as BNID, and we provide this reference in grey-boxes in each figure.

99 **Uncertainty in the data sets and the accuracy of an estimate.** The data sets presented in this work are the products of careful experimentation with the aim to report, to the best of their ability, the absolute copy numbers of proteins in the cell. These data, collected over the span of a few years, come from different labs and use different internal standards, controls, and even techniques (discussed further in Appendix Experimental Details Behind Proteomic Data). As a result, there is notable disagreement in the measured copy numbers for some complexes across data sets. In assessing whether our estimates could explain the observed scales and growth-rate dependencies, we also considered the degree of variation between the different data sets. 104 For example, say a particular estimate undercuts the observed data by an order of magnitude. If all data sets agree within a factor of a few of each other, we revisit our estimate and consider what we may have missed. 106 However, if the data sets themselves disagree by an order of magnitude, we determine that our estimate is appropriate given the variation in the data.

112 Carbon, for example, is acquired via the transport of carbohydrates and sugar alcohols with some carbon sources
113 receiving preferential treatment in their consumption (?). Phosphorus, sulfur, and nitrogen, on the other hand,
114 are harvested primarily in the forms of inorganic salts, namely phosphate, sulfate, and ammonium/ammonia
115 (??????). All of these compounds have different membrane permeabilities (?) and most require some energetic
116 investment either via ATP hydrolysis or through the proton electrochemical gradient to bring the material across
117 the hydrophobic cell membrane.

118 The elemental composition of *E. coli* has received much quantitative attention over the past half century (????),
119 providing us with a starting point for estimating how many atoms of each element must be scavenged from the
120 environment. A synthesis of these studies presents an approximate dry mass composition of \approx 50% carbon (BNID:
121 100649; see **Box 1** for explanation of BNID references), \approx 15% nitrogen (BNID: 106666), \approx 3% phosphorus (BNID:
122 100653), and 1% sulfur (BNID: 100655) with the remainder being attributable to oxygen, hydrogen, and various
123 transition metals. We use this stoichiometric breakdown to estimate the abundance and growth rate dependence
124 of a variety of transporters responsible for carbon uptake, and provide more extensive investigation of the other
125 critical elements – phosphorus, sulfur, and nitrogen – in the Appendix Section "Additional Estimates of Fundamen-
126 tal Biological Processes".

127 Using \approx 0.3 pg as the typical *E. coli* dry mass at a growth rate of \approx 0.5 hr $^{-1}$ (BNID: 103904), coupled with an
128 approximation that \approx 50% of this mass is carbon, we estimate that $\sim 10^{10}$ carbon atoms must be brought into
129 the cell in order to double all of the carbon-containing molecules (**Figure 2(A)**, top). Typical laboratory growth
130 conditions provide carbon as a single class of sugar (such as glucose, galactose, or xylose) often transported cross
131 the cell membrane by a transporter complex specific to that particular sugar. One such mechanism of transport is
132 via the PTS system, which is a highly modular system capable of transporting a diverse range of sugars with high
133 specificity (?). The glucose-specific component of this system transports \approx 200 glucose molecules (\approx 1200 carbon
134 atoms) per second per transporter (BNID: 114686). Making the assumption that this is a typical sugar transport
135 rate for the PTS system, coupled with the need to transport $\sim 10^{10}$ carbon atoms, we then expect on the order of
136 \approx 2000 transporters must be expressed per cell in order to bring in enough carbon atoms (**Figure 2(A)**, top).

137 We find, however, that the experimental measurements exceed this by several fold (**Figure 2(A)**, bottom), im-
138 plying that the cell is capable of transporting more carbon atoms than strictly needed for biosynthesis. We can
139 also abstract this calculation to consider any particular growth rate given knowledge of the cell density and vol-
140 ume as a function of growth rate and direct the reader to the Appendix Section "Extending Estimates to a Con-
141 tinuum of Growth Rates" for more information. This abstraction, shown as a grey line in **Figure 2(A)**, reveals an
142 excess of transporters even at faster growth rates. This contrasts with our observations for uptake of phosphorus
143 and sulfur, which turn out to align well with our expectations across different growth conditions (**Figure 2-Figure**
144 **Supplement 1** and discussed further in the Appendix Section "Additional Estimates of Fundamental Biological
145 Processes").

146 It is important to note that so far we have neglected any specifics of the regulation of the carbon transport
147 system. Using the diverse array of growth conditions available in the data, we can explore how individual carbon
148 transport systems depend on specific carbon availability. In **Figure 2(B)**, we show the total number of carbohydrate
149 transporters specific to different carbon sources. A striking observation, shown in the top-left plot of **Figure 2(B)**, is
150 the constancy in the expression of the glucose-specific transport systems, an observation that stands in contrast
151 with other species of transporters. Additionally, we note that the total number of glucose-specific transporters is
152 tightly distributed at $\approx 10^4$ per cell, the approximate number of transporters needed to sustain rapid growth of
153 several divisions per hour. This illustrates that *E. coli* maintains a substantial number of complexes present for
154 transporting glucose regardless of growth condition, which is known to be the preferential carbon source (??).

155 Many metabolic operons are regulated with dual-input logic gates that are only expressed when glucose con-
156 centrations are low and the concentration of other carbon sources are elevated (?????). Points colored in red in
157 **Figure 2(B)** (labeled by red text-boxes) correspond to growth conditions in which the specific carbon source (glyc-
158 erol, xylose, or fructose) is present as the sole source of carbon. The grey lines in **Figure 2(B)** show the estimated
159 number of transporters needed at each growth rate to satisfy the cellular carbon requirement, adjusted for the
160 specific carbon source in terms of number of carbon atoms per molecule and the rate of transport for the partic-
161 ular transporter species. These plots show that, even in the absence of the particular carbon source, expression
162 of the transporters is maintained on the order of $\sim 10^2$ per cell. The low but non-zero abundances may reflect the

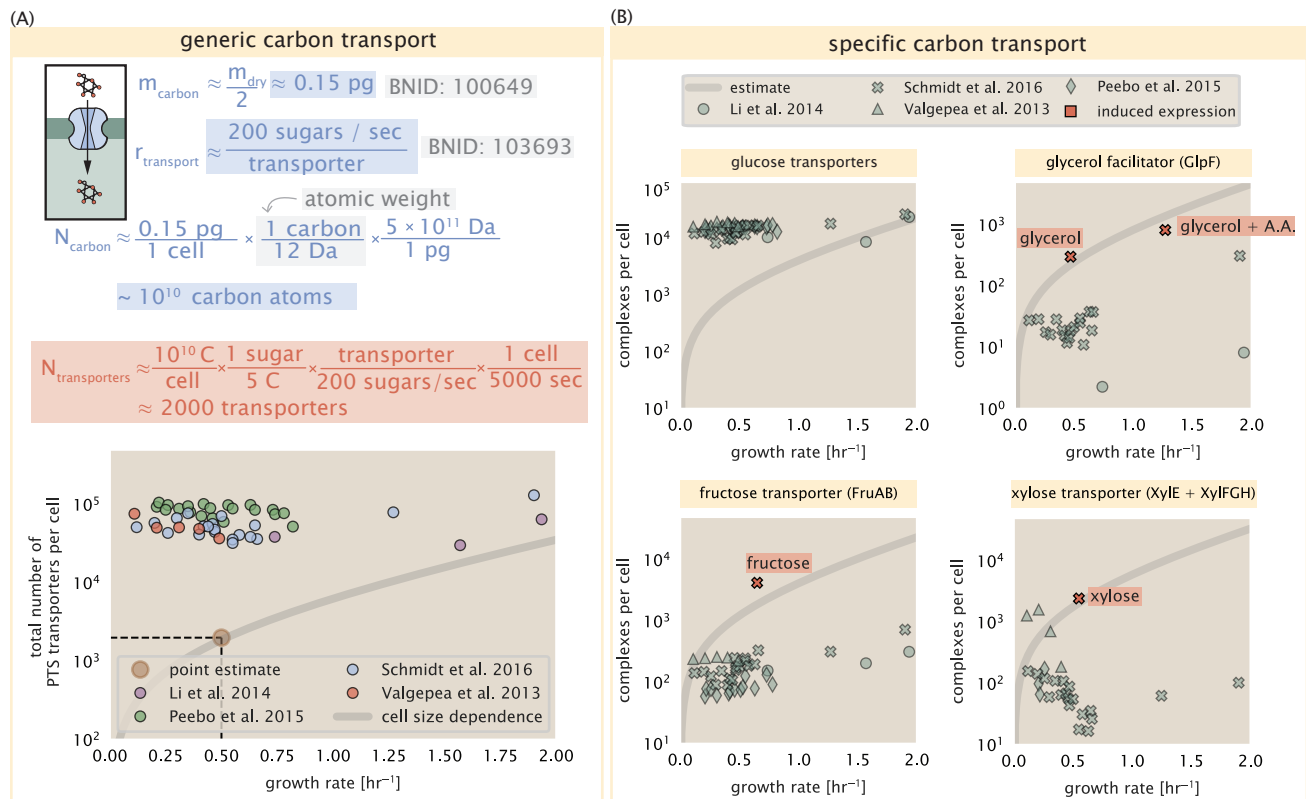


Figure 2. The abundance of carbon transport systems across growth rates. (A) A simple estimate for the minimum number of generic carbohydrate transport systems (top) assumes $\sim 10^{10}$ C are needed to complete division, each transported sugar contains ≈ 5 C, and each transporter conducts sugar molecules at a rate of ≈ 200 per second. Bottom plot shows the estimated number of transporters needed at a growth rate of ≈ 0.5 per hr (light-brown point and dashed lines). Colored points correspond to the mean number of complexes involved in carbohydrate import (complexes annotated with the Gene Ontology terms GO:0009401 and GO:0098704) for different growth conditions across different published datasets. (B) The abundance of various specific carbon transport systems plotted as a function of the population growth rate. The rates of substrate transport differ between these transporter species. To compute the continuum growth rate estimate (grey line), we used the following transport rates for each transporter species: 200 glucose- s^{-1} (BNID: 103693), 2000 glycerol- s^{-1} (?), 200 fructose- s^{-1} (assumed to be similar to PtsI, BNID: 103693), and 50 xylose- s^{-1} (assumed to be comparable to LacY, BNID: 103159). Red points and highlighted text indicate conditions in which the only source of carbon in the growth medium induces expression of the transport system. Grey lines in (A) and (B) represents the estimated number of transporters per cell at a continuum of growth rates.

Figure 2-Figure supplement 1. Estimates and observed abundances of phosphate and sulfate transporters.

163 specific regulatory logic involved, requiring that cells are able to transport some minimal amount of an alternative
164 carbon source in order to induce expression of these alternative carbon-source systems when needed.

165 **Limits on Transporter Expression**

166 If acquisition of nutrients was a limiting process in cell division under the typical growth conditions explored here,
167 the growth rate could be theoretically increased simply by expressing more transporters, but is this feasible at a
168 physiological level? A way to approach this question is to compute the amount of space in the bacterial membrane
169 that could be occupied by nutrient transporters. Considering a rule-of-thumb for the surface area of *E. coli* of
170 about $5 \mu\text{m}^2$ (BNID: 101792), we expect an areal density for 2000 transporters to be approximately a few hundred
171 transporters per μm^2 . For a typical transporter occupying about 50 nm^2 , this amounts to about only $\approx 1\%$ of
172 the total inner membrane surface area (?). Bacterial cell membranes typically have densities of 10^5 proteins/ μm^2
173 (?), with roughly 60 % of the surface area occupied by protein (BNID: 100078), implying that the cell could easily
174 accommodate more transporters. There are, however, additional constraints on the space that can be devoted to
175 nutrient uptake due to occupancy by proteins involved in processes like cell wall synthesis and energy production,
176 and we will consider this further in the coming sections.

177 **Cell Envelope Biogenesis**

178 In contrast to nutrient transporters, which support the synthesis of biomolecules throughout the cell and therefore
179 need to scale with the cell size, here we must consider the synthesis of components that will need to scale with
180 the surface area of the cell. *E. coli* is a rod-shaped bacterium with a remarkably robust length-to-width aspect ratio
181 of $\approx 4:1$ (?). Assuming this surface area is approximately the same between the inner and outer membranes of
182 *E. coli*, and the fact that each membrane is itself a lipid bilayer, our rule-of-thumb of $5 \mu\text{m}^2$ per surface suggests a
183 total membrane surface area of $\approx 20 \mu\text{m}^2$ (see the Appendix Section "Estimation of Cell Size and Surface Area" for
184 a description of the calculation of cell surface area as a function of cell size). In this section, we will estimate the
185 number of key protein complexes needed to synthesize the lipids as well as the complexes involved in assembling
186 the peptidoglycan scaffold that make up the cell envelope.

187 **Lipid Synthesis**

188 The dense packing of the membrane with proteins means that the cell membranes are not composed entirely of
189 lipid molecules, with only $\approx 40\%$ of the membrane area occupied by lipids (BNID: 100078). Using a rule-of-thumb
190 of 0.5 nm^2 as the surface area of the typical lipid (BNID: 106993), we can estimate $\sim 2 \times 10^7$ lipids per cell, which
191 is in close agreement with experimental measurements (BNID: 100071, 102996).

192 The membranes of *E. coli* are composed of a variety of different lipids, each of which are unique in their structures and biosynthetic pathways (?). Recently, a combination of stochastic kinetic modeling (?) and *in vitro* kinetic measurements (??) has revealed remarkably slow steps in the fatty acid synthesis pathways which may serve as the rate limiting reactions for making new membrane phospholipids in *E. coli*. One such step is the removal of hydroxyl groups from the fatty-acid chain by ACP dehydratase that leads to the formation of carbon-carbon double bonds. This reaction, catalyzed by proteins FabZ and FabA (?), have been estimated to have kinetic turnover rates of ≈ 1 dehydration per second per enzyme (?). Thus, given this rate and the need to synthesize $\approx 2 \times 10^7$ lipids over 5000 seconds, one can estimate that a typical cell requires ≈ 4000 ACP dehydratases. This is in reasonable agreement with the experimentally observed copy numbers of FabZ and FabA (*Figure 3(A)*). Furthermore, we can extend this estimate to account for the change in membrane surface area as a function of the growth rate (grey line in *Figure 3(A)*), which captures the observed growth rate dependent expression of these two enzymes.

203 **Peptidoglycan Synthesis**

204 The exquisite control of bacteria over their cell shape is due primarily to a stiff, several nanometer thick meshwork
205 of polymerized disaccharides that makes up the cell wall termed the peptidoglycan. The formation of the peptidoglycan
206 is an intricate process involving many macromolecular players (?), whose coordinated action maintains
207 cell shape and integrity even in the face of large-scale perturbations (?). The peptidoglycan alone comprises \approx
208 3% of the cellular dry mass (BNID: 1019360), making it the most massive molecule in *E. coli*. The polymerized
209 unit of the peptidoglycan is a N-acetylglucosamine and N-acetylmuramic acid disaccharide, of which the former

210 is functionalized with a short pentapeptide. With a mass of \approx 1000 Da, this unit, which we refer to as a murein
211 monomer, is polymerized to form long strands in the periplasm which are then attached to each other via their
212 peptide linkers. Together, these quantities provide an estimate of $\approx 5 \times 10^6$ murein monomers per cell.

213 The crosslinking of the pentapeptides between adjacent glycan strands is responsible for maintaining the struc-
214 tural integrity of the cell wall and, in principle, each murein monomer can be involved in such a crosslink. In some
215 microbes, such as in gram-positive bacterium *Staphylococcus aureus*, the extent of crosslinking can be large with
216 > 90% of pentapeptides forming a connection between glycan strands. In *E. coli*, however, a much smaller propor-
217 tion (\approx 20%) of the peptides are crosslinked, resulting in a weaker and more porous cell wall (??). The formation of
218 these crosslinks occurs primarily during the polymerization of the murein monomers and is facilitated by a family
219 of enzymes called transpeptidases. The four primary transpeptidases of *E. coli* have only recently been quantita-
220 tively characterized *in vivo*, via liquid chromatography mass spectrometry, which revealed a notably slow kinetic
221 turnover rate of \approx 2 crosslinking reactions formed per second per enzyme (?).

222 Assembling these quantities permits us to make an estimate that on the order of \approx 100 transpeptidases per cell
223 are needed for complete maturation of the peptidoglycan, given a division time of \approx 5000 seconds; a value that
224 is comparable to experimental observations [Figure 3(B)]. Expanding this estimate to account for the changing
225 mass of the peptidoglycan as a function of growth rate [grey line in Figure 3(B)] also qualitatively captures the
226 observed dependence in the data, though systematic disagreements between the different data sets makes the
227 comparison more difficult.

228 Limits on Cell Wall Biogenesis

229 While the processes we have considered represent only a small portion of proteins devoted to cell envelope bio-
230 genesis, we find it unlikely that they limit cellular growth in general. The relative amount of mass required for lipid
231 and peptidoglycan components decrease at faster growth rates due to a decrease in their surface area to volume
232 (S/V) ratio (?). Furthermore, despite the slow catalytic rate of FabZ and FabA in lipid synthesis, experimental data
233 and recent computational modeling has shown that the rate of fatty-acid synthesis can be drastically increased
234 by increasing the concentration of FabZ (??). With a proteome size of $\approx 3 \times 10^6$ proteins, a hypothetical 10-fold in-
235 crease in expression from 4000 to 40,000 ACP dehydratases would result in a paltry \approx 1% increase in the size of the
236 proteome. In the context of peptidoglycan synthesis, we note that our estimate considers only the transpeptidase
237 enzymes that are involved in lateral and longitudinal elongation of the peptidoglycan. This neglects the presence
238 of other transpeptidases that are present in the periplasm and also involved in remodeling and maturation of the
239 peptidoglycan. It is therefore possible that if this was setting the speed limit for cell division, the simple expression
240 of more transpeptidases may be sufficient to maintain the structural integrity of the cell wall.

241 Energy Production

242 Cells consume and generate energy predominantly in the form of nucleoside triphosphates (NTPs) in order to
243 grow. The high-energy phosphodiester bonds of (primarily) ATP power a variety of cellular processes that drive
244 biological systems away from thermodynamic equilibrium. We now turn to the synthesis of ATP as a potential
245 process that may limit growth, which also requires us to consider the maintenance of the electrochemical proton
246 gradient which powers it.

247 ATP Synthesis

248 Hydrolysis of the terminal phosphodiester bond of ATP into ADP (or alternatively GTP and GDP) and an inorganic
249 phosphate provides the thermodynamic driving force in a wide array of biochemical reactions. One such reaction
250 is the formation of peptide bonds during translation, which requires \approx 2 ATPs for the charging of an amino acid
251 to the tRNA and \approx 2 GTPs for the formation of each peptide bond. Assuming the ATP costs associated with error
252 correction and post-translational modifications of proteins are negligible, we can make the approximation that
253 each peptide bond has a net cost of \approx 4 ATP (BNID: 101442). Formation of GTP from ATP is achieved via the action
254 of nucleoside diphosphate kinase, which catalyzes this reaction without an energy investment (?) and therefore
255 consider all NTP requirements of the cell to be functionally equivalent to being exclusively ATP. In total, the en-
256 ergetic costs of peptide bond formation consume \approx 80% of the cells ATP budget [BNID: 107782; 106158; 101637;

CELL ENVELOPE BIOSYNTHESIS

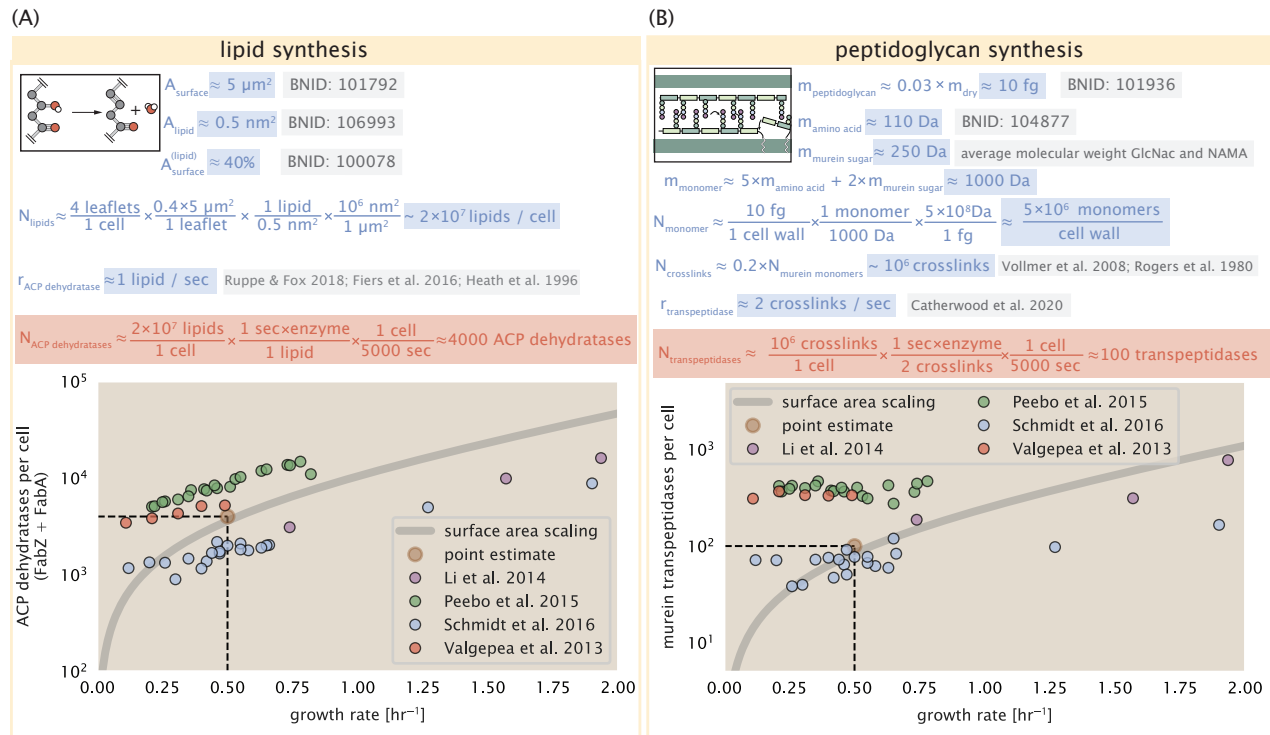


Figure 3. (A) Top panel shows an estimation for the number of ACP dehydratases necessary to form functional phospholipids, which is assumed to be a rate-limiting step on lipid synthesis. The rate of ACP dehydratases was inferred from experimental measurements via a stochastic kinetic model described in ?. Bottom panel shows the experimentally observed complex copy numbers using the stoichiometries $[\text{FabA}]_2$ and $[\text{FabZ}]_2$. (B) An estimate for the number of peptidoglycan transpeptidases needed to complete maturation of the peptidoglycan. The mass of the murein monomer was estimated by approximating each amino acid in the pentapeptide chain as having a mass of 110 Da and each sugar in the disaccharide having a mass of ≈ 250 Da. The *in vivo* rate of transpeptidation in *E. coli* was taken from recent analysis by ?. The bottom panel shows experimental measurements of the transpeptidase complexes in *E. coli* following the stoichiometries $[\text{MrcA}]_2$, $[\text{MrcB}]_2$, $[\text{MrdA}]_1$, and $[\text{MrdB}]_1$. Grey curves in each plot show the estimated number of complexes needed to satisfy the synthesis requirements scaled by the surface area as a function of growth rate.

257 111918, ??]. The pool of ATP is produced by the F₁-F₀ ATP synthase – a membrane-bound rotary motor which
258 under ideal conditions can yield ≈ 300 ATP per second [BNID: 114701; ?].
259 To estimate the total number of ATP equivalents consumed during a cell cycle, we will make the approximation
260 that there are $\approx 3 \times 10^6$ proteins per cell with an average protein length of ≈ 300 peptide bonds (BNID: 115702;
261 108986; 104877). Taking these values together, coupled with an estimate of ≈ 4 ATP equivalents per peptide bond,
262 we find that the typical *E. coli* cell consumes $\sim 5 \times 10^9$ ATP per cell cycle on protein synthesis alone. Assuming that
263 each ATP synthases operates at its maximal speed (300 ATP per second per synthase), ≈ 3000 ATP synthases
264 are needed to keep up with the energy demands of the cell. This estimate is comparable with the experimental
265 observations, shown in *Figure 4* (A). We note that this estimate assumes all ATP is synthesized via ATP synthase
266 and neglects synthesis via fermentative metabolism. This simplification may explain why at the fastest growth
267 rates (≈ 2 hr⁻¹), our continuum estimate predicts more synthase than is experimentally observed (gray line in
268 *Figure 4*). At rapid growth rates, *E. coli* enters a type of overflow metabolism where non-respiratory routes for ATP
269 synthesis become pronounced (???).

270 Generating the Proton Electrochemical Gradient

271 In order to produce ATP, the F₁-F₀ ATP synthase itself must consume energy. Rather than burning through its own
272 product (and violating thermodynamics), this intricate macromolecular machine has evolved to exploit the elec-
273 trochemical potential established across the inner membrane through cellular respiration. This electrochemical
274 gradient is manifest by the pumping of protons into the intermembrane space via the electron transport chains
275 as they reduce NADH. In *E. coli*, this potential difference is ≈ -200 mV (BNID: 102120). A simple estimate of the
276 inner membrane as a capacitor with a working voltage of -200 mV reveals that $\approx 2 \times 10^4$ protons must be present
277 in the intermembrane space. However, each rotation of an ATP synthase shuttles ≈ 4 protons into the cytosol
278 (BNID: 103390). With a few thousand ATP synthases producing ATP at their maximal rate, the potential difference
279 would be rapidly abolished in a few milliseconds if it were not being actively maintained.

280 The electrochemistry of the electron transport complexes of *E. coli* have been the subject of intense biochemical
281 and biophysical study (????). A recent work (?) examined the respiratory capacity of the *E. coli* electron transport
282 complexes using structural and biochemical data, revealing that each electron transport chain rapidly pumps
283 protons into the intermembrane space at a rate of ≈ 1500 protons per second (BNID: 114704; 114687). Using our
284 estimate of the number of ATP synthases required per cell [*Figure 4*(A)], coupled with these recent measurements,
285 we estimate that ≈ 3000 electron transport complexes would be necessary to facilitate the $\sim 5 \times 10^6$ protons per
286 second diet of the cellular ATP synthases. This estimate is in agreement with the number of complexes identified
287 in the proteomic datasets [plot in *Figure 4*(B)]. This suggests that every ATP synthase must be accompanied by \approx
288 1 functional electron transport chain.

289 Limits on Biosynthesis in a Crowded Membrane

290 Our estimates thus far have focused on biochemistry at the periphery of the cell. Since surface area and volume
291 do not scale identically as cell size changes, in order to better understand the physical constraints on transport
292 and energy production it is necessary to consider the consequence of a changing S/V ratio, which will decrease at
293 faster growth rates. Here we use our analysis of ATP production to consider this constraint.

294 In our estimate of ATP production above we found that a cell demands about 5×10^9 ATP per cell cycle or
295 10^6 ATP/s. With a cell volume of roughly 1 fL (BNID: 100004), this corresponds to about 2×10^{10} ATP per fL of
296 cell volume, in line with previous estimates (??). In *Figure 5* (A) we plot this ATP demand as a function of the S/V
297 ratio in green, where we have considered a range of cell shapes from spherical to rod-shaped with an aspect ratio
298 (length/width) equal to 4. In order to consider the maximum ATP that could be produced, we consider the amount
299 of ATP that can be generated by a membrane filled with ATP synthase and electron transport complexes and a
300 maximal production rate of about 3 ATP / (nm²·s) (?). This is shown in blue in *Figure 5*(A), which shows that at least
301 for the growth rates observed (right column in plot), the energy demand is roughly an order of magnitude less.
302 Interestingly, ? found that ATP production by respiration is less efficient than by fermentation on a per membrane
303 area basis, due to the additional proteins of the electron transport chain. This suggests that, even under anaerobic
304 growth, cells will have sufficient membrane space for ATP production.

305 The analysis highlights that there will indeed be a maximum attainable cell size due to a diminishing capacity

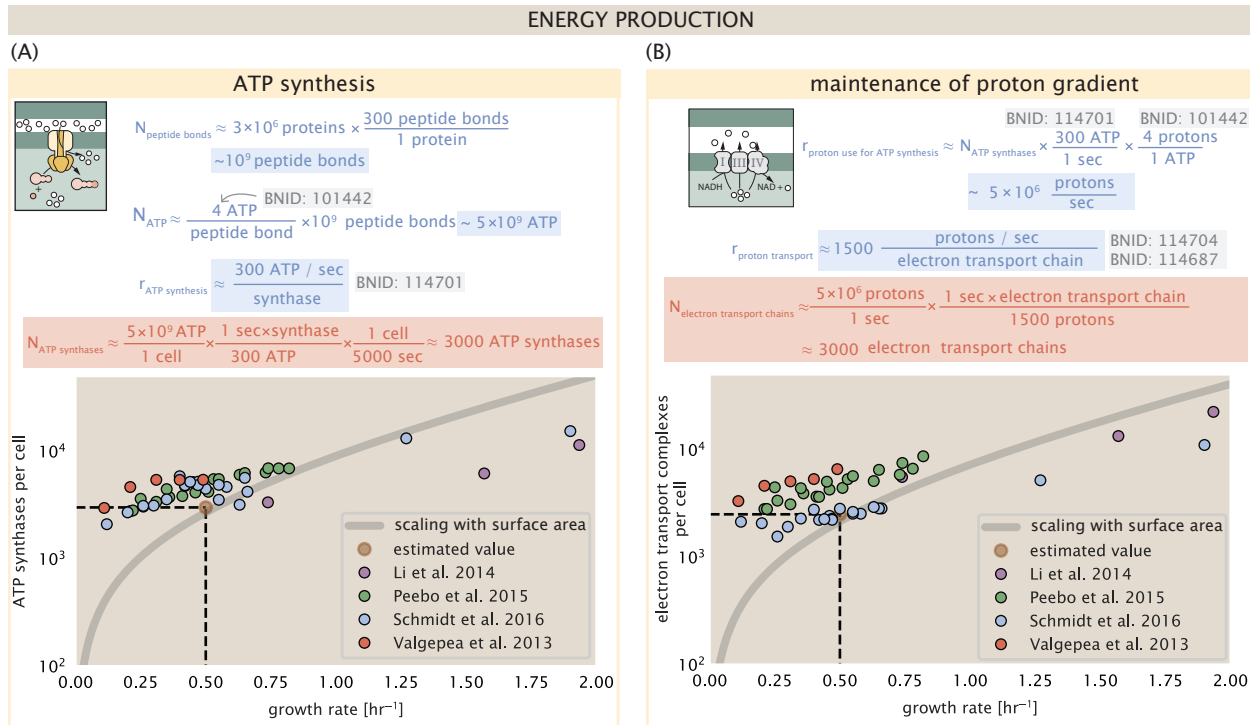


Figure 4. The abundance of F_1 - F_0 ATP synthases and electron transport chain complexes as a function of growth rate.

(A) Estimate of the number of F_1 - F_0 ATP synthase complexes needed to accommodate peptide bond formation and other NTP dependent processes. Points in plot correspond to the mean number of complete F_1 - F_0 ATP synthase complexes that can be formed given proteomic measurements and the subunit stoichiometry $[AtpE]_{10}[AtpF]_2[AtpB][AtpC][AtpH][AtpA]_3[AtpG][AtpD]_3$. (B) Estimate of the number of electron transport chain complexes needed to maintain a membrane potential of -200 mV given estimate of number of F_1 - F_0 ATP synthases from (A). Points in plot correspond to the average number of complexes identified as being involved in aerobic respiration by the Gene Ontology identifier GO:0019646 that could be formed given proteomic observations. These complexes include cytochromes $bd1$ ($[CydA][CydB][CydX][CydH]$), $bdII$ ($[AppC][AppB]$), bo_3 , ($[CyoD][CyoA][CyoB][CyoC]$) and NADH:quinone oxioreductase I ($[NuoA][NuoH][NuoJ][NuoK][NuoL][NuoM][NuoN][NuoB][NuoC][NuoE][NuoF][NuoG][NuoI]$) and II ($[Ndh]$). Grey lines in both (A) and (B) correspond to the estimate procedure described, but applied to a continuum of growth rates. We direct the reader to the Supporting Information for a more thorough description of this approach.

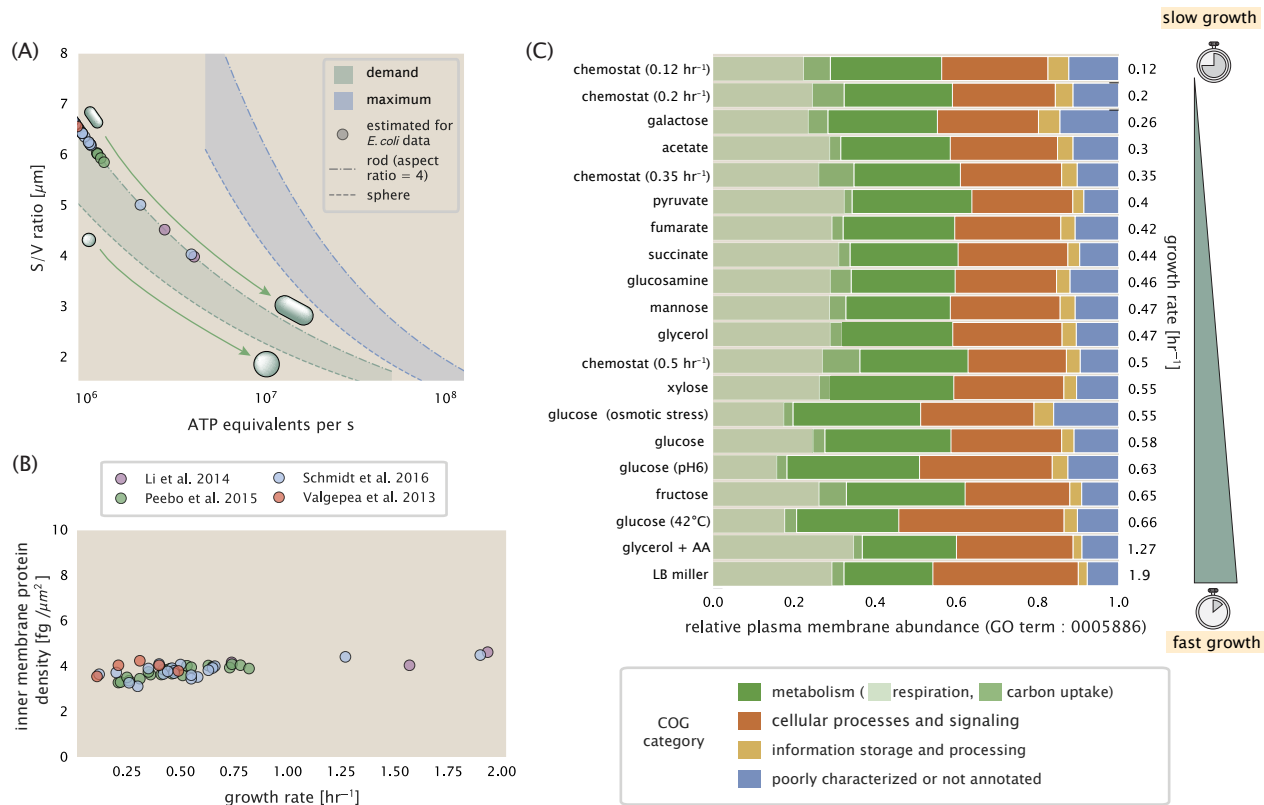


Figure 5. Influence of cell size and surface area to volume (S/V) ratio on ATP production and inner membrane composition. (A) Scaling of ATP demand and maximum ATP production through respiration as a function of S/V ratio. Cell volumes of 0.5 fL to 50 fL were considered, with the dashed (—) line corresponding to a sphere and the dash-dot line (---) reflecting a rod-shaped bacterium like *E. coli* with a typical aspect ratio (length / width) of 4 (?). The ATP demand is calculated as 10⁶ ATP/(μm³ s), while the maximum ATP production rate is taken to be 3 ATP / (nm²·s) (?), with calculations of *E. coli* volume and surface area detailed in Appendix Estimation of Cell Size and Surface Area. In this calculation, 50% of the bacterial inner membrane is assumed to be protein, with the remainder lipid. (B) Total protein mass per μm² calculated for proteins with inner membrane annotation (GO term: 0005886). (C) Relative protein abundances by mass based on COG annotation. Metabolic proteins are further separated into respiration ($F_1\text{-}F_0$ ATP synthase, NADH dehydrogenase I, succinate:quinone oxidoreductase, cytochrome bo₃ ubiquinol oxidase, cytochrome bd-I ubiquinol oxidase) and carbohydrate transport (GO term: GO:0008643). Note that the elongation factor EF-Tu can also associate with the inner membrane, but was excluded in this analysis due to its high relative abundance (roughly identical to the summed protein shown in part (B)).

306 to provide resources as the cell increases in size. The maximum energy production in **Figure 5(A)**, however, does
 307 represent a somewhat unachievable limit since the inner membrane must also include other proteins such as
 308 those we've considered for nutrient transport and cell wall biogenesis. To better understand the overall proteomic
 309 makeup of the inner membrane, we therefore used Gene Ontology (GO) annotations (?) to identify all proteins
 310 embedded or peripheral to the inner membrane (GO term: 0005886). Those associated but not membrane-bound
 311 include proteins like MreB and FtsZ and must nonetheless be considered as a vital component occupying space on
 312 the membrane. In **Figure 5(B)**, we find that the total protein mass per μm² is nearly constant across growth rates.
 313 Interestingly, when we consider the distribution of proteins grouped by their Clusters of Orthologous Groups
 314 (COG) (?), the relative abundance of each category is relatively constant across growth rates. This suggests that
 315 no one process (energy production, nutrient uptake, etc.) is dominating even at fast growth rates [**Figure 5(C)**].

316 Processes of the Central Dogma

317 Up to this point, we have considered a variety of transport and biosynthetic processes that are critical to acquiring
 318 and generating new cell mass. While there are of course many other metabolic processes we could consider, we
 319 now turn our focus to some of the most important processes which *must* be undertaken irrespective of the growth

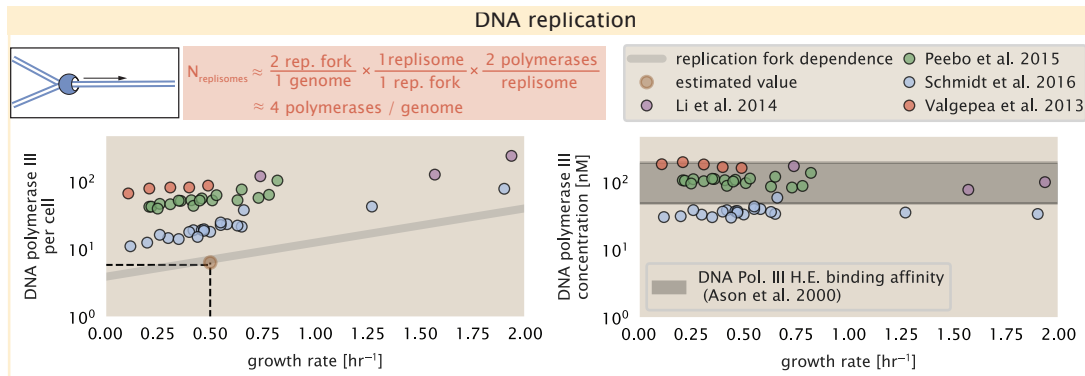


Figure 6. Complex abundance estimates for dNTP synthesis and DNA replication. An estimate for the minimum number of DNA polymerase holoenzyme complexes needed to facilitate replication of a single genome. Points in the left-hand plot correspond to the total number of DNA polymerase III holoenzyme complexes ($[\text{DnaE}]_3[\text{DnaQ}]_3[\text{HolE}]_3[\text{DnaX}]_5[\text{HolB}][\text{HolA}][\text{DnaN}]_4[\text{HolC}]_4[\text{Hold}]_4$) per cell. Right-hand plot shows the effective concentration of DNA polymerase III holoenzyme (See Appendix Estimation of Cell Size and Surface Area for calculation of cell size). Grey lines in left-hand panel show the estimated number of complexes needed as a function of growth, the details of which are described in the Supplemental Information.

Figure 6-Figure supplement 1. Estimate and observations of the abundance of ribonucleotide reductase, a key component in dNTP synthesis.

320 conditions – those of the central dogma.

321 DNA Replication

322 Most bacteria (including *E. coli*) harbor a single, circular chromosome and can have extra-chromosomal plasmids
323 up to ~ 100 kbp in length. While we consider the starting material dNTPs in **Figure 6-Figure Supplement 1** and dis-
324 cussed further in the Appendix Section "Additional Process of the Central Dogma", here we focus our quantitative
325 thinking on the chromosome of *E. coli*, which harbors ≈ 5000 genes and $\approx 5 \times 10^6$ base pairs.

326 To successfully divide and produce viable progeny, this chromosome must be faithfully replicated and segre-
327 gated into each nascent cell. Replication is initiated at a single region of the chromosome termed the *oriC* locus
328 where a pair of replisomes, each consisting of two DNA polymerase III, begin their high-fidelity replication of the
329 genome in opposite directions (?). *In vitro* measurements have shown that DNA Polymerase III copies DNA at a
330 rate of ≈ 600 nucleotides per second (BNID: 104120). Therefore, to replicate a single chromosome, two replisomes
331 moving at their maximal rate would copy the entire genome in ≈ 4000 s. Thus, with a division time of 5000 seconds,
332 there is sufficient time for a pair of replisomes complexes to replicate the entire genome.

333 In rapidly growing cultures, bacteria like *E. coli* can initiate as many as 10 - 12 replication forks at a given time (?),
334 we expect only a few DNA polymerases (≈ 10) are needed. However, as shown in **Figure 6**, DNA polymerase III is
335 nearly an order of magnitude more abundant. This discrepancy can be understood by considering its binding con-
336 stant to DNA. *In vitro* characterization has quantified the K_D of DNA polymerase III holoenzyme to single-stranded
337 and double-stranded DNA to be 50 and 200 nM, respectively (?). The right-hand plot in **Figure 6** shows that the
338 concentration of DNA polymerase III across all data sets is within this range. Thus, its copy number appears to vary
339 such that its concentration is approximately equal to the dissociation constant to the DNA. While the processes
340 regulating the initiation of DNA replication are complex and involve more than just the holoenzyme, these data
341 indicate that the kinetics of replication rather than the explicit copy number of the DNA polymerase III holoenzyme
342 is the more relevant feature of DNA replication to consider. In light of this, the data in **Figure 6** suggests that for
343 bacteria like *E. coli*, DNA replication does not represent a rate-limiting step in cell division. However, it is worth
344 noting that for bacterium like *C. crescentus* whose chromosomal replication is initiated only once per cell cycle (?),
345 the time to double their chromosome indeed represents an upper limit to their growth rate.

346 **RNA Synthesis**

347 We now turn our attention to the next stage of the central dogma – the transcription of DNA to form RNA. We
348 consider three major groupings of RNA, namely the RNA associated with ribosomes (rRNA), the RNA encoding the
349 amino-acid sequence of proteins (mRNA), and the RNA which links codon sequence to amino-acid identity during
350 translation (tRNA).

351 rRNA serves as the catalytic and structural component of the ribosome, comprising approximately 2/3 of the total
352 ribosomal mass, and is decorated with \approx 50 ribosomal proteins. Each ribosome contains three rRNA molecules
353 of lengths 120, 1542, and 2904 nucleotides (BNID: 108093), meaning each ribosome contains \approx 4500 nucleotides
354 overall. *In vivo* measurements of the kinetics of rRNA transcription have revealed that RNA polymerases are loaded
355 onto the promoter of an rRNA gene at a rate of \approx 1 per second (BNID: 111997, 102362). If RNA polymerases are
356 constantly loaded at this rate, then we can assume that \approx 1 functional rRNA unit is synthesized per second per
357 rRNA operon. While *E. coli* possesses 7 of these operons per chromosome, the fact that chromosome replication
358 can be parallelized means that the average dosage of rRNA genes can be substantially higher (up to \approx 70 copies)
359 at fast growth rates (?). At a growth rate of \approx 0.5 hr⁻¹, however, the average cell has \approx 1 copy of its chromosome
360 and therefore approximately \approx 7 copies of the rRNA operons, producing \approx 7 rRNA units per second. With a 5000
361 second division time, this means the cell is able to generate around 3×10^4 functional rRNA units, comparable
362 within an order of magnitude to the number of ribosomes per cell.

363 How many RNA polymerases are then needed to constantly transcribe the required rRNA? If one polymerase is
364 loaded per second, and the transcription rate is \approx 40 nucleotides per second (BNID: 101094), then the typical
365 spacing between polymerases will be \approx 40 nucleotides. However, we must note that the polymerase itself has a
366 footprint of \approx 40 nucleotides (BNID: 107873), meaning that one could expect to find one RNA polymerase per 80
367 nucleotide stretch of an rRNA gene. With a total length of \approx 4500 nucleotides per operon and 7 operons per cell,
368 the number of RNA polymerases transcribing rRNA at any given time is then \approx 500 per cell.

369 As outlined in *Figure 7*, and discussed further the Appendix Section "Additional Process of the Central Dogma",
370 synthesis of mRNA and tRNA together require on the order of \approx 400 RNAP. Thus, in total, one would expect
371 the typical cell to require \approx 1000 RNAP to satisfy its transcriptional demands. As is revealed in *Figure 7(B)*, this
372 estimate is about an order of magnitude below the observed number of RNA polymerase complexes per cell (\approx
373 5000 - 7000). The difference between the estimated number of RNA polymerase needed for transcription and
374 these observations, however, are consistent with literature revealing that \approx 80 % of RNA polymerases in *E. coli* are
375 not transcriptionally active (?), with the majority non-specifically bound to DNA.

376 Our estimates also neglect other mechanistic features of transcription and transcriptional initiation more
377 broadly. For example, we acknowledge that some fraction of the RNAP pool is nonspecifically bound to DNA
378 during its search for promoters from which to begin transcription. Furthermore, we ignore the obstacles that RNA
379 polymerase and DNA polymerase present to each other as they move along the DNA (?). Additionally, while they
380 represent the core machinery for transcription, RNA polymerase is not sufficient to initiate transcription. Initiation
381 of transcription is dependent on the presence of σ -factors, protein cofactors that bind directly to the polymerase
382 (?) and aid in promoter recognition. In *Figure 7–Figure Supplement 1*, we show that the predicted RNA polymerase
383 copy number indeed is more comparable with the abundance of σ -70 (RpoD), the primary sigma factor in *E. coli*.
384 There therefore remains more to be investigated as to what sets the observed abundance of RNA polymerase in
385 these proteomic data sets. However, we conclude that the observed RNA polymerase abundances are generally
386 in excess of what appears to be needed for growth, suggesting that the synthesis of RNA polymerase themselves
387 are not particularly limiting.

388 **Protein Synthesis**

389 We conclude our dialogue between back-of-the-envelope estimates and comparison with the proteomic data by
390 examining the final process in the central dogma – translation. In doing so, we will begin with an estimate of the
391 number of ribosomes needed to replicate the cellular proteome. While the rate at which ribosomes translate is
392 well known to be dependent on the growth rate (?), a phenomenon we consider later in this work) we begin by
393 making the approximation that translation occurs at a modest rate of \approx 15 amino acids per second per ribosome
394 (BNID: 100233). Under this approximation and our previous estimate of 10^9 peptide bonds per cell at a growth rate
395 of 0.5 hr⁻¹, we can easily arrive at an estimate of \approx 10^4 ribosomes needed per cell to replicate the entire protein

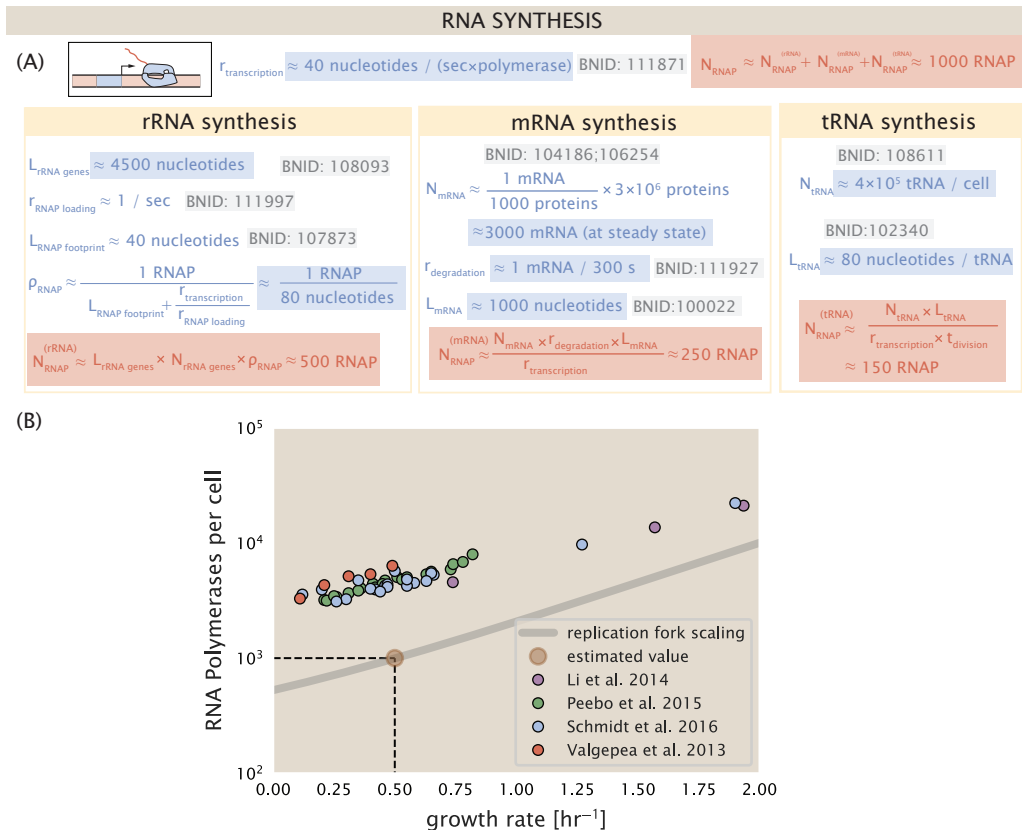


Figure 7. Estimation of the RNA polymerase demand and comparison with experimental data. (A) Estimations for the number of RNA polymerase needed to synthesize sufficient quantities of rRNA, mRNA, and tRNA from left to right, respectively. (B) The RNA polymerase core enzyme copy number as a function of growth rate. Colored points correspond to the average number RNA polymerase core enzymes that could be formed given a subunit stoichiometry of $[RpoA]_2[RpoC][RpoB]$.

Figure 7-Figure supplement 1. Abundance and growth rate dependence of σ -70.

396 mass (**Figure 8(A)**, top). This point estimate, as well as the corresponding estimate across a continuum of growth
397 rates, proves to be notably comparable to the experimental observations, shown in the bottom panel of **Figure 8(A)**.
398 While the ribosome is responsible for the formation of peptide bonds, we do not diminish the importance of
399 charging tRNAs with their appropriate amino acid, a process which occurs with remarkable fidelity. In the Appendix
400 and in **Figure 8–Figure Supplement 1**, we consider the process of ligating tRNAs to their corresponding amino acid
401 and again find notable accord between the data and our quantitative expectations.

402 Having completed our circuit through key processes of cellular growth outlined in **Figure 1**, we can now take
403 stock of our understanding of the observed growth rate dependence and abundances of various protein com-
404 plexes. We note that, broadly speaking, these simple estimates have been reasonably successful in quantitatively
405 describing the observations in the proteomic data, suggesting that the proteome is tuned in composition and
406 absolute abundance to match the growth rate requirements without any one process representing a singular bot-
407 tleneck or rate limiting step in division. However, in our effort to identify key limitations on growth, there are two
408 notable observations that we wish to emphasize.

409 The first is a recurring theme throughout the estimates investigated here, which is that any inherent biochem-
410 ical rate limitation can be overcome by expressing more proteins. We can view this as a parallelization of each
411 biosynthesis task, which helps explain why bacteria tend to increase their protein content (and cell size) as growth
412 rate increases (?). The second, and ultimately the most significant in defining the cellular growth rate, is that the
413 synthesis of ribosomal proteins presents a special case where parallelization is *not* possible and thereby imposes
414 a limit on the fastest possible growth rate. Each ribosome has \approx 7500 amino acids across all of its protein com-
415 ponents which must be strung together as peptide bonds through the action of another ribosome. Once again
416 using a modest elongation rate of \approx 15 amino acids per second, we arrive at an estimate of \approx 500 seconds or \approx
417 7 minutes to replicate a single ribosome. This limit, as remarked upon by others (?), serves as a hard theoretical
418 boundary for how quickly a bacterium like *E. coli* can replicate. As each ribosome would therefore need to copy
419 itself, this 7 minute speed limit is independent of the number of ribosomes per cell [**Figure 8(B)**], yet assumes
420 that the only proteins that need to be replicated for division to occur are ribosomal proteins, a regime not met
421 in biological reality. This poses an optimization problem for the cell – how are the translational demands of the
422 entire proteome met without investing resources in the production of an excess of ribosomes?

423 This question, more frequently presented as a question of optimal resource allocation, has been the target of
424 an extensive dialogue between experiment and theory over the past decade. In a now seminal work, ? present an
425 elegant treatment of resource allocation through partitioning of the proteome into sectors – one of which being
426 ribosome-associated proteins whose relative size ultimately defines the total cellular growth rate. In more recent
427 years, this view has been more thoroughly dissected experimentally (?????) and together have led to a paradigm-
428 shift in how we think of cellular physiology at the proteomic-level. However, the quantitative description of these
429 observations is often couched in terms of phenomenological constants and effective parameters with the key
430 observable features of expression often computed in relative, rather than absolute, abundances. Furthermore,
431 these approaches often exclude or integrate away effects of cell size and chromosome content, which we have
432 found through our estimates to have important connections to the observed cellular growth rate.

433 In the closing sections of this work, we explore how ribosomal content, total protein abundance, and chromo-
434 somal replication are intertwined in their control over the cellular growth rate. To do so, we take a more careful
435 view of ribosome abundance, increasing the sophistication of our analysis by exchanging our order-of-magnitude
436 estimates for a minimal mathematical model of growth rate control. This is defined by parameters with tangible
437 connections to the biological processes underlying cellular growth and protein synthesis. Using this model, we in-
438 terrogate how the size of the ribosome pool and its corresponding translational capacity enable cells to maintain
439 a balance between the supply of amino acids via metabolism and catabolism and their consumption through the
440 peptide bond formation required for growth.

441 **Maximum Growth Rate is Determined by the Ribosomal Mass Fraction**

442 The 7 minute speed limit shown in **Figure 8(B)** assumes all proteins in the cell are ribosomes. In order to connect
443 this to the experimental data (and physiological reality more broadly), we first need to relax this assumption and
444 determine a translation-limited growth rate. Here, we will assume that the cell is composed of N_{pep} peptide bonds
445 and R ribosomes, whose precise values will depend on the growth rate λ . The protein subunits of each ribosomal

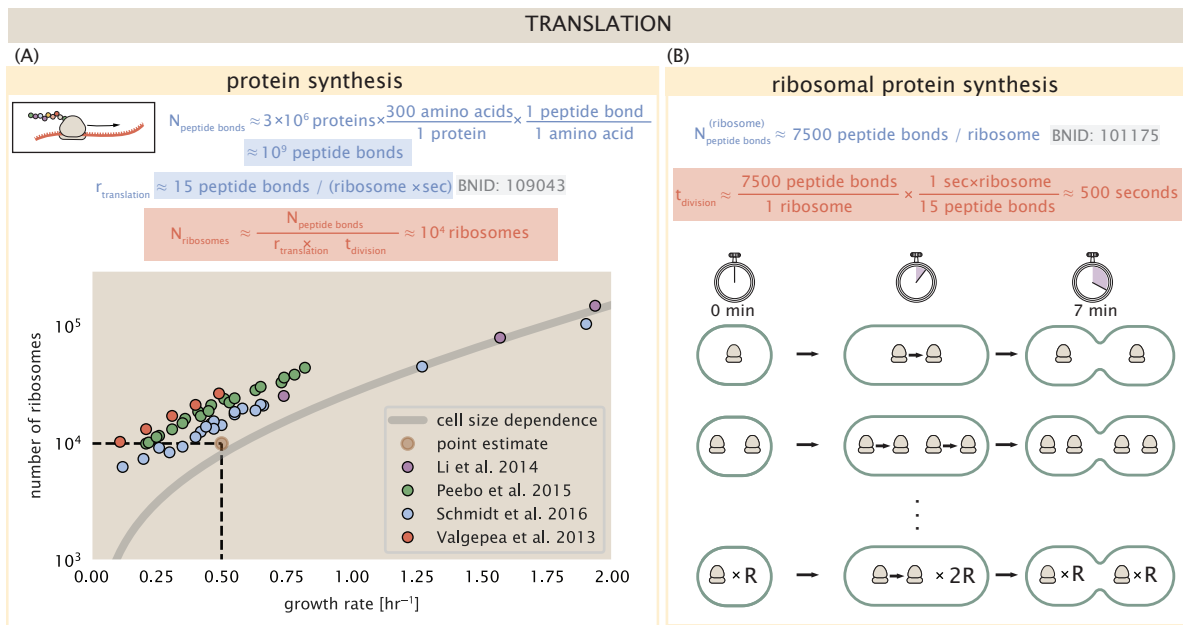


Figure 8. Estimation of the required number of ribosomes and the speed limit for bacterial replication. (A) Estimation of the number of ribosomes required to synthesize 10^9 peptide bonds with an elongation rate of 15 peptide bonds per second. The average abundance of ribosomes is plotted as a function of growth rate. Our estimated values are shown for a growth rate of 0.5 hr^{-1} . Grey lines correspond to the estimated complex abundance calculated at different growth rates. (B) Estimation for the time to replicate a ribosome. This rate is independent of the number of ribosomes R and instead is limited by the time required to double an individual ribosome.

Figure 8-Figure supplement 1. Estimate and observed abundance and growth rate dependence of tRNA ligases.

protein sum to a total of ≈ 7500 amino acids as noted earlier, which we denote by L_R . With an average mass of an amino acid of $m_{\text{AA}} \approx 110 \text{ Da}$ (BNID: 104877), the total ribosomal mass fraction Φ_R is given by

$$\Phi_R = \frac{m_{\text{ribosomes}}}{m_{\text{proteome}}} \approx \frac{m_{\text{AA}} \times R \times L_R}{m_{\text{AA}} \times N_{\text{pep}}} = \frac{R \times L_R}{N_{\text{pep}}}. \quad (1)$$

For exponentially growing cells (?), the rate of cellular growth will be related to the rate of protein synthesis via

$$\lambda N_{\text{pep}} = r_t \times R \times f_a, \quad (2)$$

where r_t is the translation rate. Here, we've introduced a multiplicative factor f_a which represents the fraction of the ribosomes that are actively translating. This term allows us to account for immature or non-functional ribosomes or active sequestration of ribosomes through the action of the secondary messenger alarmone (p)ppGpp in poorer nutrient conditions (?).

Combining **Equation 1** and **Equation 2** results in an expression for a translation-limited growth rate, which is given by

$$\lambda_{\text{translation-limited}} = \frac{r_t \times \Phi_R \times f_a}{L_R}. \quad (3)$$

This result, derived in a similar manner by others (??), reflects mass-balance under steady state growth and has long provided a rationalization of the apparent linear increase in *E. coli*'s ribosomal content as a function of growth rate (????). The left-hand panel of **Figure 9(A)** shows this growth rate plotted as a function of the ribosomal mass fraction. In the regime where all ribosomes are active ($f_a = 1$) and the entire proteome is composed of ribosomal proteins ($\Phi_R = 1$), indeed, we arrive at the maximum theoretical growth rate of r_t/L_R , and $\approx 7 \text{ min}$ for *E. coli*.

Connecting **Equation 3** to the proteomic data serving as the centerpiece of our work, however, requires knowledge of f_a at each growth rate as proteomic measurements only provide a measure of Φ_R . Recently, ? determined f_a as a function of the growth rate (**Figure 9(A)**, right-hand panel, inset), revealing that $f_a \approx 1$ at growth rates above 0.75 hr^{-1} and $f_a < 1$ as the growth rate slows. Using these data, we inferred the approximate active fraction (see the Appendix Section "Calculation of active ribosomal fraction") at each growth rate and used this to compute

465 $\Phi_R \times f_a$ (**Figure 9(A)**, colored points in right-hand panel). In general, these data skirt the translation-limited growth
 466 rate determined using **Equation 3**, where we have taken r_i to be the maximal elongation rate of 17 amino acids
 467 per second measured by **?**. There is a notable discrepancy between the data collected in **??** and that collected
 468 from **??**. When compared to other measurements (non-proteomic based) of the active ribosome mass fraction
 469 (**Figure 9(B)**, grey points in right-hand panel), the data from **?** and **?** are notably different, suggesting a systematic
 470 error in these data. These additional measurements come from a number of recent studies and are determined
 471 from measurements of total RNA to total protein mass ratios (**Figure 9–Figure Supplement 1**).

472 Together, these results illustrate that the growth rates observed across the amalgamated data sets are close
 473 to the translation-limited growth rate determined through ribosomal activity, at least for the data reported in
 474 **?** and **?**. While this is a useful framework to consider how the relative abundance of ribosomes (compared to
 475 all other proteins) defines the growth rate, it is worth noting that as growth rate increases, so does the cell size
 476 and therefore so will the total proteomic mass (**?**). With a handle on how elongation rate and the total number
 477 of peptide bonds per proteome is related to the growth rate, we now expand this description to account for the
 478 increasing cell size and ribosome copy number at faster growth rates, enabling us to identify a potential bottleneck
 479 in the synthesis of rRNA.

480 **rRNA Synthesis Presents a Potential Bottleneck During Rapid Growth**

481 Even under idealized experimental conditions, *E. coli* rarely exhibits growth rates above 2 hr^{-1} (**?**), which is still
 482 well-below the synthesis rate of a single ribosome, and below the maximum growth rates reported for several
 483 other bacteria (**?**). While we have considered potential limits imposed by translation of ribosomal *proteins*, here
 484 we consider potential limiting regimes specific to the synthesis of rRNA.

485 Due to multiple initiations of chromosomal replication per cell doubling, the effective number of rRNA operons
 486 increases with growth rate and will do so in proportion to the average number of origins per cell, $\langle \# \text{ ori} \rangle$. This later
 487 parameter is set by how often replication must be initiated in order to keep up with cell doubling times τ , whose
 488 time may be shorter than the cell cycle time τ_{cyc} (referring to the time from replication initiation to cell division)
 489 (**??**). This is quantified by

$$\langle \# \text{ ori} \rangle = 2^{\tau_{\text{cyc}}/\tau} = 2^{\tau_{\text{cyc}}\lambda/\log(2)}, \quad (4)$$

490 where the doubling time $s_0\tau$ is related to the growth rate by $\tau\alpha = \log(2)/\lambda$. We used the experimental measure-
 491 ments of τ_{cyc} (the timescale of chromosome replication and cell division) and τ (the timescale of a cell doubling)
 492 from **?** (**Figure 9–Figure Supplement 1(B)**) to calculate $\langle \# \text{ ori} \rangle$ with **Equation 4** as a function of growth rates. For
 493 growth rates above about 0.5 hr^{-1} , t_{cyc} is approximately constant at about 70 minutes, implying that $\langle \# \text{ ori} \rangle$ will
 494 grow exponentially with growth rates beyond 0.5 hr^{-1} . As the rRNA operons are predominantly located close to the
 495 origin of replication (BNID: 100352), we make the simplifying assumption that that the number of rRNA operons
 496 will be directly proportional to $\langle \# \text{ ori} \rangle$.

497 Returning to our rule-of-thumb of one functional rRNA unit is produced per second per transcribing operon, we
 498 estimate the maximum number of ribosomes that could be made as a function of growth rate (**Figure 9(B)**, blue
 499 curve). Although we expect this estimate to significantly overestimate rRNA abundance at slower growth rates
 500 ($\lambda < 0.5 \text{ hr}^{-1}$), this provides a useful reference alongside the proteomic measurements, particularly in the regime
 501 of fast growth. For growth rates above about 1 hr^{-1} , for example, we find that cells will need to transcribe rRNA
 502 near their maximal rate. As a counter example, if *E. coli* did not initiate multiple rounds of replication, but managed
 503 to replicate their chromosome within the requisite time limit, they would be unable to make enough rRNA for the
 504 observed number of ribosomes (dashed blue curve in **Figure 9(C)**). The convergence between the maximum rRNA
 505 production and measured ribosome copy number suggests rRNA synthesis may begin to present a bottleneck at
 506 the fastest growth rates due to the still-limited copies of rRNA genes.

507 **Rapid Growth Requires *E. coli* to Increase Both Cell Size and Ribosomal Mass Fraction**

508 In the right-hand side of **Figure 9(B)**, we also find that above about 0.75 hr^{-1} , the growth rate is determined solely
 509 by the ribosomal mass fraction Φ_R , since f_a is close to 1, and r_i is near its maximal rate (**?**). While Φ_R will need to
 510 increase in order for cells to grow faster, the fractional dependence in **Equation 3** gives little insight into how this
 511 scaling is actually achieved by the cell.

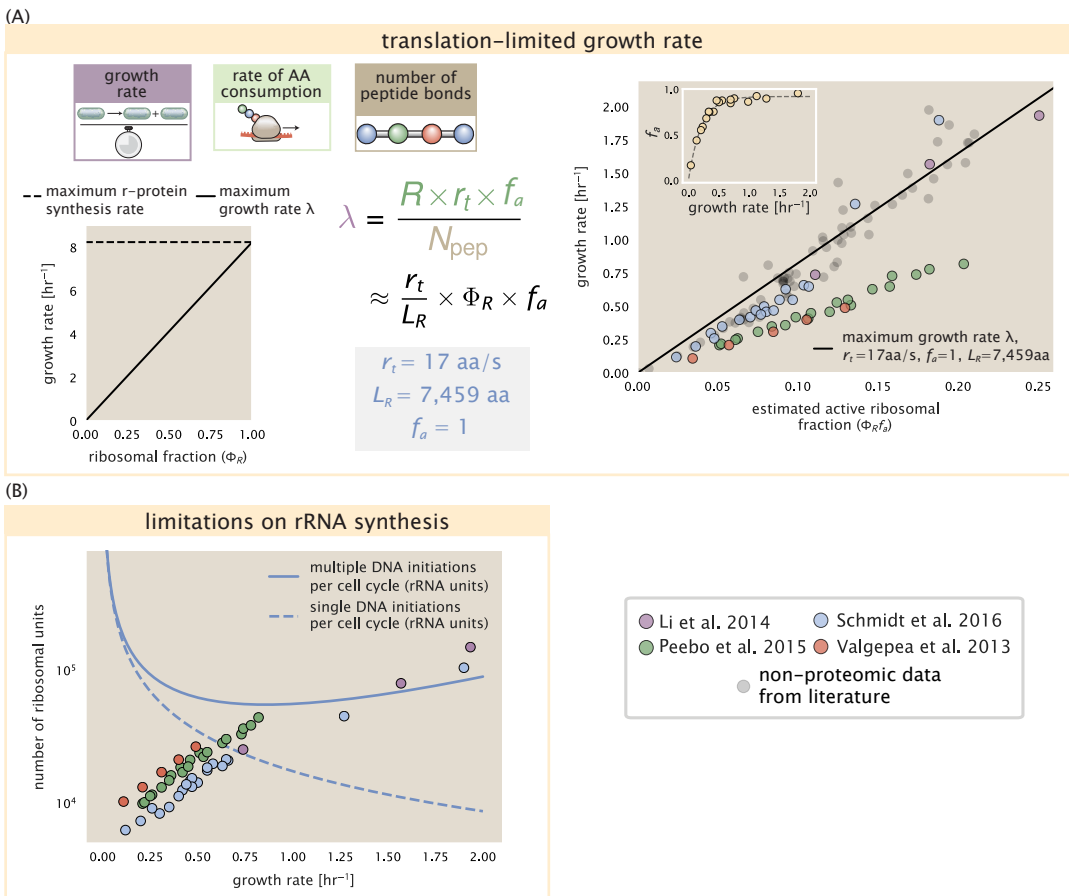


Figure 9. Translation-limited growth rate. (A) *left:* Translation-limited growth as a function of the ribosomal fraction. The solid line is calculated for an elongation rate of 17 aa per second. The dashed line corresponds to the maximum rate of ribosomal protein synthesis (≈ 7 min). *right:* Translation-limited growth rate as a function of the actively translating ribosomal fraction. The actively translating ribosomal fraction is calculated using the estimated values of f_a from ? (shown in inset; see Appendix Calculation of active ribosomal fraction for additional detail). Gray data points show additional measurements from literature and considered further in the supplemental figure part (A). (B) Maximum number of rRNA units that can be synthesized as a function of growth rate. Solid curve corresponding to the rRNA copy number is calculated by multiplying the number of rRNA operons by the estimated number of (# ori) at each growth rate. The quantity (<# ori>) was calculated using Equation 4 and the measurements from ?. The dashed line shows the maximal number of functional rRNA units produced from a single chromosomal initiation per cell cycle.

Figure 9–Figure supplement 1. Comparison of $\Phi_R f_a$ with literature and estimation of (<# ori>).

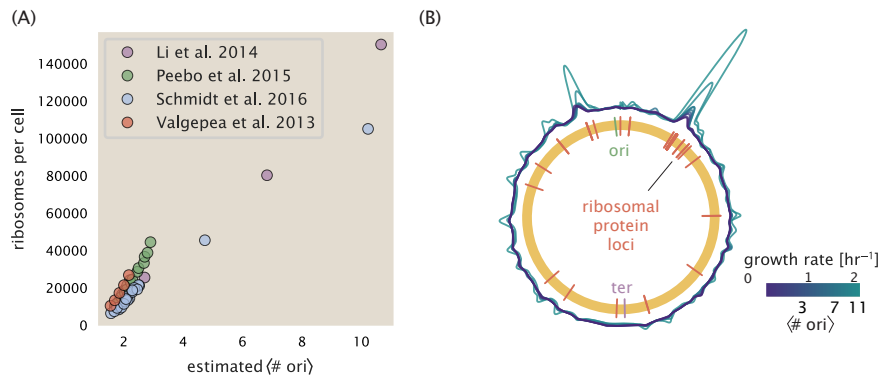


Figure 10. Cells increase both absolute ribosome abundance and Φ_R with $\langle \# \text{ori} \rangle$. (A) Plot of the ribosome copy number estimated from the proteomic data against the estimated $\langle \# \text{ori} \rangle$ (see Appendix Estimation of $\langle \# \text{ori} \rangle / \langle \# \text{ter} \rangle$ and $\langle \# \text{ori} \rangle$ for additional details). (B) A running Gaussian average (20 kbp st. dev.) of protein copy number is calculated for each growth condition considered by (?) based on each gene's transcriptional start site. Since total protein abundance increases with growth rate, protein copy numbers are median-subtracted to allow comparison between growth conditions. $\langle \# \text{ori} \rangle$ are estimated using the data in (A) and Equation 4.

It is now well-documented that *E. coli* cells add a constant volume per origin of replication, which is robust to a remarkable array of cellular perturbations (?). Given the proteomic measurements featured in this work, we find that the ribosome copy number also scales in proportion to $\langle \# \text{ori} \rangle$ (Figure 10(A)). However, an increase in ribosome abundance alone is not necessarily sufficient to increase growth rate and we also need to consider how Φ_R varies with $\langle \# \text{ori} \rangle$. Importantly, as shown in Figure 10(B), we find that the deviations in protein expression with $\langle \# \text{ori} \rangle$ are largely restricted to regions of ribosomal protein genes Figure 10(B). Here we have calculated the position-dependent protein expression across the chromosome by a running Gaussian average of protein copy number (20 kbp st. dev. averaging window) based on each gene's transcriptional start site. These were median-subtracted to account for the change in total protein abundance with $\langle \# \text{ori} \rangle$. This result suggests that Φ_R is also being tuned in proportion to $\langle \# \text{ori} \rangle$ under nutrient-limited growth, and in particular, it is through this additional dependence on Φ_R , combined with the exponential increase in $\langle \# \text{ori} \rangle$, that *E. coli* exhibits an exponential increase in cell size with growth rate.

524 A Minimal Model of Nutrient-Mediated Growth Rate Control

525 While the preceding subsections highlight a dominant role for ribosomes in setting the growth rate, our analysis
526 on the whole emphasizes how the total proteomic content also changes in response to variable growth conditions
527 and growth rate. In this final section we use a minimal model of growth rate control to better understand how
528 this interconnection between ribosomal abundance and total protein abundance influences the observed growth
529 rate.

530 Here we propose that cells modulate their protein abundance in direct response to the availability of nutrients
531 in their environment. As noted earlier, bacteria can modulate ribosomal activity through the secondary messenger
532 molecules like (p)ppGpp in poorer nutrient conditions (Figure 9(C) - inset; ?). Importantly, these secondary
533 messengers also cause global changes in transcriptional and translational activity (???). In *E. coli*, amino acid starva-
534 tion leads to the accumulation of de-acetylated tRNAs at the ribosome's A-site and a strong increase in (p)ppGpp
535 synthesis activity by the enzyme RelA (?). Along with this, there is increasing evidence that (p)ppGpp also acts to
536 inhibit the initiation of DNA replication (?), providing a potential mechanism for cells to lower $\langle \# \text{ori} \rangle$ and maintain
537 a smaller cell size in poorer nutrient conditions (?).

538 To consider this quantitatively, we assume that cells modulate their proteome (N_{pep} , R , Φ_R) to better maxi-
539 mize their rate of peptide elongation r_t . The elongation rate r_t will depend on how quickly the ribosomes can
540 match codons with their correct amino-acyl tRNA, along with the subsequent steps of peptide bond formation
541 and translocation. This ultimately depends on the cellular concentration of amino acids, which we treat as a sin-
542 gle effective species, $[AA]_{\text{eff}}$. In our model, we determine the the rate of peptide elongation r_t and achievable

543 growth rate as simply depending on the supply of amino acids (and, therefore, also amino-acyl tRNAs), through a
544 parameter r_{AA} in units of AA per second, and the rate of amino acid consumption by protein synthesis ($r_t \times R \times f_a$).
545 This is shown schematically in **Figure 11(A)** and derived in the Appendix Section "Derivation of Minimal Model for
546 Nutrient-Mediated Growth Rate Control". Given our observation that protein synthesis and energy production
547 are not limiting, we assume that other molecular players required by ribosomes such as elongation factors and
548 GTP are available in sufficient abundance.

549 In **Figure 11(B)**, we illustrate how the elongation rate will depend on the ribosomal copy number. Here, we
550 have considered an arbitrarily chosen $r_{AA} = 5 \times 10^6 \text{ AA} \cdot \text{s}^{-1} \cdot \mu\text{m}^{-3}$ and $f_a = 1$ for a unit cell volume $V = 1\text{fL}$ (we
551 provide the interactive figure **Figure 11–Figure Supplement 1** which allows the user to explore different regimes
552 of this parameter space). At low ribosome copy numbers, the observed elongation rate is dependent primarily on
553 $[AA]_{\text{eff}}$ through r_{AA} [as $r_t^{\max} \times R \times f_a \ll r_{AA}$, point (1) in **Figure 11(B)**]. As the ribosome copy number is increased
554 such that the amino acid supply rate and consumption rate are nearly equal [point (2) in **Figure 11(B)**], the ob-
555 served elongation rate begins to decrease sharply. When the ribosome copy number is increased even further,
556 consumption at the maximum elongation rate exceeds the supply rate, yielding a significantly reduced elongation
557 rate [point (3) in **Figure 11B**]. While the elongation rate will always be dominated by the amino acid supply rate
558 at sufficiently low ribosome copy numbers, the elongation rate at larger ribosome abundances can be increased
559 by tuning f_a such that not all ribosomes are elongating, reducing their total consumption rate.

560 Optimal Ribosomal Content and Cell Size Depend on Nutrient Availability and Metabolic Capacity
561 To relate elongation rate to growth rate, we constrain the set of parameters based on our available proteomic mea-
562 surements; namely, we restrict the values of R , N_{pep} , and cell size V to those associated with the amalgamated
563 proteomic data (described in the Appendix Section "Estimation of Total Protein Content per Cell"). We then con-
564 sider how changes in the nutrient conditions, through the parameter r_{AA} , influence the maximum growth rate as
565 determined by **Equation 3**. **Figure 11(C)** shows how the growth rate depends on the rate of amino acid supply r_{AA}
566 as a function of the cellular ribosome copy number. A feature immediately apparent is the presence of a maximal
567 growth rate whose dependence on R (and consequently, the cell size) increases with increasing r_{AA} . Importantly,
568 however, there is an optimum set of R , N_{pep} , and V that are strictly dependent on the value of r_{AA} . This shows that
569 increasing the ribosomal concentration beyond the cell's metabolic capacity will have the adverse consequence
570 of depleting the supply of amino acids and a concomitant decrease in the elongation rate r_t (**Figure 11(B)**) and
571 growth rate.

572 Also of note is the growth rate trends observed at low values of r_{AA} [purple and blue lines in **Figure 11(C)**],
573 representative of growth in nutrient-poor media. In these conditions, there no longer exists a peak in growth,
574 at least within the range of physiologically-relevant ribosome copy numbers. This is a regime, associated with
575 slower growth rates, where cells limit their pool of actively translating ribosomes by decreasing f_a (?), which we
576 find would help maintain the pool of available amino acids $[AA]_{\text{eff}}$ and increase the achievable elongation rate.

577 Discussion

578 Continued experimental and technological improvements have led to a treasure trove of quantitative biological
579 data (??????), and an ever advancing molecular view and mechanistic understanding of the constituents that sup-
580 port bacterial growth (??????). In this work we have compiled what we believe to be the state-of-the-art knowledge
581 on proteomic copy number across a broad range of growth conditions in *E. coli*. We have made this data accessible
582 through a [GitHub repository](#), and an [interactive figure](#) that allows exploration of specific protein and protein com-
583 plex copy numbers. Through a series of order-of-magnitude estimates that traverse key steps in the bacterial cell
584 cycle, this proteomic data has been a resource to guide our understanding of two key questions: what biological
585 processes limit the absolute speed limit of bacterial growth, and how do cells alter their molecular constituents
586 as a function of changes in growth rate or nutrient availability? While not exhaustive, our series of estimates pro-
587 vide insight on the scales of macromolecular complex abundance across four classes of cellular processes – the
588 transport of nutrients, the production of energy, the synthesis of the membrane and cell wall, and the numerous
589 steps of the central dogma.

590 In general, the copy numbers of the complexes involved in these processes were in reasonable agreement
591 with our order-of-magnitude estimates. Since many of these estimates represent soft lower-bound quantities, this

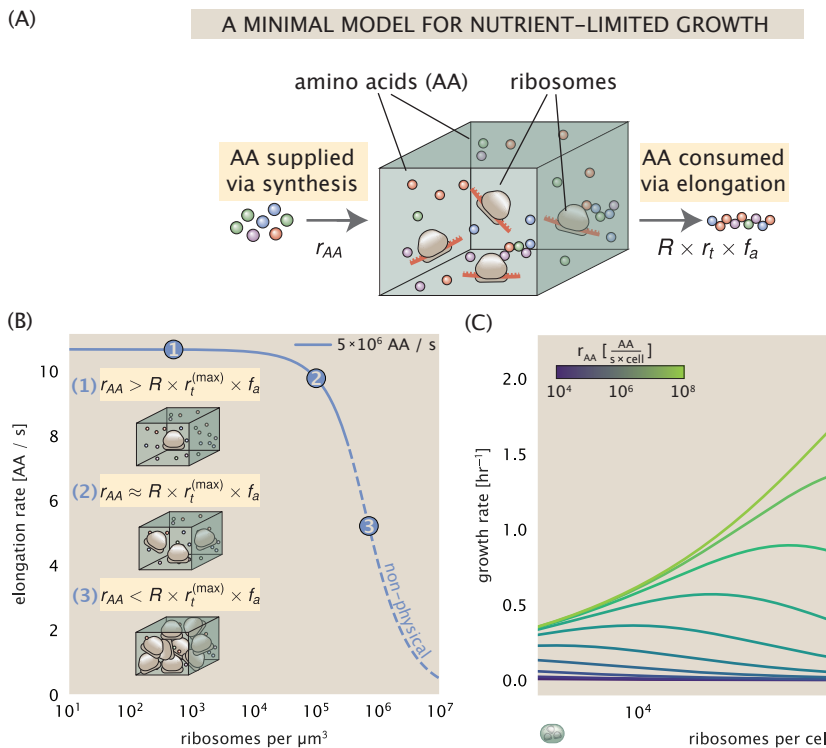


Figure 11. A minimal model of growth rate control under nutrient limitation. (A) We consider a unit volume of cellular material composed of amino acids (colored spheres) provided at a supply rate r_{AA} . These amino acids are polymerized by a pool of ribosomes (brown blobs) at a rate $r_t \times R \times f_a$, where r_t is the elongation rate, R is the ribosome copy number in the unit volume, and f_a is the fraction of those ribosomes actively translating. (B) The observed elongation rate is plotted as a function of the number of ribosomes. The three points correspond to three regimes of ribosome copy numbers and are shown schematically on the left-hand side. The region of the curve shown as dashed lines represents a non-physical copy number, but is shown for illustrative purposes. This curve was generated using an amino acid supply rate of 5×10^6 AA / s, a maximal elongation rate of 17.1 AA / s, $f_a = 1$, and a unit cell volume of $V = 1$ fL. See Appendix Derivation of Minimal Model for Nutrient-Mediated Growth Rate Control for additional model details. (C) The cellular growth rate is plotted as a function of total cellular ribosome copy number for different cellular amino acid supply rates, with blue and green curves corresponding to low and high supply rates, respectively. As the ribosome copy number is increased, so too is the cell size and total protein abundance N_{pep} . We direct the reader to the Supplemental Information for discussion on the inference of the relationship between cell size, number of peptide bonds, and ribosome copy number.

Figure 11–Figure supplement 1. An interactive figure for exploration of the model parameter space.

suggests that cells do not express proteins grossly in excess of what is needed for a particular growth rate. Several exceptions, however, also highlight the dichotomy between a proteome that appears to "optimize" expression according to growth rate and one that must be able to quickly adapt to environments of different nutritional quality. Take, for example, the expression of carbon transporters. Shown in *Figure 2(B)*, we find that cells always express a similar number of glucose transporters irrespective of growth condition. At the same time, it is interesting to note that many of the alternative carbon transporters are still expressed in low but non-zero numbers (\approx 10-100 copies per cell) across growth conditions. This may relate to the regulatory configuration for many of these operons, which require the presence of a metabolite signal in order for alternative carbon utilization operons to be induced (??). Furthermore, upon induction, these transporters are expressed and present in abundances in close agreement with a simple estimate.

Of the processes illustrated in *Figure 1*, we arrive at a ribosome-centric view of cellular growth rate control. This is in some sense unsurprising given the long-held observation that *E. coli* and many other organisms vary their ribosomal abundance as a function of growth conditions and growth rate (??). However, through our dialogue with the proteomic data, two additional key points emerge. The first relates to our question of what process sets the absolute speed limit of bacterial growth. While a cell can parallelize many of its processes simply by increasing the abundance of specific proteins or firing multiple rounds of DNA replication, this is not so for synthesis of ribosomes [*Figure 9(A)*]. The translation time for each ribosome [\approx 7 min, ?] places an inherent limit on the growth rate that can only be surpassed if the cell were to increase their polypeptide elongation rate, or if they could reduce the total protein and rRNA mass of the ribosome. The second point relates to the long-observed correlations between growth rate and cell size (??), and between growth rate and ribosomal mass fraction. While both trends have sparked tremendous curiosity and driven substantial amounts of research in their own regards, these relationships are themselves intertwined. In particular, it is the need for cells to increase their absolute number of ribosomes under conditions of rapid growth that require cells to also grow in size. Further experiments are needed to test the validity of this hypothesis. In particular, we believe that the change in growth rate in response to translation-inhibitory drugs (such as chloramphenicol) could be quantitatively predicted, given one had precision measurement of the relevant parameters, including the fraction of actively translating ribosomes f_a and changes in the metabolic capacity of the cell (i.e. the rate that amino acids can be made available) for a particular growth condition.

While the generation of new ribosomes plays a dominant role in growth rate control, there exist other physical limits to the function of cellular processes. One of the key motivations for considering energy production was the physical constraints on total volume and surface area as cells vary their size (??). As *E. coli* get larger at faster growth rates, an additional constraint begins to arise in energy production and nutrient uptake due to the relative decrease in total surface area, where ATP is predominantly produced (?). Specifically, the cell interior requires an amount of energy that scales cubically with cell size, but the available surface area only grows quadratically [*Figure 5(A)*]. While this threshold does not appear to be met for *E. coli* cells growing at 2 hr⁻¹ or less, it highlights an additional constraint on growth given the apparent need to increase cell size in order to grow faster. This limit is relevant even to eukaryotic organisms, whose mitochondria exhibit convoluted membrane structures that nevertheless remain bacteria-sized organelles (?). In the context of bacterial growth and energy production more generally, we have mainly limited our analysis to the aerobic growth conditions associated with the proteomic data and further consideration will be needed for anaerobic growth.¹

This work is by no means meant to be a complete dissection of bacterial growth rate control, and there are many aspects of the bacterial proteome and growth that we neglected to consider. For example, other recent work (???) has explored how the proteome is structured and how that structure depends on growth rate. In the work of ?, the authors coarse-grained the proteome into six discrete categories being related to either translation, catabolism, anabolism, and others related to signaling and core metabolism. The relative mass fraction of the proteome occupied by each sector could be modulated by external application of drugs or simply by changing the nutritional content of the medium. While we have explored how the quantities of individual complexes are related to cell growth, we acknowledge that higher-order interactions between groups of complexes or metabolic networks at a systems-level may reveal additional insights into how these growth-rate dependences are mechanistically achieved. Furthermore, while we anticipate the conclusions summarized here are applicable to a wide collection of bacteria with similar lifestyles as *E. coli*, other bacteria and archaea may have evolved other strate-

643 gies that were not considered. Further experiments with the level of rigor now possible in *E. coli* will need to be
644 performed in a variety of microbial organisms to learn more about how regulation of proteomic composition and
645 growth rate control has evolved over the past 3.5 billion years.

646 **Methods**

647 **Data Analysis and Availability**

648 All proteomic measurements come from the experimental work of ??? (mass spectrometry) and ? (ribosomal
649 profiling). Data curation and analysis was done programmatically in Python, and compiled data and analysis files
650 are accessible through a [GitHub repository](#) (DOI:XXX) associated with this paper as well as on the associated [paper](#)
651 [website](#). Additionally, we provide two interactive figures that allow for [rapid exploration of the compiled data sets](#)
652 as well as [exploration of the parameter space of the minimal model](#).

653 **Acknowledgements**

654 We thank Matthias Heinemann, Alexander Schmidt, and Gene-Wei Li for additional input regarding their data. We
655 also thank members of the Phillips, Theriot, Kondev, Garcia labs, as well as Ron Milo and Terry Hwa for useful
656 discussions. We thank Suzannah M. Beeler, Avi Flamholz, Soichi Hirokawa, and Manuel Razo-Mejia for reading
657 and providing comments on drafts of this manuscript. R.P. is supported by La Fondation Pierre-Gilles de Gennes,
658 the Rosen Center at Caltech, and the NIH 1R35 GM118043 (MIRA). J.A.T. is supported by the Howard Hughes
659 Medical Institute, and NIH Grant R37-AI036929. N.M.B is a HHMI Fellow of The Jane Coffin Childs Memorial Fund.
660 H.G.G. is supported by the Burroughs Wellcome Fund Career Award at the Scientific Interface, the Sloan Research
661 Foundation, the Human Frontiers Science Program, the Searle Scholars Program, the Shurl & Kay Curci Foundation,
662 the Hellman Foundation, the NIH Director's New Innovator Award (DP2 OD024541-01), and an NSF CAREER Award
663 (1652236). D.S.F. is supported by an NSF award (PHY-1607606).

664 **Competing Interests**

665 The authors declare no competing interests.

⁶⁶⁶ Appendix for: Fundamental limits on the ⁶⁶⁷ rate of bacterial growth

⁶⁶⁸ **Nathan M. Belliveau^{†, 1}, Griffin Chure^{†, 2}, Christina L. Hueschen³, Hernan G. Garcia⁴, Jane**
⁶⁶⁹ **Kondev⁵, Daniel S. Fisher⁶, Julie A. Theriot^{1, 7, *}, Rob Phillips^{8, 9, *}**

⁶⁷⁰ ¹Department of Biology, University of Washington, Seattle, WA, USA; ²Department of Applied Physics,
⁶⁷¹ California Institute of Technology, Pasadena, CA, USA; ³Department of Chemical Engineering,
⁶⁷² Stanford University, Stanford, CA, USA; ⁴Department of Molecular Cell Biology and Department of
⁶⁷³ Physics, University of California Berkeley, Berkeley, CA, USA; ⁵Department of Physics, Brandeis
⁶⁷⁴ University, Waltham, MA, USA; ⁶Department of Applied Physics, Stanford University, Stanford, CA,
⁶⁷⁵ USA; ⁷Allen Institute for Cell Science, Seattle, WA, USA; ⁸Division of Biology and Biological Engineering,
⁶⁷⁶ California Institute of Technology, Pasadena, CA, USA; ⁹Department of Physics, California Institute of
⁶⁷⁷ Technology, Pasadena, CA, USA; *Co-corresponding authors. Address correspondence to
⁶⁷⁸ phillips@pboc.caltech.edu and jtheriot@uw.edu; [†]These authors contributed equally to this work

679	Contents	
680	Introduction	1
681	Nutrient Transport	2
682	Limits on Transporter Expression	6
683	Cell Envelope Biogenesis	6
684	Lipid Synthesis	6
685	Peptidoglycan Synthesis	6
686	Limits on Cell Wall Biogenesis	7
687	Energy Production	7
688	ATP Synthesis	7
689	Generating the Proton Electrochemical Gradient	9
690	Limits on Biosynthesis in a Crowded Membrane	9
691	Processes of the Central Dogma	11
692	DNA Replication	12
693	RNA Synthesis	12
694	Protein Synthesis	13
695	Maximum Growth Rate is Determined by the Ribosomal Mass Fraction	15
696	rRNA Synthesis Presents a Potential Bottleneck During Rapid Growth	17
697	Rapid Growth Requires <i>E. coli</i> to Increase Both Cell Size and Ribosomal Mass Fraction	18
698	A Minimal Model of Nutrient-Mediated Growth Rate Control	18
699	Optimal Ribosomal Content and Cell Size Depend on Nutrient Availability and Metabolic Capacity	19
700	Discussion	21
701	Methods	22
702	Data Analysis and Availability	22
703	Acknowledgements	22
704	Competing Interests	23
705	Additional Estimates of Fundamental Biological Processes	26
706	Nutrient Transport	26
707	Nitrogen	26
708	Phosphorus	26
709	Sulfur	26
710	Additional Process of the Central Dogma	27
711	dNTP synthesis	27
712	mRNA and tRNA Synthesis	27
713	tRNA Charging	28
714	Experimental Details Behind Proteomic Data	29
715	Fluorescence based measurements	29
716	Ribosomal profiling measurements	29
717	Mass spectrometry measurements	30
718	Summary of Proteomic Data	30
719	Estimation of Cell Size and Surface Area	31

720	Estimation of Total Protein Content per Cell	32
721	Estimating Volume and Number of Amino Acids from Ribosome Copy Number	33
722	Additional Considerations of Schmidt <i>et al.</i> Data Set	33
723	Effect of cell volume on reported absolute protein abundances	35
724	Relaxing assumption of constant protein concentration across growth conditions	37
725	Comparison with total protein measurements from Basan <i>et al.</i> 2015.	37
726	Calculation of Complex Abundance	37
727	Extending Estimates to a Continuum of Growth Rates	39
728	Estimation of the total cell mass	40
729	Complex Abundance Scaling With Cell Volume	40
730	A Relation for Complex Abundance Scaling With Surface Area	41
731	Number of Lipids	41
732	Number of Murein Monomers	41
733	Complex Abundance Scaling With Number of Origins, and rRNA Synthesis	41
734	Calculation of active ribosomal fraction.	42
735	Estimation of $\langle \#ori \rangle / \langle \#ter \rangle$ and $\langle \#ori \rangle$.	42
736	Derivation of Minimal Model for Nutrient-Mediated Growth Rate Control	43

737 Additional Estimates of Fundamental Biological Processes

738 In the main text of this work, we present estimates for a significant number of fundamental biological processes
739 that are necessary for cell division. While we believe the estimates provided in the main text provide a succinct
740 summary of the corresponding process, we left out additional estimates of related processes for brevity. In this
741 section of the appendix, we present these additional estimates in full.

742 Nutrient Transport

743 In the main text, we make passing mention that while transport carbon often comes in the form of carbohydrates
744 and sugar alcohols while other critical elements – such as nitrogen, sulfur, and phosphorus – are transported as
745 inorganic ions. Below, we present estimates for the transport requirements of these materials.

746 Nitrogen

747 We must first address which elemental sources must require active transport, meaning that the cell cannot acquire
748 appreciable amounts simply via diffusion across the membrane. The permeability of the lipid membrane to a large
749 number of solutes has been extensively characterized over the past century. Large, polar molecular species (such
750 as various sugar molecules, sulfate, and phosphate) have low permeabilities while small, non-polar compounds
751 (such as oxygen, carbon dioxide, and ammonia) can readily diffuse across the membrane. Ammonia, a primary
752 source of nitrogen in typical laboratory conditions, has a permeability on par with water ($\sim 10^5$ nm/s, BNID:110824).
753 In nitrogen-poor conditions, *E. coli* expresses a transporter (AmtB) which appears to aid in nitrogen assimilation,
754 though the mechanism and kinetic details of transport are still a matter of debate (??). Beyond ammonia, another
755 plentiful source of nitrogen come in the form of glutamate, which has its own complex metabolism and scavenging
756 pathways. However, nitrogen is plentiful in the growth conditions examined in this work, permitting us to neglect
757 nitrogen transport as a potential rate limiting process in cell division in typical experimental conditions.

758 Phosphorus

759 Phosphorus is critical to the cellular energy economy in the form of high-energy phosphodiester bonds making
760 up DNA, RNA, and the NTP energy pool as well as playing a critical role in the post-translational modification of
761 proteins and defining the polar-heads of lipids. In total, phosphorus makes up $\approx 3\%$ of the cellular dry mass which
762 in typical experimental conditions is in the form of inorganic phosphate. The cell membrane has remarkably low
763 permeability to this highly-charged and critical molecule, therefore requiring the expression of active transport
764 systems. In *E. coli*, the proton electrochemical gradient across the inner membrane is leveraged to transport
765 inorganic phosphate into the cell (?). Proton-solute symporters are widespread in *E. coli* (??) and can have rapid
766 transport rates of 50 to 100 molecules per second for sugars and other solutes (BNID: 103159; 111777). As a
767 more extreme example, the proton transporters in the F₁-F₀ ATP synthase, which use the proton electrochemical
768 gradient for rotational motion, can shuttle protons across the membrane at a rate of ≈ 1000 per second (BNID:
769 104890; 103390). In *E. coli* the PitA phosphate transport system has been shown to be very tightly coupled with the
770 proton electrochemical gradient with a 1:1 proton:phosphate stoichiometric ratio (??). Taking the geometric mean
771 of the aforementioned estimates gives a plausible rate of phosphate transport on the order of 300 per second.
772 Illustrated in *Figure 2–Figure Supplement 1(A)*, we can estimate that ≈ 200 phosphate transporters are necessary
773 to maintain an $\approx 3\%$ dry mass with a 5000 s division time. This estimate is consistent with observation when we
774 examine the observed copy numbers of PitA in proteomic data sets (plot in *Figure 2–Figure Supplement 1(A)*). While
775 our estimate is very much in line with the observed numbers, we emphasize that this is likely a slight overestimate
776 of the number of transporters needed as there are other phosphorous scavenging systems, such as the ATP-
777 dependent phosphate transporter Pst system which we have neglected.

778 Sulfur

779 Similar to phosphate, sulfate is highly-charged and not particularly membrane permeable, requiring active trans-
780 port. While there exists a H⁺/sulfate symporter in *E. coli*, it is in relatively low abundance and is not well charac-
781 terized (?). Sulfate is predominantly acquired via the ATP-dependent ABC transporter CysUWA system which also
782 plays an important role in selenium transport (??). While specific kinetic details of this transport system are not
783 readily available, generic ATP transport systems in prokaryotes transport on the order of 1 to 10 molecules per

784 second (BNID: 109035). Combining this generic transport rate, measurement of sulfur comprising 1% of dry mass,
785 and a 5000 second division time yields an estimate of \approx 1000 CysUWA complexes per cell (**Figure 2–Figure Supple-**
786 **ment 1(B)**). Once again, this estimate is in notable agreement with proteomic data sets, suggesting that there are
787 sufficient transporters present to acquire the necessary sulfur. In a similar spirit of our estimate of phosphorus
788 transport, we emphasize that this is likely an overestimate of the number of necessary transporters as we have
789 neglected other sulfur scavenging systems that are in lower abundance.

790 Additional Process of the Central Dogma

791 In the main text, we consider the processes underlying the backbone of the central dogma, namely DNA replication,
792 RNA transcription, and protein translation. In this section we turn our attention to additional processes related
793 to the central dogma, primarily dNTP synthesis for DNA replication and amino-acyl tRNA synthesis for translation.
794 Additionally, we explore in more detail the estimates shown in **Figure 7(A)** for the RNA polymerase requirements
795 of mRNA and tRNA synthesis.

796 dNTP synthesis

797 The four major dNTPs (dATP, dTTP, dCTP, and dGTP) serve as the fundamental units of the genetic code. Thus, to
798 faithfully replicate the chromosome, the cell must be able to synthesize enough of these bases in the first place.
799 All dNTPs are synthesized *de novo* in separate pathways, requiring different building blocks. However, a critical
800 step present in all dNTP synthesis pathways is the conversion from ribonucleotide to deoxyribonucleotide via the
801 removal of the 3' hydroxyl group of the ribose ring (?). This reaction is mediated by a class of enzymes termed
802 ribonucleotide reductases, of which *E. coli* possesses two aerobically active complexes (termed I and II) and a
803 single anaerobically active enzyme. Due to their peculiar formation of a radical intermediate, these enzymes have
804 received much biochemical, kinetic, and structural characterization. One such work (?) performed a detailed *in*
805 *vitro* measurement of the steady-state kinetic rates of these complexes, revealing a turnover rate of \approx 10 dNTP
806 per second.

807 Since this reaction is central to the synthesis of all dNTPs, it is reasonable to consider the abundance of these
808 complexes as a measure of the total dNTP production in *E. coli*. Illustrated schematically in **Figure 6 (A)**, we consider
809 the fact that to replicate the cell's genome, on the order of \approx 10⁷ dNTPs must be synthesized. Assuming a pro-
810 duction rate of 10 per second per ribonucleotide reductase complex and a cell division time of 5000 seconds, we
811 arrive at an estimate of \approx 200 complexes needed per cell. As shown in the bottom panel of **Figure Supplement 1**
812 (A), this estimate agrees with the experimental measurements of these complexes abundances within \approx 1/2 an
813 order of magnitude. Extension of this estimate across a continuum of growth rate, including the fact that multiple
814 chromosomes can be replicated at a given time, is shown as a grey transparent line in **Figure Supplement 1**. Sim-
815 ilarly to our point estimate, this refinement agrees well with the data, accurately describing both the magnitude
816 of the complex abundance and the dependence on growth rate.

817 Recent work has revealed that during replication, the ribonucleotide reductase complexes coalesce to form
818 discrete foci colocalized with the DNA replisome complex (?). This is particularly pronounced in conditions where
819 growth is slow, indicating that spatial organization and regulation of the activity of the complexes plays an impor-
820 tant role.

821 mRNA and tRNA Synthesis

822 In **Figure 7** of the main text, we present with limited explanation estimates for the number of RNA polymerases
823 needed to synthesize enough mRNA and tRNA molecules. Here, we present a rationalization for these estimates.

824 To form a functional protein, all protein coding genes must first be transcribed from DNA to form an mRNA
825 molecule. While each protein requires an mRNA blueprint, many copies of the protein can be synthesized from
826 a single mRNA. Factors such as strength of the ribosomal binding site, mRNA stability, and rare codon usage
827 frequency dictate the number of proteins that can be made from a single mRNA, with yields ranging from 10¹
828 to 10⁴ (BNID: 104186; 100196; 106254). Computing the geometric mean of this range yields \approx 1000 proteins
829 synthesized per mRNA, a value that agrees with experimental measurements of the number of proteins per cell
830 (\approx 3 \times 10⁶, BNID: 100088) and total number of mRNA per cell (\approx 3 \times 10³, BNID: 100064).

831 This estimation captures the *steady-state* mRNA copy number, meaning that at any given time, there will exist
832 approximately 3000 unique mRNA molecules. To determine the *total* number of mRNA that need to be synthesized
833 over the cell's lifetime, we must consider degradation of the mRNA. In most bacteria, mRNAs are rather unstable
834 with life times on the order of several minutes (BNID: 104324; 106253; 111927; 111998). For convenience, we
835 assume that the typical mRNA in our cell of interest has a typical lifetime of \approx 300 seconds. Using this value, we
836 can determine the total mRNA production rate to maintain a steady-state copy number of 3000 mRNA per cell.
837 While we direct the reader to the appendix for a more detailed discussion of mRNA transcriptional dynamics, we
838 state here that the total mRNA production rate must be on the order of \approx 15 mRNA per second. In *E. coli*, the
839 average protein is \approx 300 amino acids in length (BNID: 108986), meaning that the corresponding mRNA is \approx 900
840 nucleotides which we will further approximate as \approx 1000 nucleotides to account for the non-protein coding regions
841 on the 5' and 3' ends. This means that the cell must have enough RNA polymerase molecules about to sustain a
842 transcription rate of $\approx 1.5 \times 10^4$ nucleotides per second. Knowing that a single RNA polymerase polymerizes RNA
843 at a clip of 40 nucleotides per second, we arrive at a comfortable estimate of \approx 250 RNA polymerase complexes
844 needed to satisfy the mRNA demands of the cell. It is worth noting that this number is approximately half of that
845 required to synthesize enough rRNA, as we saw in the previous section. We find this to be a striking result as these
846 250 RNA polymerase molecules are responsible for the transcription of the \approx 4000 protein coding genes that are
847 not ribosome associated.

848 We now turn our attention to the synthesis of tRNA. Unlike mRNA or rRNA, each individual tRNA is remarkably
849 short, ranging from 70 to 95 nucleotides each (BNID: 109645; 102340). What they lack in length, they make up
850 for in abundance, with reported values ranging from $\approx 5 \times 10^4$ (BNID: 105280) to $\approx 5 \times 10^5$ (BNID: 108611). To test
851 tRNA synthesis as a possible growth-rate limiting stage, we will err towards a higher abundance of $\approx 5 \times 10^5$ per
852 cell. Combining the abundance and tRNA length measurements, we make the estimate that $\approx 5 \times 10^7$ nucleotides
853 are sequestered in tRNA per cell. Unlike mRNA, tRNA is remarkably stable with typical lifetimes *in vivo* on the
854 order of \approx 48 hours (??) – well beyond the timescale of division. Once again using our rule-of-thumb for the
855 rate of transcription to be 40 nucleotides per second and assuming a division time of \approx 5000 seconds, we arrive
856 at an estimate of \approx 200 RNA polymerases to synthesize enough tRNA. This requirement pales in comparison to
857 the number of polymerases needed to generate the rRNA and mRNA pools and can be neglected as a significant
858 transcriptional burden.

859 tRNA Charging

860 In the previous subsection, we focused solely on estimating the number of RNA polymerases needed for the
861 generation of the tRNA molecule itself. We now explore the protein complex requirements for ligation of the
862 appropriate amino acid to each tRNA. We begin by again using an estimate of $\approx 3 \times 10^6$ proteins per cell at a 5000
863 s division time (BNID: 115702) and a typical protein length of \approx 300 amino acids (BNID: 100017), we can estimate
864 that a total of $\approx 10^9$ amino acids are stitched together by peptide bonds.

865 How many tRNAs are needed to facilitate this remarkable number of amino acid delivery events to the trans-
866 lating ribosomes? It is important to note that tRNAs are recycled after they've passed through the ribosome and
867 can be recharged with a new amino acid, ready for another round of peptide bond formation. While some *in vitro*
868 data exists on the turnover of tRNA in *E. coli* for different amino acids, we can make a reasonable estimate by
869 comparing the number of amino acids to be polymerized to cell division time. Using our stopwatch of 5000 s and
870 10^9 amino acids, we arrive at a requirement of $\approx 2 \times 10^5$ tRNA molecules to be consumed by the ribosome per
871 second.

872 There are many processes which go into synthesizing a tRNA and ligating it with the appropriate amino acids.
873 As we discussed previously, there appear to be more than enough RNA polymerases per cell to synthesize the
874 needed pool of tRNAs. Without considering the many ways in which amino acids can be scavenged or synthesized
875 *de novo*, we can explore ligation as a potential rate limiting step. The enzymes which link the correct amino
876 acid to the tRNA, known as tRNA synthetases or tRNA ligases, are incredible in their proofreading of substrates
877 with the incorrect amino acid being ligated once out of every 10^4 to 10^5 events (BNID: 103469). This is due in part
878 to the consumption of energy as well as a multi-step pathway to ligation. While the rate at which tRNA is ligated is
879 highly dependent on the identity of the amino acid, it is reasonable to state that the typical tRNA synthetase has
880 a charging rate of \approx 20 AA per tRNA synthetase per second (BNID: 105279).

Table 1. Overview of proteomic data sets.

Author	Method	Reported Quantity
Taniguchi <i>et al.</i> (2010)	YFP-fusion, cell fluorescence	fg/copies per cell
Valgepea <i>et al.</i> (2012)	mass spectrometry	fg/copies per cell
Peebo <i>et al.</i> (2014)	mass spectrometry	fg/copies per fl
Li <i>et al.</i> (2014)	ribosomal profiling	fg/copies per cell ^a
Soufi <i>et al.</i> (2015)	mass spectrometry	fg/copies per cell
Schmidt <i>et al.</i> (2016)	mass spectrometry	fg/copies per cell ^b

a. The reported values assume that the proteins are long-lived compared to the generation time but are unable to account for post-translational modifications that may alter absolute protein abundances.

b. This mass spectrometry approach differs substantially from the others since in addition to the relative proteome-wide abundance measurements, the authors performed absolute quantification of 41 proteins across all growth conditions (see section on Additional Considerations of Schmidt *et al.* Data Set for more details on this).

We can make an assumption that amino-acyl tRNAs are in steady-state where they are produced at the same rate they are consumed, meaning that 2×10^5 tRNAs must be charged per second. Combining these estimates together, as shown schematically in **Figure 8–Figure Supplement 1**, yields an estimate of $\sim 10^4$ tRNA synthetases per cell with a division time of 5000 s. This point estimate is in very close agreement with the observed number of synthetases (the sum of all 20 tRNA synthetases in *E. coli*). This estimation strategy seems to adequately describe the observed growth rate dependence of the tRNA synthetase copy number (shown as the grey line in **Figure 8–Figure Supplement 1**, suggesting that the copy number scales with the cell volume.

In total, the estimated and observed $\sim 10^4$ tRNA synthetases occupy only a meager fraction of the total cell proteome, around 0.5% by abundance. It is reasonable to assume that if tRNA charging was a rate limiting process, cells would be able to increase their growth rate by devoting more cellular resources to making more tRNA synthetases. As the synthesis of tRNAs and the corresponding charging can be highly parallelized, we can argue that tRNA charging is not a rate limiting step in cell division, at least for the growth conditions explored in this work.

Experimental Details Behind Proteomic Data

Here we provide a brief summary of the experiments behind each proteomic data set considered. The purpose of this section is to identify how the authors arrived at absolute protein abundances. In the following section (see section on Summary of Proteomic Data) we will then provide a summary of the protein abundance measurements. Table 1 provides an overview of the publications we considered. These are predominately mass spectrometry-based, with the exception of the work from ? which used ribosomal profiling, and the fluorescence-based counting done in ?. After having compiled and comparing these measurements, we noted substantial deviations in the measurements from ? and ? (shown in the following section), and decided to only use the data from ??? in the main text. For completeness, we include these additional datasets in our discussion of the experimental data.

Fluorescence based measurements

In the work of ?, the authors used a chromosomal YFP fusion library where individual strains have a specific gene tagged with a YFP-coding sequence. 1018 of their 1400 attempted strains were used in the work. A fluorescence microscope was used to collect cellular YFP intensities across all these strains. Through automated image analysis, the authors normalized intensity measurements by cell size to account for the change in size and expression variability across the cell cycle. Following correction of YFP intensities for cellular autofluorescence, final absolute protein levels were determined by a calibration curve with single-molecule fluorescence intensities. This calibration experiment was performed separately using a purified YFP solution.

Ribosomal profiling measurements

The work of ? takes a sequencing based approach to estimate protein abundance. Ribosomal profiling, which refers to the deep sequencing of ribosome-protected mRNA fragments, can provide a quantitative measurement

913 of the protein synthesis rate. As long as the protein life-time is long relative to the cell doubling time, it is possible to
914 estimate absolute protein copy numbers. The absolute protein synthesis rate has units of proteins per generation,
915 and for stable proteins will also correspond to the protein copy number per cell.

916 In the experiments, ribosome-protected mRNA is extracted from cell lysate and selected on a denaturing poly-
917 acrylamide gel for deep sequencing (15–45 nt long fragments collected and sequenced by using an Illumina HiSeq
918 2000 in ?). Counts of ribosome footprints from the sequencing data were then corrected empirically for position-
919 dependent biases in ribosomal density across each gene, as well as dependencies on specific sequences including
920 the Shine-Dalgarno sequence. These data-corrected ribosome densities represent relative protein synthesis rates.
921 Absolute protein synthesis rates are obtained by multiplying the relative rates by the total cellular protein per cell.
922 The total protein per unit volume was determined with the Lowry method to quantify total protein, calibrated
923 against bovine serum albumin (BSA). By counting colony-forming units following serial dilution of their cell cul-
924 tures, they then calculated the total protein per cell.

925 Mass spectrometry measurements

926 Perhaps not surprisingly, the data is predominantly mass spectrometry based. This is largely due to tremendous
927 improvements in the sensitivity of mass spectrometers, as well as improvements in sample preparation and data
928 analysis pipelines. It is now a relatively routine task to extract protein from a cell and quantify the majority of
929 proteins present by shotgun proteomics. In general, this involves lysing cells, enzymatically digesting the proteins
930 into short peptide fragments, and then introducing them into the mass spectrometer (e.g. with liquid chromatog-
931 raphy and electrospray ionization), which itself can have multiple rounds of detection and further fragmentation
932 of the peptides.

933 Most quantitative experiments rely on labeling protein with stable isotopes, which allow multiple samples to
934 be measured together by the mass spectrometer. By measuring samples of known total protein abundance sim-
935 taneously (i.e. one sample of interest, and one reference), it is possible to determine relative protein abundances.
936 Absolute protein abundances can be estimated following the same approach used above for ribosomal profiling,
937 which is to multiply each relative abundance measurement by the total cellular protein per cell. This is the ap-
938 proach taken by ?? and ?, with relative protein abundances determined based on the relative peptide intensities
939 (label free quantification 'LFQ' intensities). For the data of ?, total protein per cell was determined by measuring
940 total protein by the Lowry method, and counting colony-forming units following serial dilution. For the data from
941 ?, the authors did not determine cell quantities and instead report the cellular protein abundances in protein per
942 unit volume by assuming a mass density of 1.1 g/ml, with a 30% dry mass fraction.

943 An alternative way to arrive at absolute protein abundances is to dope in synthetic peptide fragments of known
944 abundance. These can serve as a direct way to calibrate mass spectrometry signal intensities to absolute mass.
945 This is the approach taken by ?. In addition to a set of shotgun proteomic measurements to determine proteome-
946 wide relative abundances, the authors also performed absolute quantification of 41 proteins covering over four
947 orders of magnitude in cellular abundance. Here, a synthetic peptide was generated for each of the proteins,
948 doped into each protein sample, and used these to determine absolute protein abundances of the 41 proteins.
949 These absolute measurements, determined for every growth condition, were then used as a calibration curve to
950 convert proteomic-wide relative abundances into absolute protein abundance per cell. A more extensive discus-
951 sion of the ? data set can be found in Section Additional Considerations of Schmidt *et al.* Data Set.

952 Summary of Proteomic Data

953 In the work of the main text we only used the data from ?????. As shown in **Figure 12(A)**, the reported total protein
954 abundances in the work of ? and ? differed quite substantially from the other work. For the work of ? this is in part
955 due to a lower coverage in total proteomic mass quantified, though we also noticed that most proteins appear
956 undercounted when compared to the other data.

957 **Figure 12(B)** summarizes the total protein mass for each data set used in our final compiled data set. Our
958 inclination initially was to leave reported copy numbers untouched, but a notable descrepency between the scaling
959 of the total protein per cell between ? and the other data sets forced us to dig deeper into those measurements
960 (compare ? and ? data in **Figure 12(A)**). The particular trend in ? appears to be due to assumptions made about cell
961 size and we provide a more extensive discussion and analysis of their data in Additional Considerations of Schmidt

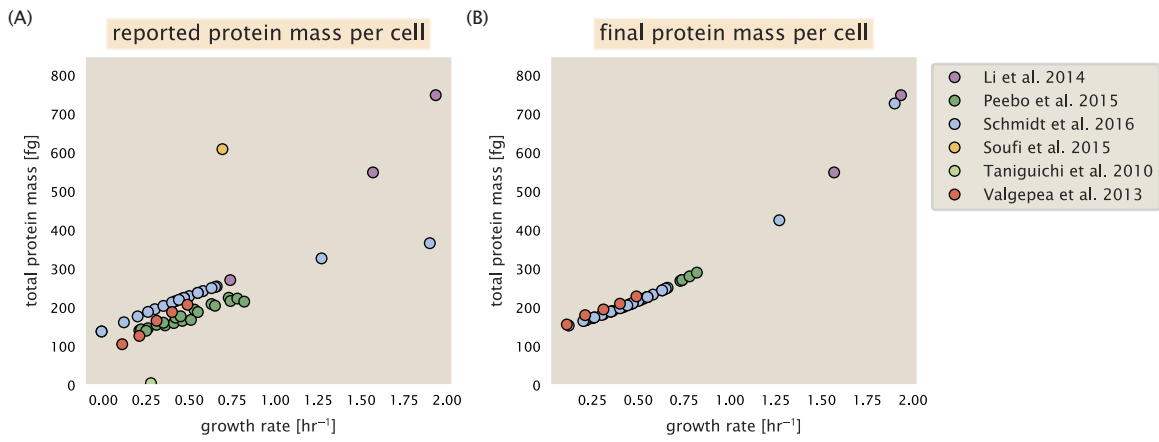


Figure 12. Summary of the growth-rate dependent total protein abundance for each data set. (A) Total protein abundance per cell as originally reported in the data sets of ??????. Note that the data from ? only reported protein abundances per unit volume and total protein per cell was found by multiplying these by the growth-rate dependent cell size as determined by ?. (B) Adjusted total protein abundances across the proteomic data sets are summarized. Protein abundances were adjusted so that all data shared a common set of growth-rate dependent total protein per cell and cellular protein concentration following the cell size expectations of ? (see section on Estimation of Cell Size and Surface Area for further details).

et al. Data Set. As a compromise, and in an effort to treat all data equally, we instead applied an correction factor to all protein abundance values based on a data-driven estimate of total protein per cell. Here we used cell size measurements from ??, and an estimate of total protein content through expected dry mass. Total protein per cell was then determined using available data on total DNA, RNA, and protein from ??, which account for the majority of dry mass in the cell. We describe these details further in sections on Estimation of Cell Size and Surface Area and Estimation of Total Protein Content per Cell that follows.

Lastly, in *Figure 13* we show the total proteomic coverage and overlap of proteins quantified across each data set. In part (A) we plot the total number of unique proteins, while in part (B) we plot a Venn diagram to also show the intersections across each data set. Overall, the overlap in quantified proteins is quite high, with 1157 proteins quantified across all data sets. The sequencing based approach of ? has substantially higher coverage compared to the mass spectrometry data sets (3394 genes versus the 2041 genes quantified in the work of ?). However, in terms of total protein mass, the data from ??? each quantify roughly equivalent total protein mass. An exception to this is in the data from ?, where we find that the total protein quantified in ? is 90-95 % of the total protein mass (when using the data from ? as a reference).

Estimation of Cell Size and Surface Area

Since most of the proteomic data sets lack cell size measurements, we chose instead to use a common estimate of size for any analysis requiring cell size or surface area. Since each of the data sets used either K-12 MG1655 or its derivative, BW25113 (from the lab of Barry L. Wanner; the parent strain of the Keio collection (??)), below we fit the MG1655 cell size data from the supplemental material of ?? using the optimize.curve_fit function from the Scipy python package (?). A quick comment on nomenclature: throughout the text, we usually refer to cell size, in units of μm^3 ; however, on occasion we will mention size as a volume in units of fL.

The average size measurements from each of their experiments are shown in *Figure 14*, with cell length and width shown in (A) and (B), respectively. The length data was well described by the exponential function $0.5 e^{1.09 \cdot \lambda} + 1.76 \mu\text{m}$, while the width data was well described by $0.64 e^{0.24 \cdot \lambda} \mu\text{m}$. In order to estimate cell size we take the cell as a cylinder with two hemispherical ends (??). Specifically, cell size is estimated from,

$$V = \pi \cdot r^2 \cdot (l - 2r/3), \quad (5)$$

where r is half the cell width. A best fit to the data is described by $0.533 e^{1.037 \cdot \lambda} \mu\text{m}^3$. Calculation of the cell surface

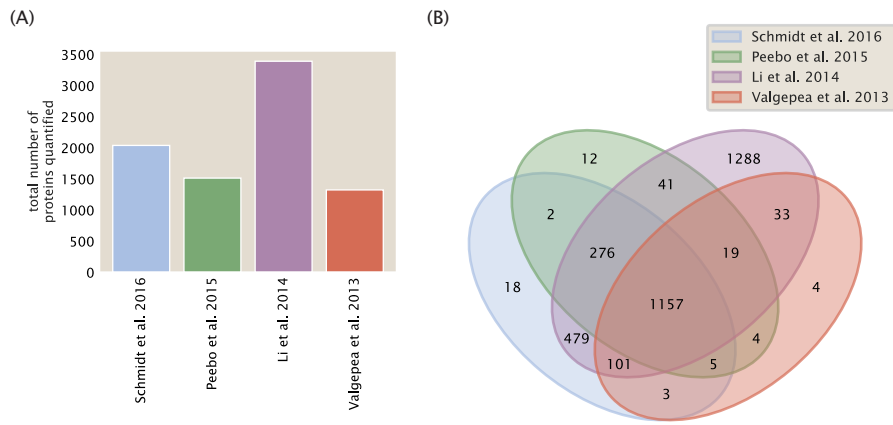


Figure 13. Comparison of proteomic coverage across different data sets. (A) Total number of unique proteins quantified in the data sets of **?????**. (2) Venn diagram showing the number of unique proteins and their intersections across each of the four data sets in (A). The intersection of all four data sets identifies 1157 proteins with measured protein copy number values. The intersection of each of the shaded colors identifies the number of unique proteins quantified only in those overlapping data sets.

area is given by,

$$S = \eta \cdot \pi \left(\frac{\eta \cdot \pi}{4} - \frac{\pi}{12} \right)^{-2/3} V^{2/3}, \quad (6)$$

where η is the aspect ratio ($\eta = l/w$) (?).

Estimation of Total Protein Content per Cell

In order to estimate total protein per cell for a particular growth rate, we begin by estimating the cell size from the fit shown in **Figure 14(C)** (cell size = $0.533 e^{1.037 \cdot \lambda} \mu\text{m}^3$, as noted in the previous section). We then estimate the total protein content from the total dry mass of the cell. Here we begin by noting that for almost the entire range of growth rates considered here, protein, DNA, and RNA were reported to account for at least 90 % of the dry mass (?). The authors also found that the total dry mass concentration was roughly constant across growth conditions. Under such a scenario, we can calculate the total dry mass concentration for protein, DNA, and RNA, which is given by $1.1 \text{ g/ml} \times 30 \% \times 90 \% \text{ or about } [M_p] = 300 \text{ fg per fL}$. Multiplying this by our prediction of cell size gives the total dry mass per cell.

However, even if dry mass concentration is relatively constant across growth conditions, it is not obvious how protein concentration might vary due to the substantial increase in rRNA at faster growth rates (?). The increase in rRNA increases from the linear increase in ribosomal content with faster growth rate (?), since it makes up about 2/3 of the ribosomal mass. To proceed we therefore relied on experimental measurements of total DNA content per cell from ?, and RNA to protein ratios that were measured in Dai *et al.* (and cover the entire range of growth conditions considered here). These are reproduced in **Figure 15(A)** and (B), respectively.

Assuming that the protein, DNA, and RNA account for 90 % of the total dry mass, the protein mass can then be determined by first subtracting the experimentally measured DNA mass, and then using the experimental estimate of the RNA to protein ratio. The total protein per cell will be related to the summed RNA and protein mass by,

$$M_p = \frac{[M_p + M_{RNA}]}{1 + (RP_{ratio})}. \quad (7)$$

(RP_{ratio} refers to the RNA to protein ratio as measured by Dai *et al.*. In **Figure 15(C)** we plot the estimated cellular concentrations for protein, DNA, and RNA from these calculations, and in **Figure 15(D)** we plot their total expected mass per cell. This latter quantity is the growth rate-dependent total protein mass that was used to estimate total protein abundance across all data sets (and summarized in **Figure 12(B)**).

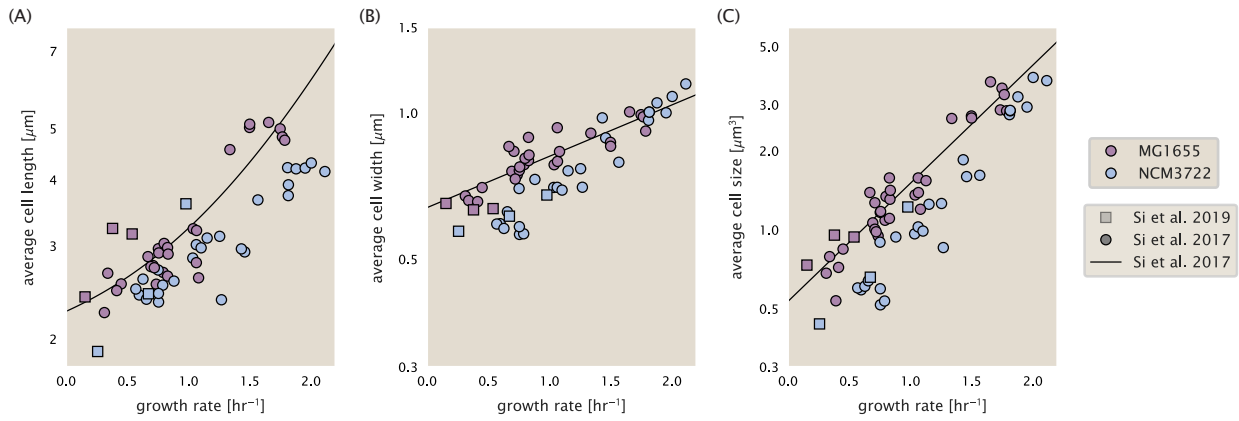


Figure 14. Summary of size measurements from Si et al. 2017, 2019. Cell lengths and widths were measured from cell contours obtained from phase contrast images, and refer to the long and short axis respectively. (A) Cell lengths and (B) cell widths show the mean measurements reported (they report 140-300 images and 5,000-30,000 for each set of samples; which likely means about 1,000-5,000 measurements per mean value reported here since they considered about 6 conditions at a time). Fits were made to the MG1655 strain data; length: $0.5 e^{1.09 \cdot \lambda} + 1.76 \mu\text{m}$, width: $0.64 e^{0.24 \cdot \lambda} \mu\text{m}$. (C) Cell size was calculated as cylinders with two hemispherical ends (Equation 5). The MG1655 strain data gave a best fit of $0.533 e^{1.037 \cdot \lambda} \mu\text{m}^3$.

1012 Estimating Volume and Number of Amino Acids from Ribosome Copy Number

1013 Towards the end of the main text, we examine a coarse-grained model of nutrient-limited growth. A key point
 1014 in our analysis was to consider how elongation rate r_e and growth rate λ vary with respect to the experimentally
 1015 observed changes in cell size, total number of peptide bonds per cell N_{pep} , and ribosomal content. In order to
 1016 restrict parameters to those observed experimentally, but otherwise allow us to explore the model, we performed
 1017 a phenomenological fit of N_{pep} and V as a function of the measured ribosomal copy number R . As has been
 1018 described in the preceding sections of this supplement, we estimate cell volume for each growth condition using
 1019 the size measurements from ??, and N_{pep} is approximated by taking the total protein mass and dividing this
 1020 number by the average mass of an amino acid, 110 Da (BNID: 104877).

1021 Given the exponential scaling of V and N_{pep} with growth rate, we performed a linear regression of the log trans-
 1022 form of these parameters as a function of the log transform of the ribosome copy number. Using optimization
 1023 by minimization, we estimated the best-fit values of the intercept and slope for each regression. **Figure 16** shows
 1024 the result of each regression as a dashed line.

1025 Additional Considerations of Schmidt et al. Data Set

1026 While the data set from ? remains a heroic effort that our labs continue to return to as a resource, there were
 1027 steps taken in their calculation of protein copy number that we argue needed further consideration. In particular,
 1028 the authors made an assumption of constant cellular protein concentration across all growth conditions and
 1029 used measurements of cell volume that appear inconsistent with an expected exponential scaling of cell size
 1030 with growth rate that is well-documented in *E. coli* (??).

1031 We begin by looking at their cell volume measurements, which are shown in blue in Figure **Figure 17**. As a
 1032 comparison, we also plot cell sizes reported in three other recent papers: measurements from Taheri-Araghi *et*
 1033 *al.* and Si *et al.* come from the lab of Suckjoon Jun, while those from Basan *et al.* come from the lab of Terence
 1034 Hwa. Each set of measurements used microscopy and cell segmentation to determine the length and width,
 1035 and then calculated cell size by treating the cell as a cylinder with two hemispherical ends, as we considered
 1036 in the previous section. While there is notable discrepancy between the two research groups, which are both
 1037 using strain NCM3722, Basan *et al.* found that this came specifically from uncertainty in determining the cell
 1038 width. This is prone to inaccuracy given the small cell size and optical resolution limits (further described in their
 1039 supplemental text). Perhaps the more concerning point is that while each of these alternative measurements
 1040 show an exponential increase in cell size at faster growth rates, the measurements used by Schmidt *et al.* appear
 1041 to plateau. This resulted in an analogous trend in their final reported total cellular protein per cell as shown in

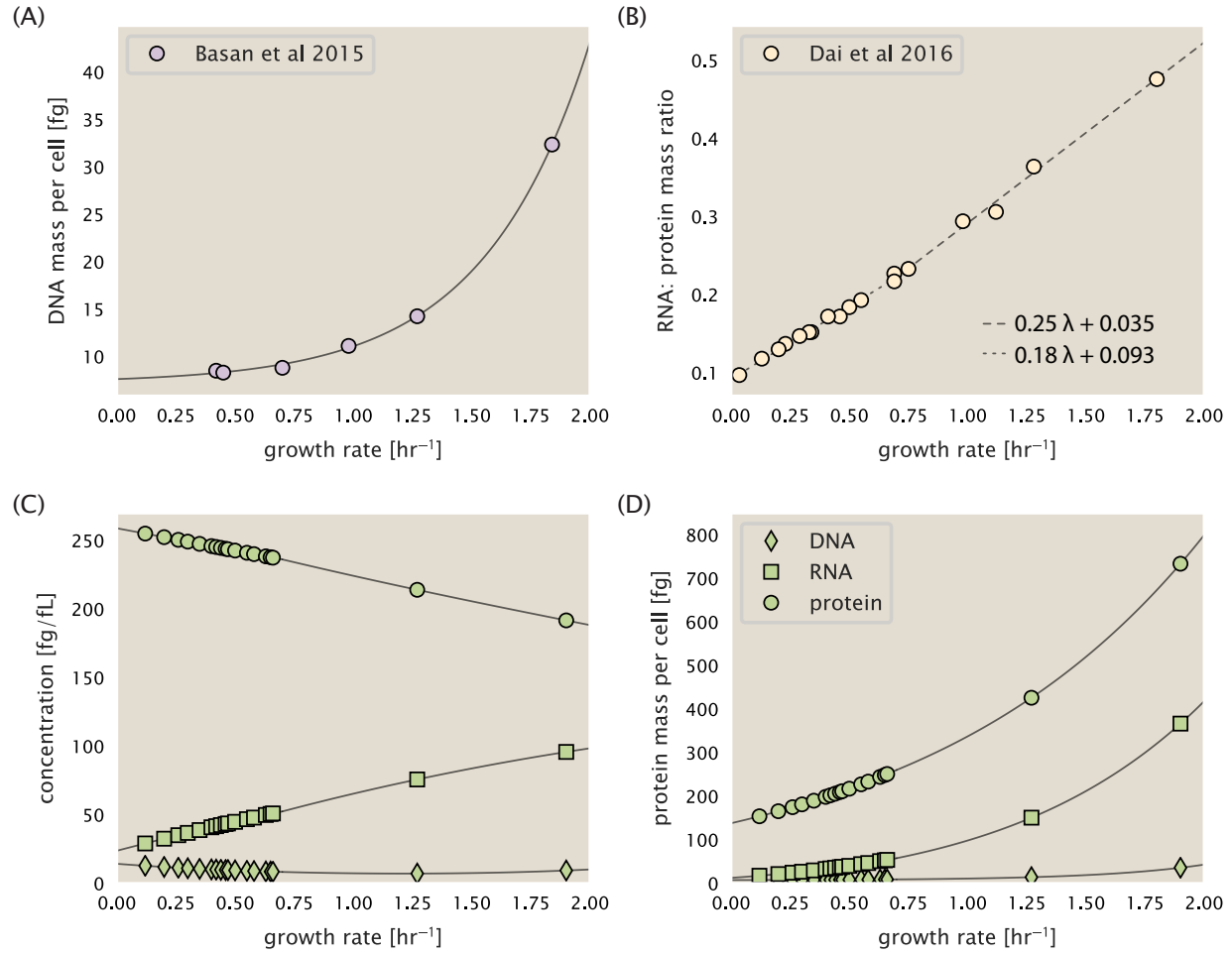


Figure 15. Empirical estimate of cellular protein, DNA, and RNA as a function of growth rate. (A) Measured DNA mass per cell as a function of growth rate, reproduced from Basan *et al.* 2015. The data was fit to an exponential curve (DNA mass in fg per cell is given by $0.42 e^{2.23 \cdot \lambda} + 7.2$ fg per cell, where λ is the growth rate in hr^{-1}). (B) RNA to protein measurements as a function of growth rate. The data was fit to two lines (shown in black) due to the change in slope at slower growth rates ?? . For growth rates below 0.7 hr^{-1} , the RNA/protein ratio is $0.18 \cdot \lambda + 0.093$, while for growth rates faster than 0.7 hr^{-1} the RNA/protein ratio is given by $0.25 \cdot \lambda + 0.035$. For (A) and (B) cells are grown under varying levels of nutrient limitation, with cells grown in minimal media with different carbon sources for the slowest growth conditions, and rich-defined media for fast growth rates. (C) Estimation of cellular protein, DNA, and RNA concentration. (D) Total cellular mass estimated for protein, DNA, and RNA using the cell size calculated in Estimation of Cell Size and Surface Area. Symbols (diamond: DNA, square: RNA, circle: protein) show estimated values of mass concentration and mass per cell for the specific growth rates ? .

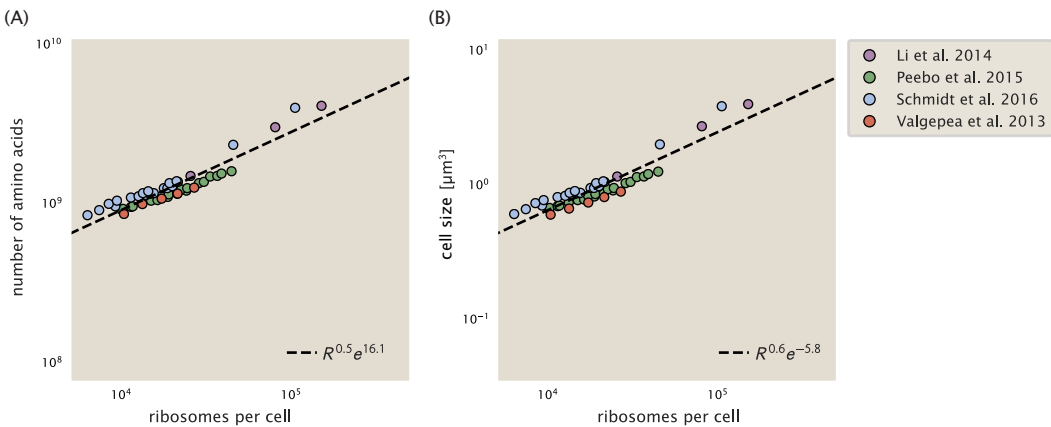


Figure 16. Phenomenological regression of cell volume and number of amino acids per cell as a function of the ribosome copy number. (A) Estimated total number of peptide bonds per cell N_{pep} as a function of number of ribosomes per cell. (B) Estimated cell size as described in Estimation of Cell Size and Surface Area, as a function of number of ribosomes per cell. Colored points correspond to the measured value (or calculated value in the case of the cell size) with colors denoting different data sets. The dashed black line shows the result of the fit, with the functional form of the equation given in the legend with R representing the ribosome copy number.

1042 **Figure 18** (purple data points), and is in disagreement with other measurements of total protein at these growth
1043 rates (?).

1044 Since it is not obvious how measurements of cell size influenced their reported protein abundances, in the
1045 following subsections we begin by considering how the authors determined total protein mass per cell. We then
1046 consider three different approaches to estimate the growth-rate dependent total protein mass and compare these
1047 estimates with those reported by ?. Those results are summarized in **Figure 17(B)**, with the original values from
1048 both ? and ? shown in **Figure 17(A)** for reference. For most growth conditions, we find reasonable agreement
1049 between our estimates and the reported total protein per cell. However, for the fastest growth conditions, with
1050 glycerol + supplemented amino acids, and LB media, all estimates are substantially higher than those originally
1051 reported. This is the main reason why we chose to readjuste protein abundance as shown in **Figure 12(B**) (with
1052 the calculation described in section Estimation of Total Protein Content per Cell).

1053 Effect of cell volume on reported absolute protein abundances

1054 As noted in Experimental Details Behind Proteomic Data, the authors from the work in ? calculated proteome-wide
1055 protein abundances by first determining absolute abundances of 41 pre-selected proteins, which relied on adding
1056 synthetic heavy reference peptides into their protein samples at known abundance. This absolute quantitation
1057 was performed in replicate for each growth condition. Separately, the authors also performed a more conven-
1058 tional mass spectrometry measurement for samples from each growth condition, which attempted to maximize
1059 the number of quantified proteins but only provided relative abundances based on peptide intensities. Finally,
1060 using their 41 proteins with absolute abundances already determined, they then created calibration curves with
1061 which to relate their relative intensity to absolute protein abundance for each growth condition. This allowed them
1062 to estimate absolute protein abundance for all proteins detected in their proteome-wide data set. Combined with
1063 their flow cytometry cell counts, they were then able to determine absolute abundance of each protein detected
1064 on a per cell basis.

1065 While this approach provided absolute abundances, another necessary step to arrive at total cellular protein
1066 was to account for any protein loss during their various protein extraction steps. Here the authors attempted
1067 to determine total protein separately using a BCA protein assay. In personal communications, it was noted that
1068 determining reasonable total protein abundances by BCA across their array of growth conditions was particularly
1069 troublesome. Instead, they noted confidence in their total protein measurements for cells grown in M9 minimal
1070 media + glucose and used this as a reference point with which to estimate the total protein for all other growth
conditions.

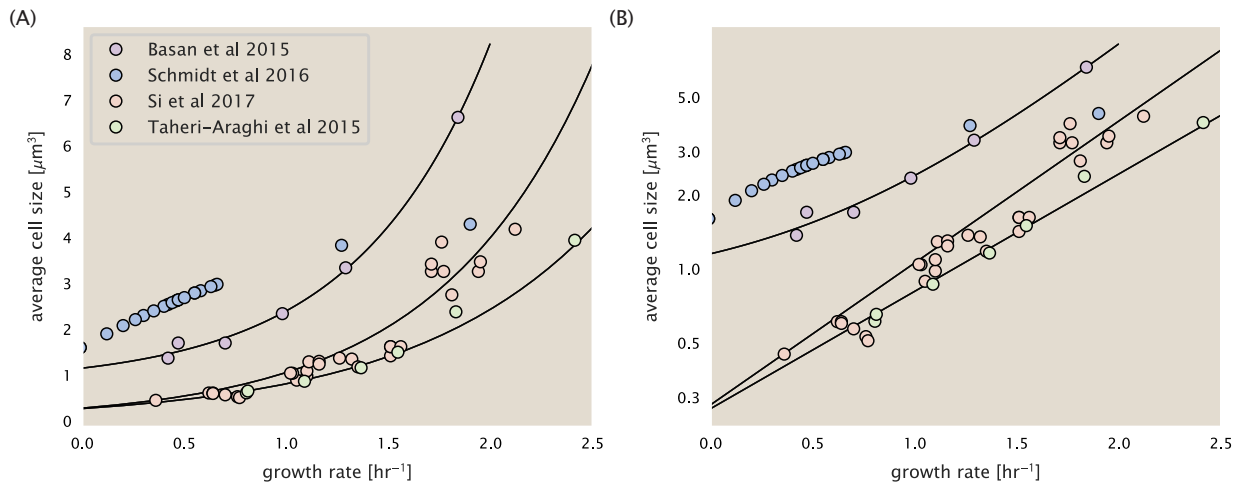


Figure 17. Measurements of cell size as a function of growth rate. (A) Plot of the reported cell sizes from several recent papers. The data in blue come from Volkmer and Heinemann, 2011 (?) and were used in the work of Schmidt *et al.*. Data from the lab of Terence Hwa are shown in purple (?), while the two data sets shown in green and light red come from the lab of Suckjoon Jun (??). (B) Same as in (A) but with the data plotted on a logarithmic y-axis to highlight the exponential scaling that is expected for *E. coli*.

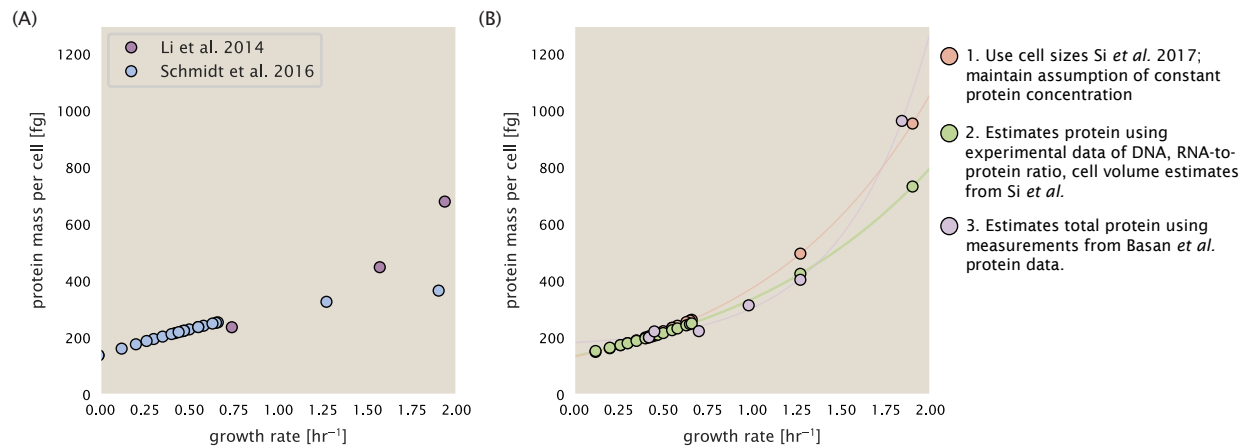


Figure 18. Alternative estimates of total cellular protein for the growth conditions considered in Schmidt *et al.* (A) The original protein mass from Schmidt *et al.* and Li *et al.* are shown in purple and blue, respectively. (B) Three alternative estimates of total protein per cell. 1. light red: Rescaling of total protein mass assuming a growth rate independent protein concentration and cell volumes estimated from Si *et al.* 2017. 2. light green: Rescaling of total protein mass using estimates of growth rate-dependent protein concentrations and cell volumes estimated from Si *et al.* 2017. Total protein per cell is calculated by assuming a 1.1 g/ml cellular mass density, 30% dry mass, with 90% of the dry mass corresponding to DNA, RNA, and protein (?). See Estimation of Total Protein Content per Cell for details on calculation. 3. light purple: Rescaling of total protein mass using the experimental measurements from Basan *et al.* 2015.

1072 For cells grown in M9 minimal media + glucose an average total mass of $M_p = 240$ fg per cell was measured.
1073 Using their reported cell volume, reported as $V_{orig} = 2.84$ fl, a cellular protein concentration of $[M_p]_{orig} = M_p/V_{orig} =$
1074 85 fg/fl. Now, taking the assumption that cellular protein concentration is relatively independent of growth rate,
1075 they could then estimate the total protein mass for all other growth conditions from,

$$M_{P,i} = [M_p]_{orig} \cdot V_i \quad (8)$$

1076 where $M_{P,i}$ represents the total protein mass per cell and V_i is the cell volume for each growth condition i as mea-
1077 sured in Volkmer and Heinemann, 2011. Here the thinking is that the values of $M_{P,i}$ reflects the total cellular protein
1078 for growth condition i , where any discrepancy from their absolute protein abundance is assumed to be due to
1079 protein loss during sample preparation. The protein abundances from their absolute abundance measurements
1080 noted above were therefore scaled to their estimates and are shown in Figure **Figure 18** (purple data points).

1081 If we instead consider the cell volumes predicted in the work of Si *et al.*, we again need to take growth in M9
1082 minimal media + glucose as a reference with known total mass, but we can follow a similar approach to estimate
1083 total protein mass for all other growth conditions. Letting $V_{Si,glu} = 0.6$ fl be the predicted cell volume, the cellular
1084 protein concentration becomes $[M_p]_{Si} = M_p/V_{Si,glu} = 400$ fg/fl. The new total protein mass per cell can then be
1085 calculated from,

$$M'_{P,i} = [M_p]_{Si} \cdot V_{Si,i} \quad (9)$$

1086 where $M'_{P,i}$ is the new protein mass prediction, and $V_{Si,i}$ refers to the new volume prediction for each condition i ,
1087 These are shown as red data points in Figure **Figure 18(B)**.

1088 Relaxing assumption of constant protein concentration across growth conditions

1089 We next relax the assumption that cellular protein concentration is constant and instead, attempt to estimate
1090 it using experimental data. Here we use the estimation of total protein mass per cell detailed in Estimation of
1091 Total Protein Content per Cell for all data points in the ? data set. The green data points in **Figure 18(B)** show this
1092 prediction, and this represents the approach used to estimate total protein per cell for all data sets.

1093 Comparison with total protein measurements from Basan *et al.* 2015.

1094 One of the challenges in our estimates in the preceding sections is the need to estimate protein concentration
1095 and cell volumes. These are inherently difficult to measure accurately due to the small size of *E. coli*. Indeed, for all
1096 the additional measurements of cell volume included in Figure **Figure 17**, no measurements were performed for
1097 cells growing at rates below 0.5 hr^{-1} . It therefore remains to be determined whether our extrapolated cell volume
1098 estimates are appropriate, with the possibility that the logarithmic scaling of cell size might break down for slower
1099 growth.

1100 In our last approach we therefore attempt to estimate total protein using experimental data that required no
1101 estimates of concentration or cell volume. Specifically, in the work of Basan *et al.*, the authors measured total
1102 protein per cell for a broad range of growth rates (reproduced in Figure **Figure 19**). These were determined by
1103 first measuring bulk protein from cell lysate, measured by the colorimetric Biuret method (?), and then abundance
1104 per cell was calculated from cell counts from either plating cells or a Coulter counter. While it is unclear why
1105 Schmidt *et al.* was unable to take a similar approach, the results from Basan *et al* appear more consistent with
1106 our expectation that cell mass will increase exponentially with faster growth rates. In addition, although they do
1107 not consider growth rates below about 0.5 hr^{-1} , it is interesting to note that the protein mass per cell appears to
1108 plateau to a minimum value at slow growth. In contrast, our estimates using cell volume so far have predicted
1109 that total protein mass should continue to decrease slightly for slower growing cells. By fitting this data to an
1110 exponential function dependent on growth rate, we could then estimate the total protein per cell for each growth
1111 condition considered by ?. These are plotted as red data points in **Figure 18(B)**.

1112 Calculation of Complex Abundance

1113 All protein data quantified the abundance of individual proteins per cell. However, this work requires estimates
1114 on the abundance of individual protein complexes, rather than the copy number of individual proteins. In our

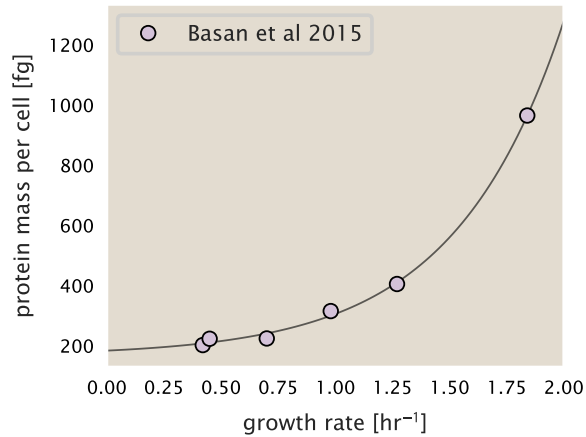


Figure 19. Total cellular protein reported in Basan et al. 2015. Measured protein mass as a function of growth rate as reproduced from Basan et al. 2015, with cells grown under different levels of nutrient limitation. The data was fit to an exponential curve where protein mass in fg per cell is given by $14.65 e^{2.180 \cdot \lambda} + 172$ fg per cell, where λ is the growth rate in hr^{-1}).

analysis of the protein copy number data, it became clear that the reported copy numbers do not always align with those based on reported stoichiometry. As one example of this, the F-O subunit of ATP synthase consists of three protein subunits with a stoichiometry of $[\text{AtpB}][\text{AtpF}]_2[\text{AtpE}]_{10}$ (also referred to as subunits a, b, and c, respectively). In the experimental data of ?, the values deviate from this quite substantially, with approximately 1000 AtpB, 9000 AtpF, and 300 AtpE reported per cell (minimal media + glucose growth condition). This highlights the technical challenges that still remain in our ability to quantify cellular composition, particularly for membrane-bound proteins like the ATP synthase complex considered here. In this section, we outline the approach we used to annotate proteins as part of each macromolecular complex and how we used averaging across the individual protein measurements to estimate an absolute complex abundances per cell.

Protein complexes, and proteins individually, often have a variety of names, both longform and shorthand. As individual proteins can have a variety of different synonyms, we sought to ensure that each protein annotated in the data sets used the same synonym. To do use, we relied heavily on the EcoCyc Genomic Database (?). Each protein in available data sets included an annotation of one of the gene name synonyms as well as an accession ID – either a UniProt or Blattner "b-number". We programmatically matched up individual accession IDs between the proteins in different data sets. In cases where accession IDs matched but the gene names were different, we manually verified that the gene product was the same between the datasets and chose a single synonym. All code used in the data cleaning and unification procedures can be found on the associated [GitHub repository](#) (DOI:XXX) associated with this paper as well as on the associated [paper website](#).

With each protein conforming to a single identification scheme, we then needed to identify the molecular complexes each protein was a member of. Additionally, we needed to identify how many copies of each protein were present in each complex (i.e. the subunit copy number) and compute the estimated abundance complex that accounted for fluctuations in subunit stoichiometry. To map proteins to complexes, we accessed the EcoCyc *E. coli* database ? using PathwayTools version 23.0 ?. With a license for PathWay Tools, we mapped each unique protein to its annotated complexes via the BioCyc Python package. As we mapped each protein with *all* of its complex annotations, there was redundancy in the dataset. For example, ribosomal protein L20 (RplT) is annotated to be a component of the 50S ribosome (EcoCyc complex CPLX-03962) as well as a component of the mature 70S ribosome (EcoCyc complex CPLX-03964).

In addition to the annotated complex, we collected information on the stoichiometry of each macromolecular complex. For a complex with N_{subunits} protein species, for each protein subunit i we first calculate the number of complexes that *could* be formed given the measured protein copy numbers per cell,

$$N_{\text{complex}}(\text{subunit } i) = \frac{P_{\text{subunit } i}^{(\text{measured})}}{m_{\text{subunit } i}}. \quad (10)$$

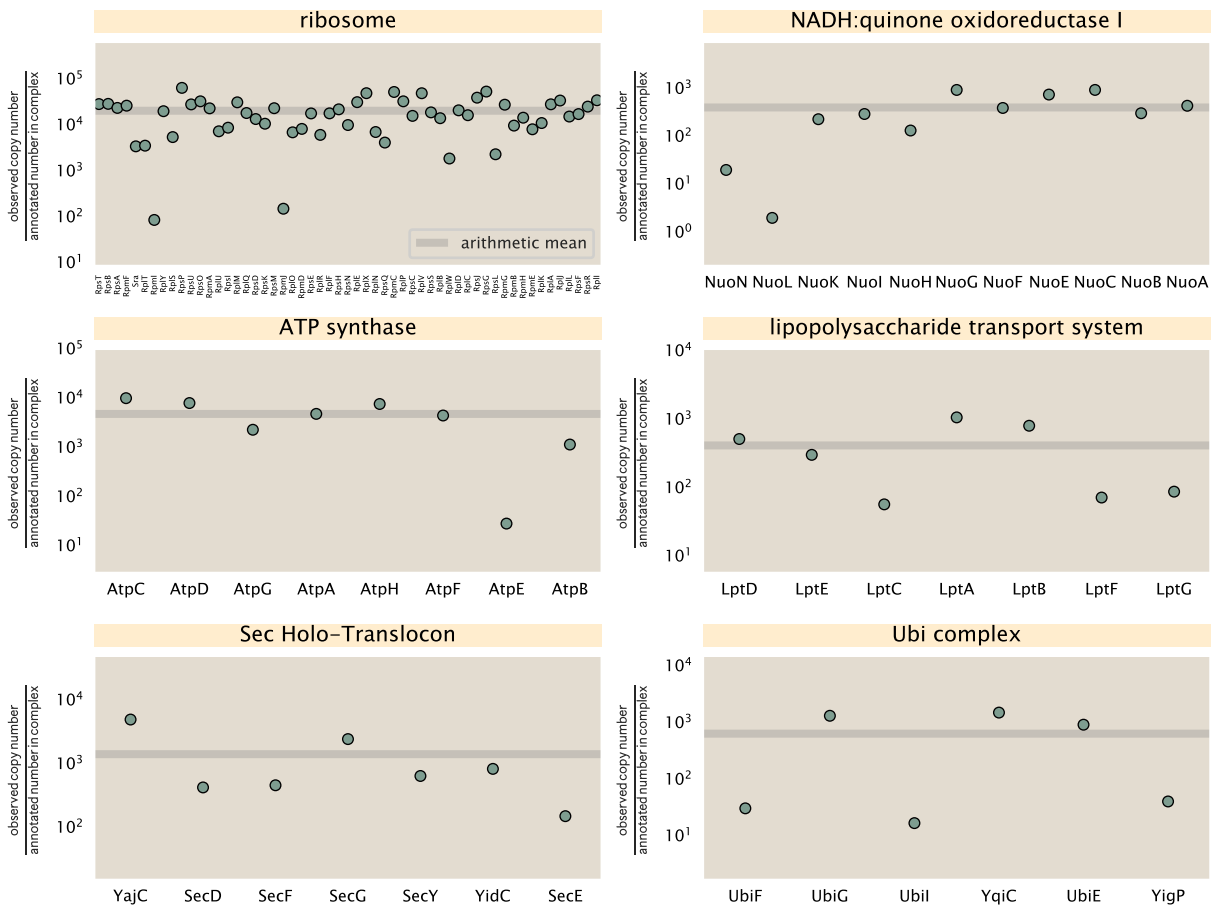


Figure 20. Calculation of the mean complex abundance from measurements of single subunits. Six of the largest complexes (by number of subunits) in *E. coli*. Points correspond to the maximum number of complexes that can be formed given measurement of that individual protein. Solid grey line corresponds to the arithmetic mean across all subunits. These data correspond to measurements from ? in a glucose-supplemented minimal growth medium.

1145 Here, $P_{\text{subunit } i}^{(\text{measured})}$ refers to the measured protein copy number of species i , and m refers to the number of monomers
 1146 present for that protein in the complex. For example, the 70S mature ribosome complex has 55 protein compo-
 1147 nents, all of which are present in a single copy except L4 (RplL), which is present in 4 copies ($m = 4$). For each
 1148 ribosomal protein, we then calculate the maximum number of complexes that could be formed using **Equation 10**.
 1149 This example, along with example from 5 other macromolecular complexes, can be seen in **Figure 20**.
 1150 It is important to note that measurement noise, efficiency of protein extraction, and differences in protein
 1151 stability will mean that the precise value of each calculation will be different for each component of a given complex.
 1152 Thus, to report the total complex abundance, we use the arithmetic mean of across all subunits in the complex,

$$\langle N_{\text{complex}} \rangle = \frac{1}{N_{\text{subunits}}} \sum_i^{N_{\text{subunits}}} \frac{P_i^{(\text{measured})}}{m_{\text{subunit } i}}. \quad (11)$$

1153 in **Figure 20**, we show this mean value as a grey line for a variety of different complexes. Additionally, we have
 1154 built an interactive figure accessible on the [paper website](#) where the validity of this approach can be examined
 1155 for any complex with more than two subunits (thus, excluding monomers and dimers).

1156 Extending Estimates to a Continuum of Growth Rates

1157 In the main text, we considered a standard stopwatch of 5000 s to estimate the abundance of the various protein
 1158 complexes considered. In addition to point estimates, we also showed the estimate as a function of growth rate

1159 as transparent grey curves. In this section, we elaborate on this continuum estimate, giving examples of estimates
1160 that scale with either cell volume, cell surface area, or number of origins of replication.

1161 Estimation of the total cell mass

1162 For many of the processes estimated in the main text we relied on a cellular dry mass of ≈ 300 fg from which we
1163 computed elemental and protein fractions using knowledge of fractional composition of the dry mass. At modest
1164 growth rates, such as the 5000 s doubling time used in the main text, this is a reasonable number to use as the
1165 typical cell mass is ≈ 1 pg and *E. coli* cells can approximated as 70% water by volume. However, as we have shown
1166 in the preceding sections, the cell size is highly dependent on the growth rate. This means that a dry mass of 300
1167 fg cannot be used reliably across all growth rates.

1168 Rather, using the phenomenological description of cell volume scaling exponentially with growth rate, and
1169 using a rule-of-thumb of a cell buoyant density of ≈ 1.1 pg / fL (BNID: 103875), we can calculate the cell dry mass
1170 across a range of physiological growth rates as

$$m_{\text{cell}} \approx \rho V(\lambda) \approx \rho a e^{\lambda * b} \quad (12)$$

1171 where a and b are constants with units of μm^3 and hr, respectively. The value of these constants can be estimated
1172 from the careful volume measurements performed by ??, as considered in Appendix Estimation of Cell Size and
1173 Surface Area earlier.

1174 Complex Abundance Scaling With Cell Volume

1175 Several of the estimates performed in the main text are implicitly dependent on the cell volume. This includes
1176 processes such as ATP utilization and, most prominently, the transport of nutrients, whose demand will be pro-
1177 portional to the volume of the cell. Of the latter, we estimated the number of transporters that would be needed
1178 to shuttle enough carbon, phosphorus, and sulfur across the membrane to build new cell mass. To do so, we
1179 used elemental composition measurements combined with a 300 fg cell dry mass to make the point estimate. As
1180 we now have a means to estimate the total cell mass as a function of volume, we can generalize these estimates
1181 across growth rates.

1182 Rather than discussing the particular details of each transport system, we will derive this scaling expression in
1183 very general terms. Consider that we wish to estimate the number of transporters for some substance X , which
1184 has been measured to be made up some fraction of the dry mass, θ_X . If we assume that, irrespective of growth
1185 rate, the cell dry mass is relatively constant (?) and $\approx 30\%$ of the total cell mass, we can state that the total mass
1186 of substance X as a function of growth rate is

$$m_X \approx 0.3 \times \rho V(\lambda) \theta_X, \quad (13)$$

1187 where we have used $\rho V(\lambda)$ as an estimate of the total cell mass, defined in *Equation 12*. To convert this to the
1188 number of units N_X of substance X in the cell, we can use the formula weight w_X of a single unit of X in conjunction
1189 with *Equation 13*,

$$N_X \approx \frac{m_X}{w_X}. \quad (14)$$

1190 To estimate the number of transporters needed, we make the approximation that loss of units of X via diffusion
1191 through porins or due to the permeability of the membrane is negligible and that a single transporter complex
1192 can transport substance X at a rate r_X . As this rate r_X is in units of X per time per transporter, we must provide
1193 a time window over which the transport process can occur. This is related to the cell doubling time τ , which can
1194 be calculated from the the growth rate λ as $\tau = \log(2)/\lambda$. Putting everything together, we arrive at a generalized
1195 transport scaling relation of

$$N_{\text{transporters}}(\lambda) = \frac{0.3 \times \rho V(\lambda) \theta_X}{w_X r_X \tau}. \quad (15)$$

1196 This function is used to draw the continuum estimates for the number of transporters seen in Figures 2 and
1197 3 as transparent grey curves. Occasionally, this continuum scaling relationship will not precisely agree with the
1198 point estimate outlined in the main text. This is due to the choice of ≈ 300 fg total dry mass per cell for the point
1199 estimate, whereas we considered more precise values of cell mass in the continuum estimate. We note, however,

1200 that both this scaling relation and the point estimates are meant to describe the order-of-magnitude observed,
1201 and not the predict the exact values of the abundances.

1202 **Equation 15** is a very general relation for processes where the cell volume is the "natural variable" of the
1203 problem. This means that, as the cell increases in volume, the requirements for substance X also scale with
1204 volume rather than scaling with surface area, for example. So long as the rate of the process, the fraction of the
1205 dry mass attributable to the substance, and the formula mass of the substance is known, **Equation 15** can be used
1206 to compute the number of complexes needed. For example, to compute the number of ATP synthases per cell,
1207 **Equation 15** can be slightly modified to the form

$$N_{\text{ATP synthases}}(\lambda) = \frac{0.3 \times \rho V(\lambda) \theta_{\text{protein}} N_{\text{ATP}}}{w_{AA} r_{\text{ATP}} \tau}, \quad (16)$$

1208 where we have included the term N_{ATP} to account for the number of ATP equivalents needed per amino acid for
1209 translation (≈ 4 , BNID: 114971), and w_{AA} is the average mass of an amino acid. The grey curves in Figure 4 of the
1210 main text were made using this type of expression.

1211 **A Relation for Complex Abundance Scaling With Surface Area**

1212 In our estimation for the number of complexes needed for lipid synthesis and peptidoglycan maturation, we used
1213 a particular estimate for the cell surface area ($\approx 5 \mu\text{m}$, BNID: 101792) and the fraction of dry mass attributable to
1214 peptidoglycan ($\approx 3\%$, BNID: 101936). Both of these values come from glucose-fed *E. coli* in balanced growth. As we
1215 are interested in describing the scaling as a function of the growth rate, we must also consider how these values
1216 scale with cell surface area, which is the natural variable for these types of processes. In the coming paragraphs,
1217 we highlight how we incorporate a condition-dependent surface area into our calculation of the number of lipids
1218 and murein monomers that need to be synthesized and crosslinked, respectively.

1219 Number of Lipids

1220 To compute the number of lipids as a function of growth rate, we make the assumption that some features, such as
1221 the surface area of a single lipid ($A_{\text{lipid}} \approx 0.5 \text{ nm}^2$, BNID: 106993) and the total fraction of the membrane composed
1222 of lipids ($\approx 40\%$, BNID: 100078) are independent of the growth rate. Using these approximations combined with
1223 **Equation 6**, and recognizing that each membrane is composed of two leaflets, we can compute the number of
1224 lipids as a function of growth rate as

$$N_{\text{lipids}}(\lambda) \approx \frac{4 \text{ leaflets} \times 0.4 \times \eta \pi \left(\frac{\eta \pi}{4} - \frac{\pi}{12} \right)^{-2/3} V(\lambda)^{2/3}}{A_{\text{lipid}}} \quad (17)$$

1225 where η is the length-to-width aspect ratio and V is the cell volume.

1226 Number of Murein Monomers

1227 In calculation of the number of transpeptidases needed for maturation of the peptidoglycan, we used an empirical
1228 measurement that $\approx 3\%$ of the dry mass is attributable to peptidoglycan and that a single murien monomer is
1229 $m_{\text{murein}} \approx 1000 \text{ Da}$. While the latter is independent of growth rate, the former is not. As the peptidoglycan exists as
1230 a thin shell with a width of $w \approx 10 \text{ nm}$ encapsulating the cell, one would expect the number of murein monomers
1231 scales with the surface area of this shell. In a similar spirit to our calculation of the number of lipids, the total
1232 number of murein monomers as a function of growth rate can be calculated as

$$N_{\text{murein monomers}}(\lambda) \approx \frac{\rho_{\text{pg}} w \eta \pi \left(\frac{\eta \pi}{4} - \frac{\pi}{12} \right)^{-2/3} V(\lambda)^{2/3}}{m_{\text{murein}}}, \quad (18)$$

1233 where ρ_{pg} is the density of peptidoglycan.

1234 **Complex Abundance Scaling With Number of Origins, and rRNA Synthesis**

1235 While the majority of our estimates hinge on the total cell volume or surface area, processes related to the central
1236 dogma, namely DNA replication and synthesis of rRNA, depend on the number of chromosomes present in the
1237 cell. As discussed in the main text, the ability of *E. coli* to parallelize the replication of its chromosome by having

multiple active origins of replication is critical to synthesize enough rRNA, especially at fast growth rates. Derived in ? and reproduced in the main text and Appendix Estimation of $\langle \#ori \rangle$ / $\langle \#ter \rangle$ and $\langle \#ori \rangle$ below, the average number of origins of replication at a given growth rate can be calculated as

$$\langle \#ori \rangle \approx 2^{t_{cyc} \lambda / \ln 2} \quad (19)$$

where t_{cyc} is the total time of replication and division. We can make the approximation that $t_{cyc} \approx 70$ min, which is the time from the initiation of chromosomal replication until division. This time corresponds to the sum of the so-called C and D periods of the cell cycle, which correspond to the time it takes to replicate the entire chromosome (C period) and the time from completion to eventual division (D period) ?.

In the case of rRNA synthesis, the majority of the rRNA operons are surrounding the origin of replication. Thus, at a given growth rate λ , the average dosage of rRNA operons per cell D_{rRNA} is

$$D_{rRNA}(\lambda) \approx N_{rRNA \text{ operons}} \times 2^{t_{cyc} \lambda / \ln 2}. \quad (20)$$

This makes the approximation that *all* rRNA operons are localized around the origin. In reality, the operons are some distance away from the origin, making **Equation 20** an approximation (?).

In the main text, we stated that at a growth rate of 0.5 hr^{-1} , there is ≈ 1 chromosome per cell. While a fair approximation, **Equation 19** illustrates that is not precisely true, even at slow growth rates. In estimating the number of RNA polymerases as a function of growth rate, we consider that regardless of the number of rRNA operons, they are all sufficiently loaded with RNA polymerase such that each operon produces one rRNA per second. Thus, the total number of RNA polymerase as a function of the growth rate can be calculated as

$$N_{\text{RNA polymerase}}(\lambda) \approx L_{\text{operon}} D_{rRNA} \rho_{\text{RNA polymerase}}, \quad (21)$$

where L_{operon} is the total length of an rRNA operon (≈ 4500 bp) and $\rho_{\text{RNA polymerase}}$ is packing density of RNA polymerase on a given operon, taken to be 1 RNA polymerase per 80 nucleotides.

Calculation of active ribosomal fraction.

In the main text we used the active ribosomal fraction f_a that was reported in the work of ? to estimate the active ribosomal mass fraction $\Phi_R \times f_a$ across growth conditions. We lacked any specific model to consider how f_a should vary with growth rate, and instead find that the data is well-approximated by fitting to an exponential curve ($f_a = -0.889 e^{4.6 \cdot \lambda} + 0.922$; dashed line in inset of **Figure 9(C)**). We use this function to estimate f_a for each of the data points shown in **Figure 9(C)**.

Estimation of $\langle \#ori \rangle$ / $\langle \#ter \rangle$ and $\langle \#ori \rangle$.

E. coli shows robust scaling of cell size with the average number of origins per cell, $\langle \#ori \rangle$ (?). Since protein makes up a majority of the cell's dry mass, the change in cell size is also a reflection of the changes in proteomic composition and total abundance across growth conditions. Given the potential constraints on rRNA synthesis and changes in ribosomal copy number with $\langle \#ori \rangle$, it becomes important to also consider how protein copy numbers vary with the state of chromosomal replication. This is particularly true when trying to make sense of the changes in ribosomal fraction and growth-rate dependent changes in proteomic composition at a mechanistic level. As considered in the main text, it is becoming increasingly apparent that regulation through the secondary messengers (p)ppGpp may act to limit DNA replication and also reduce ribosomal activity in poorer nutrient conditions. In this context, both $\langle \#ori \rangle$, as well as the $\langle \#ori \rangle$ / $\langle \#ter \rangle$ ratio become important parameters to consider and keep track of. An increase in $\langle \#ori \rangle$ / $\langle \#ter \rangle$ ratio in particular, causes a relatively higher gene dosage in rRNA and r-protein genes due to skew in genes near the origin, where the majority of these are located

In the main text we estimated the change in $\langle \#ori \rangle$ with growth rate using the nutrient-limited wild-type cell data from ?. We consider their measurements of DNA replication time (t_C , 'C' period of cell division), total cell cycle time (t_{cyc} , 'C' + 'D' period of cell division), and doubling time τ from wild-type *E. coli* growing across a range of growth conditions. Here we show how we estimate this parameter, as well as the $\langle \#ori \rangle$ / $\langle \#ter \rangle$ ratio from their data. We begin by considering $\langle \#ori \rangle$. If the cell cycle time takes longer than the time of cell division, the cell will need to initiate DNA replication more often than its rate of division, $2^{\lambda t} = 2^{\ln(2) \cdot t / \tau}$ to maintain steady state growth. Cells will

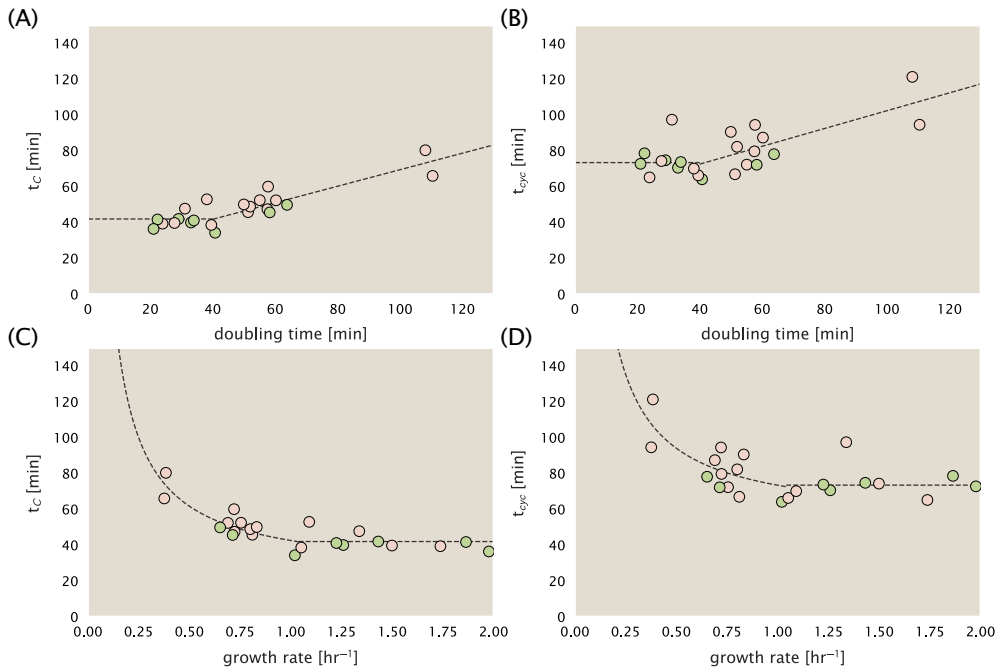


Figure 21. Estimation of $\langle \#ori \rangle / \langle \# ter \rangle$ and $\langle \#ori \rangle$ using data from Si et al. (2017). (A) and (B) plot the reported t_C and t_{cyc} as a function of cell doubling time τ , respectively. The dashed lines show a piecewise fit to the data. For short doubling times (rich media), t_C and t_{cyc} are assumed constant ($t_C = 42$ minutes, $t_{cyc} = 73$ minutes). At the transition, taken to occur at 40 minutes, the dashed line corresponds to an assumed proportional increase in each parameter as a function of the doubling time ($t_C = 0.46\tau + 23.3$ minutes, $t_{cyc} = 0.50\tau + 52.7$ minutes). (C) and (D) plot the same data as in (A) and (B), but as a function of growth rate, given by $\lambda = \ln(2)/\tau$.

need to do this in proportion to the ratio $\lambda_{cyc}/\lambda = t_{cyc}/\tau$, and the number of origins per cell (on average) is then given by $2^{t_{cyc}/\tau}$. The average number of termini will in contrast depend on the lag time between DNA replication and cell division, t_D , with $\langle \#ori \rangle / \langle \# ter \rangle$ ratio $= 2^{t_{cyc}/\tau - t_D/\tau} = 2^{t_C/\tau}$.

In Figure 21(A) and (B) we plot the measured t_C and t_{cyc} values versus the doubling time from ?. The authors estimated t_C by marker frequency analysis using qPCR, while $t_{cyc} = t_C + t_D$ were inferred from t_C and τ . In the plots we see that both t_C and t_{cyc} reach a minimum at around 40 and 75 minutes, respectively. For a C period of 40 minutes, this would correspond to a maximum rate of elongation of about 1,000 bp/sec. Since we lacked a specific model to describe how each of these parameters vary with growth condition, we assumed that they were linearly dependent on the doubling time. For each parameter, t_C and t_{cyc} , we split them up into two domains corresponding to poorer nutrient conditions and rich nutrient conditions (cut off at $\tau \approx 40$ minutes where chromosomal replication becomes nearly constant). The fit lines are shown as solid black lines. In Figure 21(C) and (D) we also show t_C and t_{cyc} as a function of growth rate λ along with our piecewise linear fits, which match the plots in the main text.

Derivation of Minimal Model for Nutrient-Mediated Growth Rate Control

Here we provide a derivation of the minimal model for growth rate control under nutrient-limited growth. By growth rate control, we are specifically referring to the ability of bacteria to modulate their proteome (N_{pep} , R , Φ_R) and cell size as nutrient conditions change, with slower growing cells generally being smaller in size (?). This capability provides bacteria with a particular benefit when nutrients are more scarce since it will mean there is a smaller net demand on carbon, phosphorus, sulfur, and nitrogen. The specific goal of developing this model is to help us better explore the overall constraints on growth that follow from 1) our observation that many of the cellular processes we've considered require increased protein abundance at faster growth rates, and 2) a strict limit on growth rate that is governed by the ribosomal synthesis rate and ribosomal mass fraction Φ_R .

In Figure 11(A) of the main text we provide a schematic of the model, where we consider growth as simply

1303 governed by the rate of protein synthesis ($r_t \times R \times f_a$). In order to grow rapidly, at least to the extent possible,
 1304 these three parameters need to be maximized (with $r_t \leq 17$ amino acids per second, and $f_a \leq 1$ reported in the
 1305 work of ?). The elongation rate r_t will depend on how quickly ribosomes can match codons with their correct
 1306 amino-acyl tRNA, along with the subsequent steps of peptide bond formation and translocation. This ultimately
 1307 depends on the cellular concentration amino acids, which we treat as a single effective species, $[AA]_{\text{eff}}$.

1308 In our model, we need to determine the rate of peptide elongation r_t , which we consider as simply depending
 1309 on the supply of amino acids (and, therefore, also amino-acyl tRNAs) through a parameter r_{AA} in units of AA per
 1310 second, and the rate of amino acid consumption by protein synthesis ($r_t \times R \times f_a$). The balance between these
 1311 two rates will determine the effective amino acid concentration in the cell $[AA]_{\text{eff}}$. An important premise for this
 1312 formulation is growing evidence that cells are able to modulate their biosynthesis activity according to nutrient
 1313 availability (i.e. extent of chromosomal replication, transcriptional, and translation activity) through secondary-
 1314 messenger molecules like (p)ppGpp (?????). Given our observation that protein synthesis and energy production
 1315 are not limiting, we assume that other molecular players required by ribosomes like elongation factors and GTP
 1316 are available in sufficient abundance. In addition, experimentally, the relative number of tRNA and elongation
 1317 factor EF-Tu per ribosome have been found to increase in poorer nutrient conditions ???).

1318 We begin by considering a coarse-grained description of peptide elongation, which includes 1) the time re-
 1319 quired to find and bind each correct amino-acyl tRNA, and 2) the remaining steps in peptide elongation that will
 1320 not depend on the amino acid availability. These time scales will be related to the inverse of the elongation rate

1321 r_t ,

$$\frac{1}{r_t} = \frac{1}{k_{on}\alpha[AA]_{\text{eff}}} + \frac{1}{r_t^{\max}}. \quad (22)$$

1322 where we have assumed that the rate of binding by amino-acyl tRNA k_{on} is proportional to $[AA]_{\text{eff}}$ by a constant
 1323 α . r_t^{\max} refers to the maximum elongation rate. This leads to a Michaelis-Menten dependence of the elongation
 1324 rate r_t on the effective amino acid concentration $[AA]_{\text{eff}}$ (??). We can re-write this more succinctly in terms of an
 1325 effective dissociation constant,

$$K_D = \frac{r_t^{\max}}{\alpha k_{on}}, \quad (23)$$

1326 where the elongation rate r_t is now given by

$$r_t = \frac{r_t^{\max}}{1 + K_D/[AA]_{\text{eff}}}. \quad (24)$$

1327 The rate of amino acid supply r_{AA} will vary with changing nutrient conditions and the cell can maintain $[AA]_{\text{eff}}$
 1328 by tuning the rate of amino acid consumption, $r_t \times R \times f_a$. Thus, $[AA]_{\text{eff}}$ is determined by the difference in the
 1329 rate of amino acid synthesis (or import, for rich media) and/or tRNA charging, r_{AA} , and the rate of consumption,
 1330 $r_t \times R \times f_a$. Over an arbitrary length of time t of cellular growth, the cell will grow in volume, requiring us to consider
 1331 these rates in terms of concentration rather than absolute numbers, with $[AA]_{\text{eff}}$ given by,

$$\int_0^t \frac{d[AA]_{\text{eff}}}{dt} dt = \int_0^t ([r_{AA}] - [r_t \times R \times f_a]) dt. \quad (25)$$

1332 This considers the net change in amino acid concentration over a time from 0 to t , with the square brackets
 1333 indicating concentrations per unit time. Integrating **Equation 25** yields.

$$[AA]_{\text{eff}} = t([r_{AA}] - [r_t \times R \times f_a]). \quad (26)$$

1334 Alternatively, to connect to the experimental data in terms of absolute ribosome copy number R we can con-
 1335 sider a unit volume V ,

$$[AA]_{\text{eff}} = \frac{t(r_{AA} - r_t \times R \times f_a)}{V \times N_A}, \quad (27)$$

1336 where r_{AA} is in units of AA per unit time and r_t is in units of AA per unit time per ribosome. N_A refers to Avogadro's
 1337 number and is needed to convert between concentration and absolute numbers per cell. With an expression for

1338 $[AA]_{\text{eff}}$ in hand, we can now solve **Equation 24** for r_t , which is a quadratic function with a physically-meaningful
1339 root of

$$r_t = \frac{t(r_{AA} + r_t^{(\max)} R f_a) + K_D V N_A - \sqrt{(r_{AA} t + r_t^{(\max)} R f_a t + K_D V N_A)^2 - 4(R f_a t)(r_t^{(\max)} r_{AA} t)}}{2R f_a t}. \quad (28)$$

1340 This is the key equation that allows us to calculate growth rate for any combination of N_{pep} , R , f_a , and cell size V
1341 as a function of amino acid supply r_{AA} (**Equation 3** of the main text). We refer the reader to A Minimal Model of
1342 Nutrient-Mediated Growth Rate Control of the main text for our exploration of this model in the context of the
1343 proteomic data.

1344 We end this section by noting several distinctions of this formulation with previous work. The first, as noted
1345 in the main text, relates to the now seminal work of ?, which provides a treatment of resource allocation that
1346 partitions of the proteome into sectors – including one for ribosome-associated proteins and one for metabolic
1347 proteins. As cells grow faster, there is a notable change in the mass fraction of these sectors, with an increase
1348 in ribosomal content that is predominantly achieved at the expense of a decrease in the metabolic sector. By
1349 including an additional constraint through the phenomenological parameter v , which characterizes the quality of
1350 the growth medium ???, the authors derive a model of growth rate, dependent on optimal resource allocation.
1351 Here we have developed a model that considers the effect of changes in absolute protein abundance and ribo-
1352 somal content, and consider how these influence the achievable growth rate. In addition, by accounting for the
1353 metabolic supply of amino acids directly though their availability in the cell (i.e. $[AA]_{\text{eff}}$), we are able to consider
1354 how the balance between translation-specific metabolic capacity and translational capacity influences both the
1355 elongation rate r_t and growth rate λ .

1356 The second and last point we note is that the recent works from ? and ? also employ a similar coarse-graining of
1357 translation elongation as we've considered above. Here, however, a notable distinction is that the authors consider
1358 the entire ternary complex (i.e. the complex of amino-acyl tRNA, EF-Tu, and GTP) as rate limiting. Further, through
1359 an assumed proportionality between ternary complex and ribosome abundance, they arrive at a formulation of
1360 elongation rate r_t that exhibits a Michaelis-Menten dependence on the ribosomal fraction Φ_R . They demonstrate
1361 that all their measurements of elongation rate, even upon addition of sublethal doses of chloramphenicol (which
1362 cause an increase in both r_t and Φ_R), can be collapsed onto a single curve described by this Michaelis-Menten
1363 dependence. There is always a benefit to increase their ribosomal fraction Φ_R on growth rate when nutrient
1364 conditions allow (see Maximum Growth Rate is Determined by the Ribosomal Mass Fraction), and this trend in
1365 the data in part follows from the tendency for cells to increase Φ_R and better maximize r_t as nutrient conditions
1366 improve. In addition, it does not account for the decrease in the fraction of actively translating ribosome f_a that
1367 was strikingly apparent at slow growth rates or in sublethal doses of chloramphenicol in the work of ?. Through
1368 **Equation 28** we also account for changes in the fraction of actively translating ribosomes. Ultimately, we find that
1369 cells are able to maximize both Φ_R , r_t , and their growth rate only to the extent allowed by the nutrient conditions
1370 (i.e. via r_{AA}) and through the maintenance of the cellular pool of amino acids $[AA]_{\text{eff}}$, amino-acyl tRNA, GTP, as well
1371 as the synthesis of other key molecular constituents like EF-Tu.

1372 **References**

- 1373 Abelson, H., Johnson, L., Penman, S., and Green, H. (1974). Changes in RNA in relation to growth of the fibroblast: II. The lifetime
1374 of mRNA, rRNA, and tRNA in resting and growing cells. *Cell*, 1(4):161–165.
- 1375 Aidelberg, G., Towbin, B. D., Rothschild, D., Dekel, E., Bren, A., and Alon, U. (2014). Hierarchy of non-glucose sugars in *Escherichia*
1376 *coli*. *BMC Systems Biology*, 8(1):133.
- 1377 Antonenko, Y. N., Pohl, P., and Denisov, G. A. (1997). Permeation of ammonia across bilayer lipid membranes studied by ammo-
1378 nium ion selective microelectrodes. *Biophysical Journal*, 72(5):2187–2195.
- 1379 Ashburner, M., Ball, C. A., Blake, J. A., Botstein, D., Butler, H., Cherry, J. M., Davis, A. P., Dolinski, K., Dwight, S. S., Eppig, J. T., Harris,
1380 M. A., Hill, D. P., Issel-Tarver, L., Kasarskis, A., Lewis, S., Matese, J. C., Richardson, J. E., Ringwald, M., Rubin, G. M., and Sherlock,
1381 G. (2000). Gene Ontology: tool for the unification of biology. *Nature Genetics*, 25(1):25–29.
- 1382 Ason, B., Bertram, J. G., Hingorani, M. M., Beechem, J. M., O'Donnell, M., Goodman, M. F., and Bloom, L. B. (2000). A Model
1383 for *Escherichia coli* DNA Polymerase III Holoenzyme Assembly at Primer/Template Ends: DNA Triggers A Change In Binding
1384 Specificity of the γ Complex Clamp Loader. *Journal of Biological Chemistry*, 275(4):3006–3015.
- 1385 Assentoft, M., Kaptan, S., Schneider, H.-P., Deitmer, J. W., de Groot, B. L., and MacAulay, N. (2016). Aquaporin 4 as a NH_3 Channel.
1386 *Journal of Biological Chemistry*, 291(36):19184–19195.
- 1387 Baba, T., Ara, T., Hasegawa, M., Takai, Y., Okumura, Y., Baba, M., Datsenko, K. A., Tomita, M., Wanner, B. L., and Mori, H. (2006).
1388 Construction of *Escherichia coli*K-12 in-frame, single-gene knockout mutants: the Keio collection. *Molecular Systems Biology*,
1389 2(1):2460.
- 1390 Basan, M., Zhu, M., Dai, X., Warren, M., Sévin, D., Wang, Y.-P., and Hwa, T. (2015). Inflating bacterial cells by increased protein
1391 synthesis. *Molecular Systems Biology*, 11(10):836.
- 1392 Bauer, S. and Ziv, E. (1976). Dense growth of aerobic bacteria in a bench-scale fermentor. *Biotechnology and Bioengineering*,
1393 18(1):81–94. _eprint: <https://onlinelibrary.wiley.com/doi/pdf/10.1002/bit.260180107>.
- 1394 Belliveau, N. M., Barnes, S. L., Ireland, W. T., Jones, D. L., Sweredoski, M. J., Moradian, A., Hess, S., Kinney, J. B., and Phillips, R.
1395 (2018). Systematic approach for dissecting the molecular mechanisms of transcriptional regulation in bacteria. *Proceedings
1396 of the National Academy of Sciences*, 115(21):E4796–E4805.
- 1397 Booth, I. R., Mitchell, W. J., and Hamilton, W. A. (1979). Quantitative analysis of proton-linked transport systems. The lactose
1398 permease of *Escherichia coli*. *Biochemical Journal*, 182(3):687–696.
- 1399 Bremer, H. and Dennis, P. P. (2008). Modulation of Chemical Composition and Other Parameters of the Cell at Different Expon-
1400 ential Growth Rates. *EcoSal Plus*, 3(1).
- 1401 Browning, D. F. and Busby, S. J. W. (2016). Local and global regulation of transcription initiation in bacteria. *Nature Reviews
1402 Microbiology*, 14(10):638–650.
- 1403 Büke, F., Grilli, J., Lagomarsino, M. C., Bokinsky, G., and Tans, S. (2020). ppGpp is a bacterial cell size regulator. *bioRxiv*,
1404 266:2020.06.16.154187.
- 1405 Catherwood, A. C., Lloyd, A. J., Tod, J. A., Chauhan, S., Slade, S. E., Walkowiak, G. P., Galley, N. F., Punekar, A. S., Smart, K., Rea, D.,
1406 Evans, N. D., Chappell, M. J., Roper, D. I., and Dowson, C. G. (2020). Substrate and Stereochemical Control of Peptidoglycan
1407 Cross-Linking by Transpeptidation by *Escherichia coli* PBP1B. *Journal of the American Chemical Society*, 142(11):5034–5048.
- 1408 Cox, G. B., Newton, N. A., Gibson, F., Snoswell, A. M., and Hamilton, J. A. (1970). The function of ubiquinone in *Escherichia coli*.
1409 *Biochemical Journal*, 117(3):551–562.
- 1410 Dai, X., Zhu, M., Warren, M., Balakrishnan, R., Okano, H., Williamson, J. R., Fredrick, K., and Hwa, T. (2018). Slowdown of Transla-
1411 tional Elongation in *Escherichia coli* under Hyperosmotic Stress. - PubMed - NCBI. *mBio*, 9(1):281.
- 1412 Dai, X., Zhu, M., Warren, M., Balakrishnan, R., Patsalo, V., Okano, H., Williamson, J. R., Fredrick, K., Wang, Y.-P., and Hwa, T.
1413 (2016). Reduction of translating ribosomes enables *Escherichia coli* to maintain elongation rates during slow growth. *Nature
1414 Microbiology*, 2(2):16231.
- 1415 Datsenko, K. A. and Wanner, B. L. (2000). One-step inactivation of chromosomal genes in *Escherichia coli* K-12 using PCR products.
1416 *Proceedings of the National Academy of Sciences*, 97(12):6640–6645.
- 1417 Dennis, P. P., Ehrenberg, M., and Bremer, H. (2004). Control of rRNA Synthesis in *Escherichia coli*: a Systems Biology Approach.
1418 *Microbiology and Molecular Biology Reviews*, 68(4):639–668.

- 1419 Dill, K. A., Ghosh, K., and Schmit, J. D. (2011). Physical limits of cells and proteomes. *Proceedings of the National Academy of Sciences*, 108(44):17876–17882.
- 1420
- 1421 Dong, H., Nilsson, L., and Kurland, C. G. (1996). Co-variation of tRNA Abundance and Codon Usage in *Escherichia coli* at Different Growth Rates. *Journal of Molecular Biology*, 260(5):649–663.
- 1422
- 1423 Erickson, D. W., Schink, S. J., Patsalo, V., Williamson, J. R., Gerland, U., and Hwa, T. (2017). A global resource allocation strategy governs growth transition kinetics of *Escherichia coli*. *Nature*, 551(7678):119–123.
- 1424
- 1425 Escalante, A., Salinas Cervantes, A., Gosset, G., and Bolívar, F. (2012). Current knowledge of the *Escherichia coli* phosphoenolpyruvate–carbohydrate phosphotransferase system: Peculiarities of regulation and impact on growth and product formation. *Applied Microbiology and Biotechnology*, 94(6):1483–1494.
- 1426
- 1427
- 1428 Feist, A. M., Henry, C. S., Reed, J. L., Krummenacker, M., Joyce, A. R., Karp, P. D., Broadbelt, L. J., Hatzimanikatis, V., and Palsson, B. Ø. (2007). A genome-scale metabolic reconstruction for *Escherichia coli* K-12 MG1655 that accounts for 1260 ORFs and thermodynamic information. *Molecular Systems Biology*, 3(1):121.
- 1429
- 1430
- 1431 Fernández-Coll, L., Maciąg-Dorszynska, M., Tailor, K., Vadia, S., Levin, P. A., Szalewska-Palasz, A., Cashel, M., and Dunny, G. M. (2020). The Absence of (p)ppGpp Renders Initiation of *Escherichia coli* Chromosomal DNA Synthesis Independent of Growth Rates. *mBio*, 11(2):45.
- 1432
- 1433
- 1434 Fijalkowska, I. J., Schaaper, R. M., and Jonczyk, P. (2012). DNA replication fidelity in *Escherichia coli*: A multi-DNA polymerase affair. *FEMS Microbiology Reviews*, 36(6):1105–1121.
- 1435
- 1436 Finkelstein, I. J. and Greene, E. C. (2013). Molecular Traffic Jams on DNA. *Annual Review of Biophysics*, 42(1):241–263.
- 1437
- 1438 Gallagher, L. A., Bailey, J., and Manoil, C. (2020). Ranking essential bacterial processes by speed of mutant death. *Proceedings of the National Academy of Sciences*.
- 1439
- 1440 Gama-Castro, S., Salgado, H., Santos-Zavaleta, A., Ledezma-Tejeida, D., Muñiz-Rascado, L., García-Sotelo, J. S., Alquicira-Hernández, K., Martínez-Flores, I., Pannier, L., Castro-Mondragón, J. A., Medina-Rivera, A., Solano-Lira, H., Bonavides-Martínez, C., Pérez-Rueda, E., Alquicira-Hernández, S., Porrón-Sotelo, L., López-Fuentes, A., Hernández-Koutoucheva, A., Moral-Chávez, V. D., Rinaldi, F., and Collado-Vides, J. (2016). RegulonDB version 9.0: High-level integration of gene regulation, coexpression, motif clustering and beyond. *Nucleic Acids Research*, 44(D1):D133–D143.
- 1441
- 1442
- 1443
- 1444 Ge, J., Yu, G., Ator, M. A., and Stubbe, J. (2003). Pre-Steady-State and Steady-State Kinetic Analysis of *E. coli* Class I Ribonucleotide Reductase. *Biochemistry*, 42(34):10071–10083.
- 1445
- 1446 Godin, M., Delgado, F. F., Son, S., Grover, W. H., Bryan, A. K., Tzur, A., Jorgensen, P., Payer, K., Grossman, A. D., Kirschner, M. W., and Manalis, S. R. (2010). Using buoyant mass to measure the growth of single cells. *Nature Methods*, 7(5):387–390.
- 1447
- 1448 Guo, Y., Li, D., Zhang, S., Yang, Y., Liu, J.-J., Wang, X., Liu, C., Milkie, D. E., Moore, R. P., Tulu, U. S., Kiehart, D. P., Hu, J., Lippincott-Schwartz, J., Betzig, E., and Li, D. (2018). Visualizing Intracellular Organelle and Cytoskeletal Interactions at Nanoscale Resolution on Millisecond Timescales. *Cell*, 175(5):1430–1442.e17.
- 1449
- 1450
- 1451 Harris, L. K. and Theriot, J. A. (2018). Surface Area to Volume Ratio: A Natural Variable for Bacterial Morphogenesis. *Trends in microbiology*, 26(10):815–832.
- 1452
- 1453 Harris, R. M., Webb, D. C., Howitt, S. M., and Cox, G. B. (2001). Characterization of PitA and PitB from *Escherichia coli*. *Journal of Bacteriology*, 183(17):5008–5014.
- 1454
- 1455 Haurihiuk, V., Atkinson, G. C., Murakami, K. S., Tenson, T., and Gerdes, K. (2015). Recent functional insights into the role of (p)ppGpp in bacterial physiology. *Nature Reviews Microbiology*, 13(5):298–309.
- 1456
- 1457 Heldal, M., Norland, S., and Tumyr, O. (1985). X-ray microanalytic method for measurement of dry matter and elemental content of individual bacteria. *Applied and Environmental Microbiology*, 50(5):1251–1257.
- 1458
- 1459 Helmstetter, C. E. and Cooper, S. (1968). DNA synthesis during the division cycle of rapidly growing *Escherichia coli* Br. *Journal of Molecular Biology*, 31(3):507–518.
- 1460
- 1461 Henkel, S. G., Beek, A. T., Steinsiek, S., Stagge, S., Bettenbrock, K., de Mattos, M. J. T., Sauter, T., Sawodny, O., and Ederer, M. (2014). Basic Regulatory Principles of *Escherichia coli*'s Electron Transport Chain for Varying Oxygen Conditions. *PLoS ONE*, 9(9):e107640.
- 1462
- 1463
- 1464 Ho, P.-Y. and Amir, A. (2015). Simultaneous regulation of cell size and chromosome replication in bacteria. *Frontiers in Microbiology*, 6.
- 1465

- ¹⁴⁶⁶ Hui, S., Silverman, J. M., Chen, S. S., Erickson, D. W., Basan, M., Wang, J., Hwa, T., and Williamson, J. R. (2015). Quantitative proteomic analysis reveals a simple strategy of global resource allocation in bacteria. *Molecular Systems Biology*, 11(2):e784-e784.
- ¹⁴⁶⁹ Ingledew, W. J. and Poole, R. K. (1984). The respiratory chains of *Escherichia coli*. *Microbiological Reviews*, 48(3):222–271.
- ¹⁴⁷⁰ Ireland, W. T., Beeler, S. M., Flores-Bautista, E., Belliveau, N. M., Sweredoski, M. J., Moradian, A., Kinney, J. B., and Phillips, R. (2020). Deciphering the regulatory genome of *Escherichia coli*, one hundred promoters at a time. *bioRxiv*.
- ¹⁴⁷² Jensen, R. B., Wang, S. C., and Shapiro, L. (2001). A moving DNA replication factory in *Caulobacter crescentus*. *The EMBO journal*, 20(17):4952–4963.
- ¹⁴⁷⁴ Jun, S., Si, F., Pugatch, R., and Scott, M. (2018). Fundamental principles in bacterial physiology - history, recent progress, and the future with focus on cell size control: A review. *Reports on Progress in Physics*, 81(5):056601.
- ¹⁴⁷⁶ Karp, P. D., Billington, R., Caspi, R., Fulcher, C. A., Latendresse, M., Kothari, A., Keseler, I. M., Krummenacker, M., Midford, P. E., Ong, Q., Ong, W. K., Paley, S. M., and Subhraveti, P. (2019). The BioCyc collection of microbial genomes and metabolic pathways. *Briefings in Bioinformatics*, 20(4):1085–1093.
- ¹⁴⁷⁹ Karr, J. R., Sanghvi, J. C., Macklin, D. N., Gutschow, M. V., Jacobs, J. M., Bolival, B., Assad-Garcia, N., Glass, J. I., and Covert, M. W. (2012). A Whole-Cell Computational Model Predicts Phenotype from Genotype. *Cell*, 150(2):389–401.
- ¹⁴⁸¹ Keseler, I. M., Mackie, A., Santos-Zavaleta, A., Billington, R., Bonavides-Martínez, C., Caspi, R., Fulcher, C., Gama-Castro, S., Kothari, A., Krummenacker, M., Latendresse, M., Muñiz-Rascado, L., Ong, Q., Paley, S., Peralta-Gil, M., Subhraveti, P., Velázquez-Ramírez, D. A., Weaver, D., Collado-Vides, J., Paulsen, I., and Karp, P. D. (2017). The EcoCyc database: reflecting new knowledge about *Escherichia coli*K-12. *Nucleic Acids Research*, 45(D1):D543–D550.
- ¹⁴⁸⁵ Khademi, S., O'Connell, J., Remis, J., Robles-Colmenares, Y., Miercke, L. J. W., and Stroud, R. M. (2004). Mechanism of Ammonia Transport by Amt/MEP/Rh: Structure of AmtB at 1.35 Å. *Science*, 305(5690):1587–1594.
- ¹⁴⁸⁷ Khademian, M. and Imlay, J. A. (2017). *Escherichia coli* cytochrome c peroxidase is a respiratory oxidase that enables the use of hydrogen peroxide as a terminal electron acceptor. *Proceedings of the National Academy of Sciences*, 114(33):E6922–E6931.
- ¹⁴⁸⁹ Klumpp, S. and Hwa, T. (2008). Growth-rate-dependent partitioning of RNA polymerases in bacteria. *Proceedings of the National Academy of Sciences*, 105(51):20245–20250.
- ¹⁴⁹¹ Klumpp, S. and Hwa, T. (2014). Bacterial growth: Global effects on gene expression, growth feedback and proteome partition. *Current Opinion in Biotechnology*, 28:96–102.
- ¹⁴⁹³ Klumpp, S., Scott, M., Pedersen, S., and Hwa, T. (2013). Molecular crowding limits translation and cell growth. *Proceedings of the National Academy of Sciences*, 110(42):16754–16759.
- ¹⁴⁹⁵ Kostinski, S. and Reuveni, S. (2020). Ribosome Composition Maximizes Cellular Growth Rates in *E. coli*. *Physical Review Letters*, 125(2):028103.
- ¹⁴⁹⁷ Kraemer, J. A., Sanderlin, A. G., and Laub, M. T. (2019). The Stringent Response Inhibits DNA Replication Initiation in *E. coli* by Modulating Supercoiling of oriC. *mBio*, 10(4):822.
- ¹⁴⁹⁹ Lascu, I. and Gonin, P. (2000). The Catalytic Mechanism of Nucleoside Diphosphate Kinases. *Journal of Bioenergetics and Biomembranes*, 32(3):237–246.
- ¹⁵⁰¹ Laxhuber, K. S., Morrison, M. J., Chure, G., Belliveau, N. M., Strandkvist, C., Naughton, K. L., and Phillips, R. (2020). Theoretical investigation of a genetic switch for metabolic adaptation. *PLOS ONE*, 15(5):e0226453.
- ¹⁵⁰³ Li, G.-W., Burkhardt, D., Gross, C., and Weissman, J. S. (2014). Quantifying absolute protein synthesis rates reveals principles underlying allocation of cellular resources. *Cell*, 157(3):624–635.
- ¹⁵⁰⁵ Liebermeister, W., Noor, E., Flamholz, A., Davidi, D., Bernhardt, J., and Milo, R. (2014). Visual account of protein investment in cellular functions. *Proceedings of the National Academy of Sciences*, 111(23):8488–8493.
- ¹⁵⁰⁷ Liu, M., Durfee, T., Cabrera, J. E., Zhao, K., Jin, D. J., and Blattner, F. R. (2005). Global Transcriptional Programs Reveal a Carbon Source Foraging Strategy by *Escherichia coli*. *Journal of Biological Chemistry*, 280(16):15921–15927.
- ¹⁵⁰⁹ Lu, D., Grayson, P., and Schulten, K. (2003). Glycerol Conductance and Physical Asymmetry of the *Escherichia coli* Glycerol Facilitator GlpF. *Biophysical Journal*, 85(5):2977–2987.
- ¹⁵¹¹ Lynch, M. and Marinov, G. K. (2015). The bioenergetic costs of a gene. *Proceedings of the National Academy of Sciences*, 112(51):15690–15695.

- 1513 Maaløe, O. (1979). *Regulation of the Protein-Synthesizing Machinery—Ribosomes, tRNA, Factors, and So On*. Gene Expression.
1514 Springer.
- 1515 Macklin, D. N., Ahn-Horst, T. A., Choi, H., Ruggero, N. A., Carrera, J., Mason, J. C., Sun, G., Agmon, E., DeFelice, M. M., Maayan,
1516 I., Lane, K., Spangler, R. K., Gillies, T. E., Paull, M. L., Akhter, S., Bray, S. R., Weaver, D. S., Keseler, I. M., Karp, P. D., Morrison,
1517 J. H., and Covert, M. W. (2020). Simultaneous cross-evaluation of heterogeneous *E. coli* datasets via mechanistic simulation.
1518 *Science*, 369(6502).
- 1519 Mahajan, S. (2010). *Street-Fighting Mathematics*. The Art of Educated Guessing and Opportunistic Problem Solving. MIT Press.
- 1520 Metzl-Raz, E., Kafri, M., Yaakov, G., Soifer, I., Gurvich, Y., and Barkai, N. (2017). Principles of cellular resource allocation revealed
1521 by condition-dependent proteome profiling. *eLife*, 6:e03528.
- 1522 Mikucki, J. A., Pearson, A., Johnston, D. T., Turchyn, A. V., Farquhar, J., Schrag, D. P., Anbar, A. D., Priscu, J. C., and Lee, P. A. (2009).
1523 A Contemporary Microbially Maintained Subglacial Ferrous "Ocean". *Science*, 324(5925):397–400.
- 1524 Milo, R., Jorgensen, P., Moran, U., Weber, G., and Springer, M. (2010). BioNumbers—the database of key numbers in molecular
1525 and cell biology. *Nucleic Acids Research*, 38(suppl_1):D750–D753.
- 1526 Molenaar, D., van Berlo, R., de Ridder, D., and Teusink, B. (2009). Shifts in growth strategies reflect tradeoffs in cellular economics.
1527 *Molecular Systems Biology*, 5(1):323.
- 1528 Monod, J. (1947). The phenomenon of enzymatic adaptation and its bearings on problems of genetics and cellular differentiation.
1529 *Growth Symposium*, 9:223–289.
- 1530 Monod, J. (1949). The Growth of Bacterial Cultures. *Annual Review of Microbiology*, 3(1):371–394.
- 1531 Morgenstein, R. M., Bratton, B. P., Nguyen, J. P., Ouzounov, N., Shaevitz, J. W., and Gitai, Z. (2015). RodZ links MreB to cell wall
1532 synthesis to mediate MreB rotation and robust morphogenesis. *Proceedings of the National Academy of Sciences*, 112(40):12510–
1533 12515.
- 1534 Neidhardt, F. C., Ingraham, J., and Schaechter, M. (1991). *Physiology of the Bacterial Cell - A Molecular Approach*, volume 1. Elsevier.
- 1535 Ojikic, N., Serbanescu, D., and Banerjee, S. (2019). Surface-to-volume scaling and aspect ratio preservation in rod-shaped bacteria.
1536 *eLife*, 8:642.
- 1537 Patrick, M., Dennis, P. P., Ehrenberg, M., and Bremer, H. (2015). Free RNA polymerase in *Escherichia coli*. *Biochimie*, 119:80–91.
- 1538 Pedersen, S. (1978). Patterns of protein synthesis in *E. coli*: a catalog of the amount of 140 individual proteins at different growth
1539 rates. *Cell*, 14(1):179–190.
- 1540 Peebo, K., Valgepea, K., Maser, A., Nahku, R., Adamberg, K., and Vilu, R. (2015). Proteome reallocation in *Escherichia coli* with
1541 increasing specific growth rate. *Molecular BioSystems*, 11(4):1184–1193.
- 1542 Phillips, R. (2018). Membranes by the Numbers. In *Physics of Biological Membranes*, pages 73–105. Springer, Cham.
- 1543 Ramos, S. and Kaback, H. R. (1977). The relation between the electrochemical proton gradient and active transport in *Escherichia*
1544 *coli* membrane vesicles. *Biochemistry*, 16(5):854–859.
- 1545 Ranganathan, S., Tee, T. W., Chowdhury, A., Zomorodi, A. R., Yoon, J. M., Fu, Y., Shanks, J. V., and Maranas, C. D. (2012). An
1546 integrated computational and experimental study for overproducing fatty acids in *Escherichia coli*. *Metabolic Engineering*,
1547 14(6):687–704.
- 1548 Rogers, H., Perkins, H., and Ward, J. (1980). *Microbial Cell Walls and Membranes*. Chapman and Hall, London.
- 1549 Roller, B. R. K., Stoddard, S. F., and Schmidt, T. M. (2016). Exploiting rRNA operon copy number to investigate bacterial reproduc-
1550 tive strategies. *Nature microbiology*, 1(11):1–7.
- 1551 Rosenberg, H., Gerdes, R. G., and Chegwidden, K. (1977). Two systems for the uptake of phosphate in *Escherichia coli*. *Journal of*
1552 *Bacteriology*, 131(2):505–511.
- 1553 Rudd, S. G., Valerie, N. C. K., and Helleday, T. (2016). Pathways controlling dNTP pools to maintain genome stability. *DNA Repair*,
1554 44:193–204.
- 1555 Ruppe, A. and Fox, J. M. (2018). Analysis of Interdependent Kinetic Controls of Fatty Acid Synthases. *ACS Catalysis*, 8(12):11722–
1556 11734.

- ¹⁵⁵⁷ Sánchez-Romero, M. A., Molina, F., and Jiménez-Sánchez, A. (2011). Organization of ribonucleoside diphosphate reductase during multifork chromosome replication in *Escherichia coli*. *Microbiology*, 157(8):2220–2225.
- ¹⁵⁵⁹ Schaechter, M., MaalØe, O., and Kjeldgaard, N. O. (1958). Dependency on Medium and Temperature of Cell Size and Chemical Composition during Balanced Growth of *Salmonella typhimurium*. *Microbiology*, 19(3):592–606.
- ¹⁵⁶¹ Schmidt, A., Kochanowski, K., Vedelaar, S., Ahrné, E., Volkmer, B., Callipo, L., Knoops, K., Bauer, M., Aebersold, R., and Heinemann, M. (2016). The quantitative and condition-dependent *Escherichia coli* proteome. *Nature Biotechnology*, 34(1):104–110.
- ¹⁵⁶³ Scott, M., Gunderson, C. W., Mateescu, E. M., Zhang, Z., and Hwa, T. (2010). Interdependence of cell growth and gene expression: origins and consequences. *Science*, 330(6007):1099–1102.
- ¹⁵⁶⁵ Sekowska, A., Kung, H.-F., and Danchin, A. (2000). Sulfur Metabolism in *Escherichia coli* and Related Bacteria: Facts and Fiction. *Journal of Molecular Microbiology and Biotechnology*, 2(2):34.
- ¹⁵⁶⁷ Shi, H., Bratton, B. P., Gitai, Z., and Huang, K. C. (2018). How to Build a Bacterial Cell: MreB as the Foreman of *E. coli* Construction. *Cell*, 172(6):1294–1305.
- ¹⁵⁶⁹ Si, F., Le Treut, G., Sauls, J. T., Vadia, S., Levin, P. A., and Jun, S. (2019). Mechanistic Origin of Cell-Size Control and Homeostasis in Bacteria. *Current Biology*, 29(11):1760–1770.e7.
- ¹⁵⁷¹ Si, F., Li, D., Cox, S. E., Sauls, J. T., Azizi, O., Sou, C., Schwartz, A. B., Erickstad, M. J., Jun, Y., Li, X., and Jun, S. (2017). Invariance of Initiation Mass and Predictability of Cell Size in *Escherichia coli*. *Current Biology*, 27(9):1278–1287.
- ¹⁵⁷³ Sirko, A., Zatyka, M., Sadowy, E., and Hulanicka, D. (1995). Sulfate and thiosulfate transport in *Escherichia coli* K-12: Evidence for a functional overlapping of sulfate- and thiosulfate-binding proteins. *Journal of Bacteriology*, 177(14):4134–4136.
- ¹⁵⁷⁵ Sohlenkamp, C. and Geiger, O. (2016). Bacterial membrane lipids: Diversity in structures and pathways. *FEMS Microbiology Reviews*, 40(1):133–159.
- ¹⁵⁷⁷ Soufi, B., Krug, K., Harst, A., and Macek, B. (2015). Characterization of the *E. coli* proteome and its modifications during growth and ethanol stress. *Frontiers in Microbiology*, 6:198.
- ¹⁵⁷⁹ Stasi, R., Neves, H. I., and Spira, B. (2019). Phosphate uptake by the phosphonate transport system PhnCDE. *BMC Microbiology*, 19.
- ¹⁵⁸¹ Stouthamer, A. H. (1973). A theoretical study on the amount of ATP required for synthesis of microbial cell material. *Antonie van Leeuwenhoek*, 39(1):545–565.
- ¹⁵⁸³ Stouthamer, A. H. and Bettenhausen, C. W. (1977). A continuous culture study of an ATPase-negative mutant of *Escherichia coli*. *Archives of Microbiology*, 113(3):185–189.
- ¹⁵⁸⁵ Svenningsen, S. L., Kongstad, M., Stenum, T. S. n., Muñoz-Gómez, A. J., and Sørensen, M. A. (2017). Transfer RNA is highly unstable during early amino acid starvation in *Escherichia coli*. *Nucleic Acids Research*, 45(2):793–804.
- ¹⁵⁸⁷ Szenk, M., Dill, K. A., and de Graff, A. M. R. (2017). Why Do Fast-Growing Bacteria Enter Overflow Metabolism? Testing the Membrane Real Estate Hypothesis. *Cell Systems*, 5(2):95–104.
- ¹⁵⁸⁹ Taheri-Araghi, S., Bradde, S., Sauls, J. T., Hill, N. S., Levin, P. A., Paulsson, J., Vergassola, M., and Jun, S. (2015). Cell-size control and homeostasis in bacteria. - PubMed - NCBI. *Current Biology*, 25(3):385–391.
- ¹⁵⁹¹ Taniguchi, Y., Choi, P. J., Li, G.-W., Chen, H., Babu, M., Hearn, J., Emili, A., and Xie, X. S. (2010). Quantifying *E. coli* proteome and transcriptome with single-molecule sensitivity in single cells. *Science (New York, N.Y.)*, 329(5991):533–538.
- ¹⁵⁹³ Tatusov, R. L., Galperin, M. Y., Natale, D. A., and Koonin, E. V. (2000). The COG database: a tool for genome-scale analysis of protein functions and evolution. *Nucleic Acids Research*, 28(1):33–36.
- ¹⁵⁹⁵ Taymaz-Nikerel, H., Borujeni, A. E., Verheijen, P. J. T., Heijnen, J. J., and van Gulik, W. M. (2010). Genome-derived minimal metabolic models for *Escherichia coli* MG1655 with estimated in vivo respiratory ATP stoichiometry. *Biotechnology and Bioengineering*, 107(2):369–381. _eprint: <https://onlinelibrary.wiley.com/doi/pdf/10.1002/bit.22802>.
- ¹⁵⁹⁸ The Gene Ontology Consortium (2018). The Gene Ontology Resource: 20 years and still GOing strong. *Nucleic Acids Research*, 47(D1):D330–D338.
- ¹⁶⁰⁰ Valgepea, K., Adamberg, K., Seiman, A., and Vilu, R. (2013). *Escherichia coli* achieves faster growth by increasing catalytic and translation rates of proteins. *Molecular BioSystems*, 9(9):2344.

- ¹⁶⁰² van Heeswijk, W. C., Westerhoff, H. V., and Boogerd, F. C. (2013). Nitrogen Assimilation in *Escherichia coli*: Putting Molecular
¹⁶⁰³ Data into a Systems Perspective. *Microbiology and Molecular Biology Reviews*, 77(4):628–695.
- ¹⁶⁰⁴ Virtanen, P., Gommers, R., Oliphant, T. E., Haberland, M., Reddy, T., Cournapeau, D., Burovski, E., Peterson, P., Weckesser, W.,
¹⁶⁰⁵ Bright, J., van der Walt, S. J., Brett, M., Wilson, J., Jarrod Millman, K., Mayorov, N., Nelson, A. R. J., Jones, E., Kern, R., Larson,
¹⁶⁰⁶ E., Carey, C., Polat, İ., Feng, Y., Moore, E. W., VanderPlas, J., Laxalde, D., Perktold, J., Cimrman, R., Henriksen, I., Quintero,
¹⁶⁰⁷ E. A., Harris, C. R., Archibald, A. M., Ribeiro, A. H., Pedregosa, F., van Mulbregt, P., and Contributors, S. . . (2020). SciPy 1.0:
¹⁶⁰⁸ Fundamental Algorithms for Scientific Computing in Python. *Nature Methods*, 17:261–272.
- ¹⁶⁰⁹ Volkmer, B. and Heinemann, M. (2011). Condition-Dependent Cell Volume and Concentration of *Escherichia coli* to Facilitate Data
¹⁶¹⁰ Conversion for Systems Biology Modeling. *PLOS ONE*, 6(7):e23126.
- ¹⁶¹¹ Vollmer, W., Blanot, D., and De Pedro, M. A. (2008). Peptidoglycan structure and architecture. *FEMS Microbiology Reviews*,
¹⁶¹² 32(2):149–167.
- ¹⁶¹³ Weber, J. and Senior, A. E. (2003). ATP synthesis driven by proton transport in F1F0-ATP synthase. *FEBS Letters*, 545(1):61–70.
- ¹⁶¹⁴ Willsky, G. R., Bennett, R. L., and Malamy, M. H. (1973). Inorganic Phosphate Transport in *Escherichia coli*: Involvement of Two
¹⁶¹⁵ Genes Which Play a Role in Alkaline Phosphatase Regulation. *Journal of Bacteriology*, 113(2):529–539.
- ¹⁶¹⁶ You, C., Okano, H., Hui, S., Zhang, Z., Kim, M., Gunderson, C. W., Wang, Y.-P., Lenz, P., Yan, D., and Hwa, T. (2013). Coordination
¹⁶¹⁷ of bacterial proteome with metabolism by cyclic AMP signalling. *Nature*, 500(7462):301–306.
- ¹⁶¹⁸ Yu, X., Liu, T., Zhu, F., and Khosla, C. (2011). In vitro reconstitution and steady-state analysis of the fatty acid synthase from
¹⁶¹⁹ *Escherichia coli*. *Proceedings of the National Academy of Sciences*, 108(46):18643–18648.
- ¹⁶²⁰ Zhang, L., Jiang, W., Nan, J., Almqvist, J., and Huang, Y. (2014a). The *Escherichia coli* CysZ is a pH dependent sulfate transporter
¹⁶²¹ that can be inhibited by sulfite. *Biochimica et Biophysica Acta (BBA) - Biomembranes*, 1838(7):1809–1816.
- ¹⁶²² Zhang, Z., Aboulwafa, M., and Saier, M. H. (2014b). Regulation of crp gene expression by the catabolite repressor/activator, cra,
¹⁶²³ in *Escherichia coli*. *Journal of Molecular Microbiology and Biotechnology*, 24(3):135–141.
- ¹⁶²⁴ Zhu, M. and Dai, X. (2019). Growth suppression by altered (p)ppGpp levels results from non-optimal resource allocation in
¹⁶²⁵ *Escherichia coli*. *Nucleic Acids Research*, 47(9):4684–4693.
- ¹⁶²⁶ Zhuang, K., Vemuri, G. N., and Mahadevan, R. (2011). Economics of membrane occupancy and respiro-fermentation. *Molecular
¹⁶²⁷ Systems Biology*, 7(1):500.

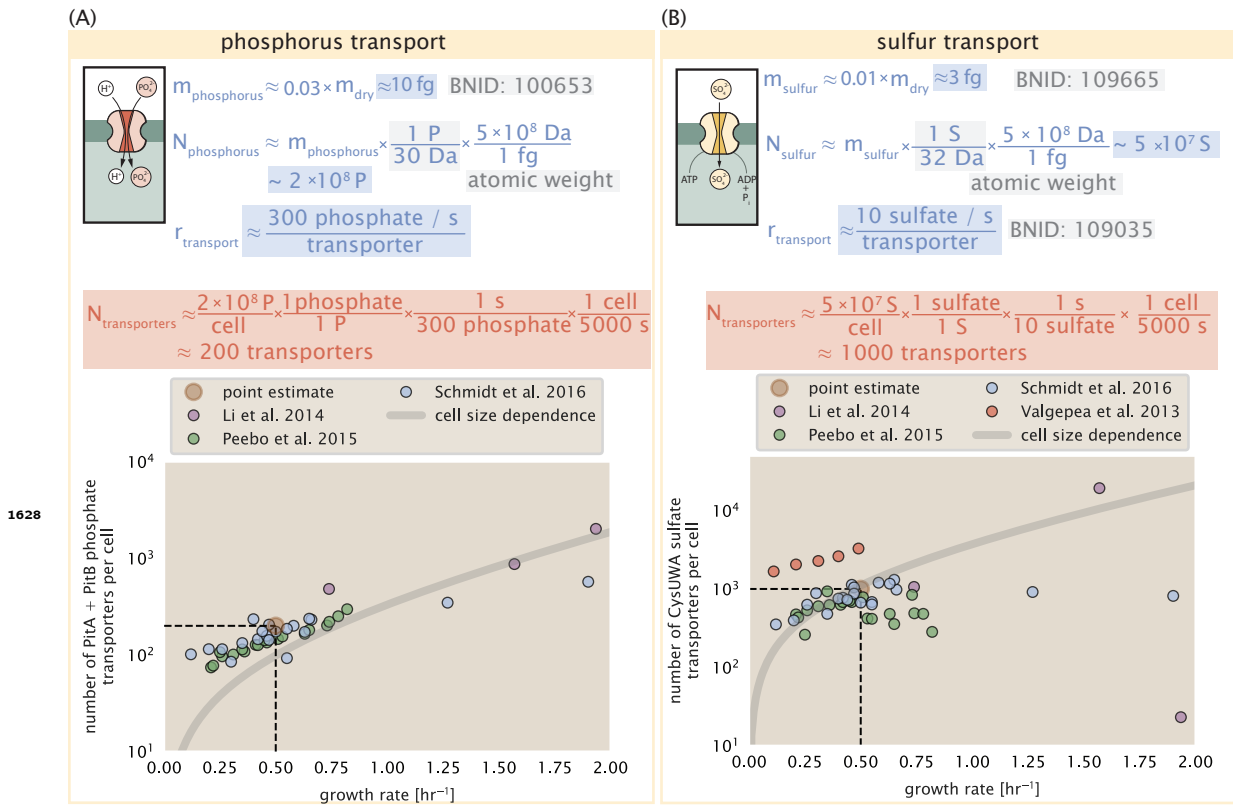


Figure 2-Figure supplement 1. (A) Estimate for the number of PitA phosphate transport systems needed to maintain a 3% phosphorus *E. coli* dry mass. Points in plot correspond to the total number of PitA transporters per cell. (B) Estimate of the number of CysUWA complexes necessary to maintain a 1% sulfur *E. coli* dry mass. Points in plot correspond to average number of CysUWA transporter complexes that can be formed given the transporter stoichiometry $[CysA]_2[CysU][CysW][Sbp/CysP]$. Grey line in (A) and (B) represents the estimated number of transporters per cell at a continuum of growth rates.

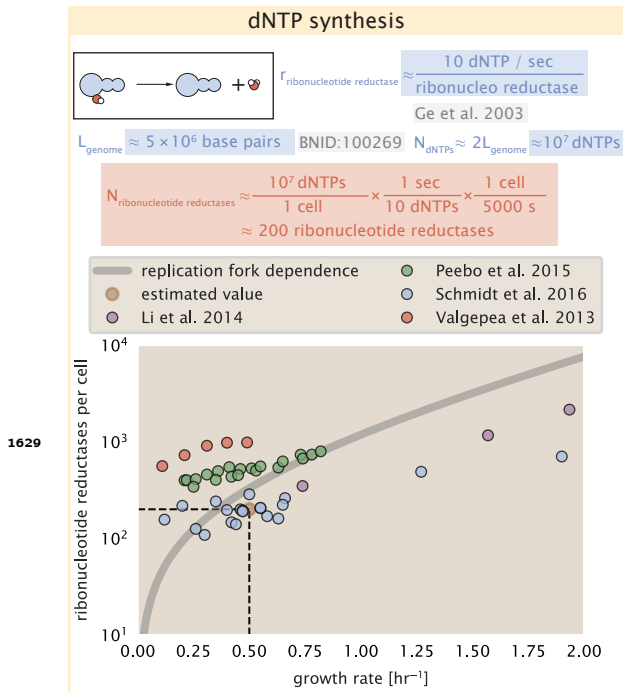


Figure 6–Figure supplement 1. Estimate of the number of ribonucleotide reductase enzymes needed to facilitate the synthesis of $\approx 10^7$ dNTPs over the course of a 5000 second generation time. Points in the plot correspond to the total number of ribonucleotide reductase I ($[\text{NrdA}]_2[\text{NrdB}]_2$) and ribonucleotide reductase II ($[\text{NrdE}]_2[\text{NrdF}]_2$) complexes. Grey lines in top panel show the estimated number of complexes needed as a function of growth, the details of which are described in the Appendix.

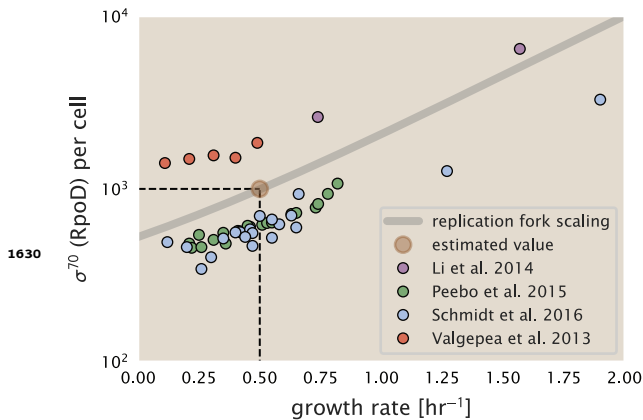


Figure 7–Figure supplement 1. The abundance of σ^{70} as a function of growth rate. Estimated value for the number of RNAP is shown as a translucent brown point and grey line.

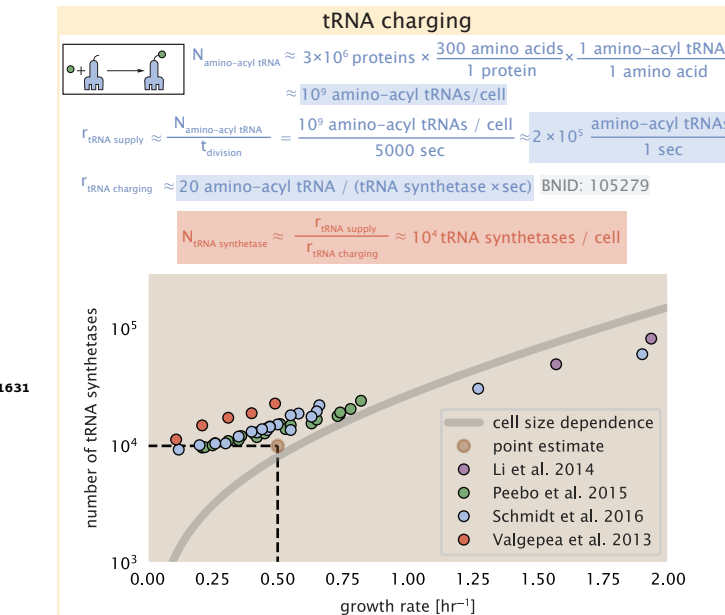


Figure 8-Figure supplement 1. Estimation for the number of tRNA synthetases that will supply the required amino acid demand. The sum of all tRNA synthetases copy numbers are plotted as a function of growth rate ([ArgS], [CysS], [GlnS], [GltX], [IleS], [LeuS], [ValS], [AlaS]₂, [AsnS]₂, [AspS]₂, [TyrS]₂, [TrpS]₂, [ThrS]₂, [SerS]₂, [ProS]₂, [PheS]₂[PheT]₂, [MetG]₂, [lysS]₂, [HisS]₂, [GlyS]₂[GlyQ]₂).

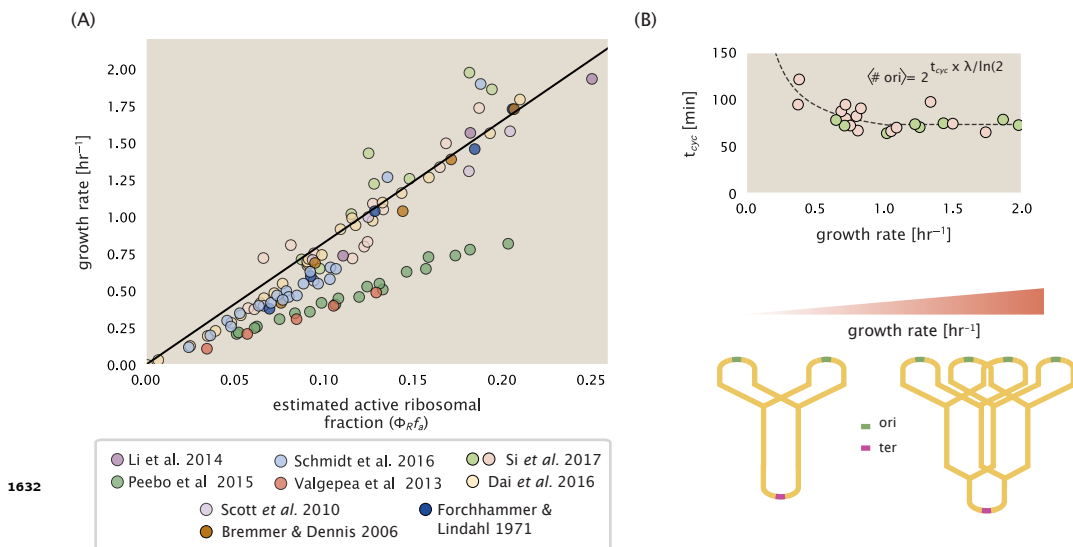


Figure 9-Figure supplement 1. (A) Actively translating ribosomal fraction versus growth rate. The actively translating ribosomal fraction is calculated using the estimated values of f_a from ? (shown in inset; see the Appendix Section "Calculation of active ribosomal fraction" for additional detail). Additional measurements in addition to the proteomic measurements are based on measurements of cellular RNA to protein ratio, with $\Phi_R \approx$ the cellular RNA to protein ratio divided by 2.1 (?). (B) Experimental measurements of the cell doubling time τ and cell cycle time t_{cyc} from Si et al. (2017). Dashed line shows fit to the data, which were used to estimate $\langle \# \text{ori} \rangle$. t_{cyc} was assumed to vary in proportion to τ for doubling times greater than 40 minutes, and reach a minimum value of 73 minutes. See Appendix Estimation of $\langle \# \text{ori} \rangle / \langle \# \text{ter} \rangle$ and $\langle \# \text{ori} \rangle$ for additional details exact estimation of rRNA copy number. Red data points correspond to measurements in strain MG1655, while light green points are for strain NCM3722. Schematic shows the expected increase in replication forks (or number of ori regions) as *E. coli* cells grow faster.

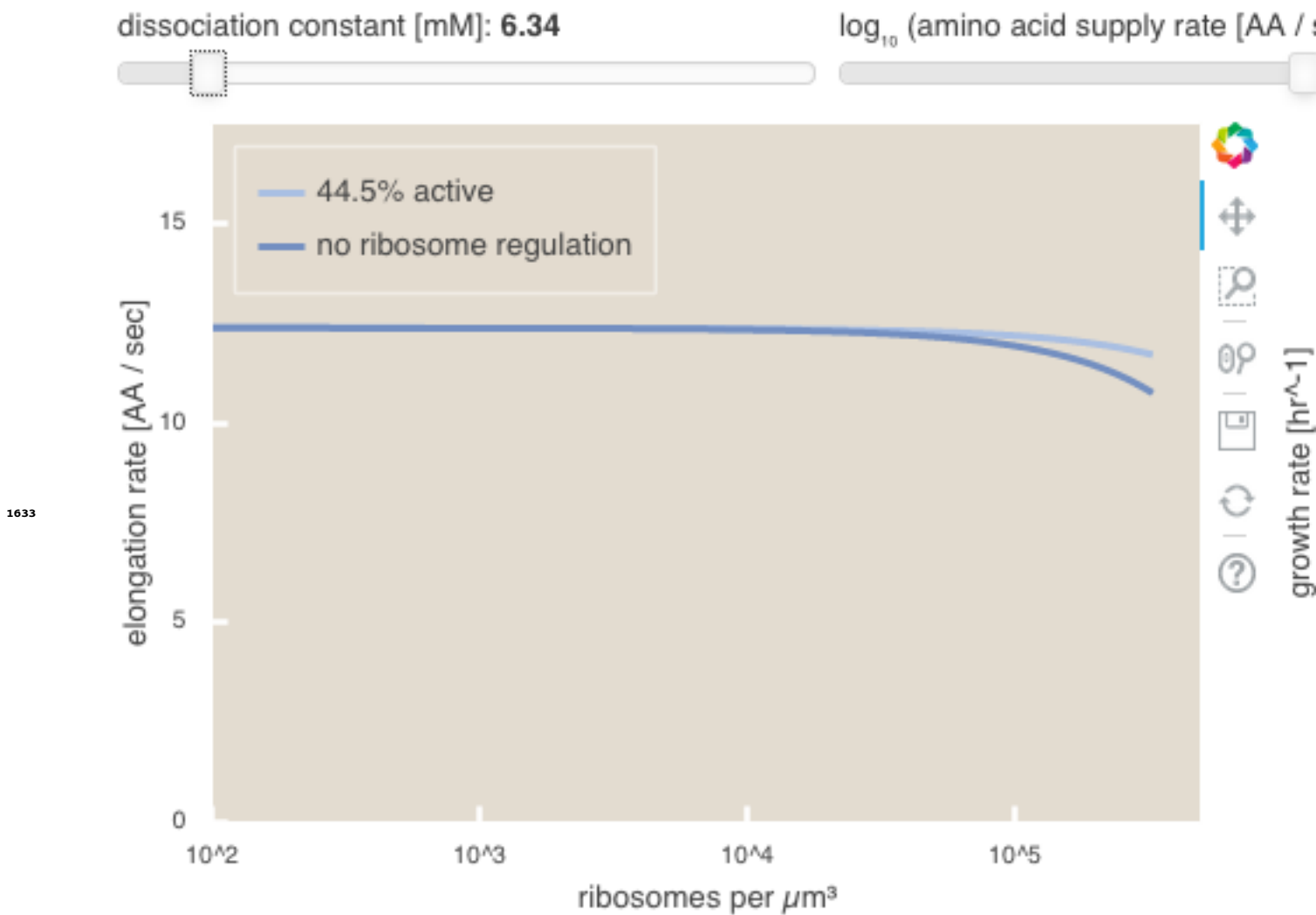


Figure 11–Figure supplement 1. An interactive version of parts (B) and (C) of **Figure 11** which permit the user to modulate the rate of amino acid supply, the dissociation constant of amino acids to the ribosome, and the fraction of the ribosome pool that is actively translating. This interactive figure, and the code used to generate it, is available on the [paper website](#).